Defects and transport in Ce-doped $La_{27}W_5O_{55.5}$

Nadezda Alyeshkina

Master Thesis in Materials, Energy and Nanotechnology

UNIVERSITY OF OSLO

DEPARTMENT OF CHEMISTRY

June 2013

Preface

This thesis represents the experimental part of the Master studies at Materials, Energy and Nanotechnology at the Department of chemistry, University of Oslo. The work was performed at the Centre for Material Science and Nanotechnology (SMN) at the research group Solid-State Electrochemistry in the period August 2011 to June 2013.

Firstly I would like to thank the entire research group for creating an inspiring and comfortable environment and making me feeling part of the team.

I would especially like to thank Truls Norby for giving me the opportunity to be a part of the research group and for giving me an interesting and challenging problem to work with my study.

I would like to thank my brilliant supervisor Associate Professor Reidar Haugsrud for great guidance, support, critical comments and technical assistance throughout the work. I would also like to thank my co-supervisor PhD student Wen Xing for his great enthusiasm, advice and inspiration.

Furthermore, I thank Reidar Haugsrud, Anna Magrasó, Camilla Vigen, Wen Xing for feedback during writing process and all help in the lab.

In addition I want to thank all my fellow students and especially Xuemei Cue for great collaboration during this project.

University of Oslo, June 2013

Nadezda Alyeshkina

Abstract

Non-perovskite structured oxides are the promising candidates for fuel cell and/or gas separation membrane applications. Some of them exhibit mixed proton-electron conductivity and are stable towards CO_2 and SO_2/SO_3 containing atmosphere. Rare – earth tungstates such as $La_{28-x}W_{4+x}O_{54+1,5x}v_{2-1,5x}$ attracted attention recently for their significant protonic conductivity at elevated temperatures. It was therefore of interest to study the conductivity of these materials upon substitution of La^{3+} with Ce^{4+} in LWO.

Lanthanum tungstate with a nominal composition $La_{27}W_5O_{55.5}v_{0.5}$ was doped with 2 mol% and 5 mol% CeO_2. These compounds were synthesized by a wet-chemical method, calcined at 1000 °C for 11 hours and sintered at 1500 °C for 5-7 hours. The crystal structure was characterized by XRD. The microstructure and the ratio of the cations were studied by SEM and EPMA, respectively.

The defect structure and the transport properties of 2%Ce – and 5%Ce- doped $La_{27}W_5O_{55.5}$ have been studied by means of thermogravimetric measurements and electrical measurements as a function of temperature, oxygen vapor pressure and water vapor pressure in the temperature range 1000 – 300 °C. In order to study the water uptake of the material after the donor doping and measure the standard molar hydration thermodynamic properties, thermogravimetric measurements were performed on 2Ce-LWO.

From the total conductivity measurements it was observed that the compounds exhibit mixed ionic-electronic conductivity. The total conductivity of both samples is predominated by protons under wet atmospheres below ~ 800 °C and the protonic conductivity reached a maximum of $\sim 1 \times 10^{-3}$ S/cm and $\sim 3 \times 10^{-4}$ S/cm above 800 °C for 2Ce-LWO and 5Ce-LWO, respectively. At high temperatures both samples exhibit n-and p-type electronic conduction under reducing and oxidizing conditions respectively. Donor doping decreases the ionic contribution of $La_{27}W_5O_{55.5}$, whereas it enhances the n-type electronic conductivity for both samples, and it is more significant with the higher level of donor dopant.

Impedance spectroscopy was conducted at temperature range of 300 - 1000 °C. The measurements demonstrated relatively resistive grain boundaries under oxidizing

conditions, which increases with increasing level of the dopant. Under reducing conditions no grain boundary contribution was detected. This difference was suggested to be due to a positive space charge layer, which was depleted under reducing conditions.

EPMA analysis revealed formation of $La_6W_2O_{15}$ as a secondary phase. Understanding of this behavior was supported by existence of La1 and La2 sites with different coordination number, where some La2 sites are donor substituted by W, forming intrinsic positive defect, the concentration of which is determined by the crystal structure of $La_{28-x}W_{4+x}O_{54+1,5x}v_{2-1,5x.}$ (see subsection 3.1.1). The formation of the secondary phase may be formed due to donor substitution of both La and W_{La2} sites in $La_{27}W_5O_{55.5}v_{0.5}$. This phase was not refined by Rietveld method, but the peaks were close to those reported earlier.

The derived defect structure was used as a basis to model the conductivity and the thermogravimetry data to extract thermodynamic and transport parameters. This approach gave a hydration enthalpy and entropy in the range of -105 ± 5 kJ/mol and -123 ± 5 J/molK, respectively, varying slightly between two experimental approaches. The thermogravimetric parameters extracted from the thermogravimetric analysis were in agreement with the values extracted from the conductivity measurements. The enthalpy of mobility of protons and oxide ions for both compounds was in good agreement with reported data, of 60 ± 5 kJ/mol and $\sim 90\pm10$ kJ/mol respectively.

List of Abbreviations

LWO	$La_{28-x}W_{4+x}O_{54+1,5x}v_{2-1,5x}$
LWO52	$La_{26.84}W_{5.16}O_{55.74}v_{0.26}$
LWO53	$La_{25.92}W_{5.08}O_{55.62}v_{0.38}$
LWO54	$La_{27}W_{5}O_{55.5}v_{0.5}$
LWO57	$La_{27.22}W_{4.77}O_{55.16}v_{0.84}$
LWO58	$La_{27.3}W4.7O_{55.05}v_{0.95}$
LWO6	$La_{27.43}W_{4.57}O_{54.85}v_{1.15}$
NdWO6	$Nd_{27.43}W_{4.57}O_{54.85}v_{1.15}$
ErWO6	$Er_{27.43}W_{4.57}O_{54.85}v_{1.15}$
2Ce-LWO	2%Ce-doped LWO54 on La site
5Ce-LWO	5%Ce-doped LWO54 on La site

AC	Alternating current
BSE	Backscattered electrons
CPE	Constant phase element
CS	Cross section
EDS	Energy dispersive spectroscopy
EPMA	Electron probe micro-analysis
ppm	Parts per million
SEM	Scanning electron microscopy
SOFC	Solid oxide fuel cell
TEM	Transmission electron microscopy
TG	Thermogravimetry
XRD	Powder X-Ray diffraction

Quantity name	**SI unit**
Admittance Y	S – Siemens
Capacitance C	F - Farad
Conductance G	S – Siemens
Impedance Z	Ω - Ohm
Inductance L	H - Henry
Resistance R	Ω - Ohm
Susceptance B	S - Siemens

Table of contents

1 Introduction

1.1 Background and Motivation

Today, energy is the basis for the industrial development and quality of life of mankind. The total energy consumption increases with 3% every year due to increasing world population [1]. The history of energy sources passed the firewood, energy of water, wind, wood and coals. The industrial revolution changed the major energy sources to coal, oil, gas nuclear energy and others. The world has become dependent on energy availability at low cost, which was, and still is, a prime factor for high quality of life in the development countries [1].

Figure 1.1 illustrates the huge increase in the world's energy consumption that has taken place in the last 200 years and in particular since the 1950s. E.g. the energy consumption has increased by 39% to a value 5.2×10^{20} J from 1990 to 2007 [2]. The rise in energy consumption is primarily from increased fossil fuel using [3]. However, the fossil fuels are non-renewable, and with the current rate of consumption, it will run out in 150 years.

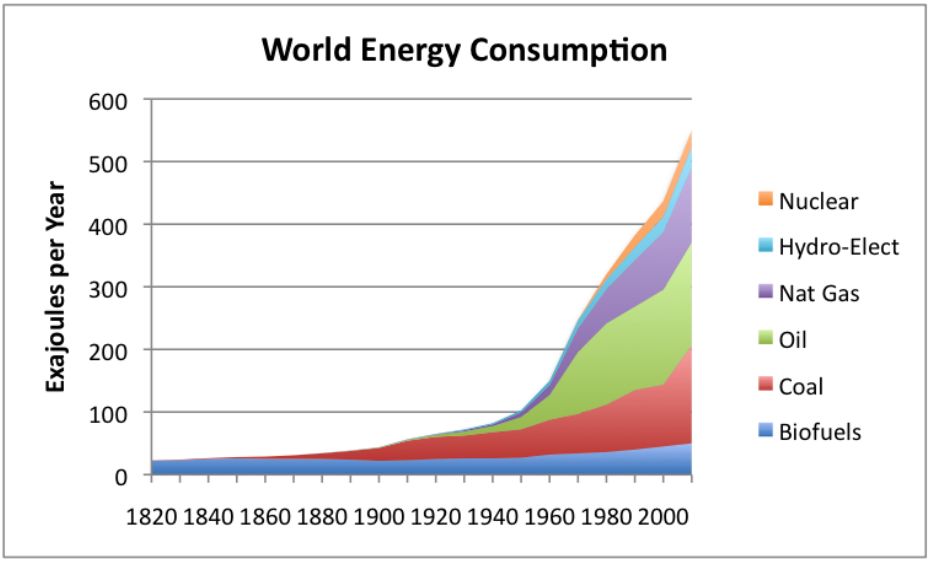

Figure 1.1 World Energy Consumption by source based on estimates from energy transitions: history, requirements and prospects [3].

Rapid technological development in the last century has led to increased pollution from using fossil fuels. This emission has resulted in an increase in the global surface temperature of 0.6 °C over the past century, and if the global surface temperature rise with 4°C, the result can be disastrous. Combustion of fossil fuel is responsible for the increase in CO_2 emission from 300 ppm to 360 ppm from 1860 to 1995. In order to limit temperature increase to 1 °C, the concentration of CO_2 in the atmosphere should not exceed 450 ppm [4]. Figure 1.2 illustrates the rise in CO_2 emission versus the growth of the energy use. It is clear that the energy consumption and CO_2 emission have increased in a similar manner from 1965 to today.

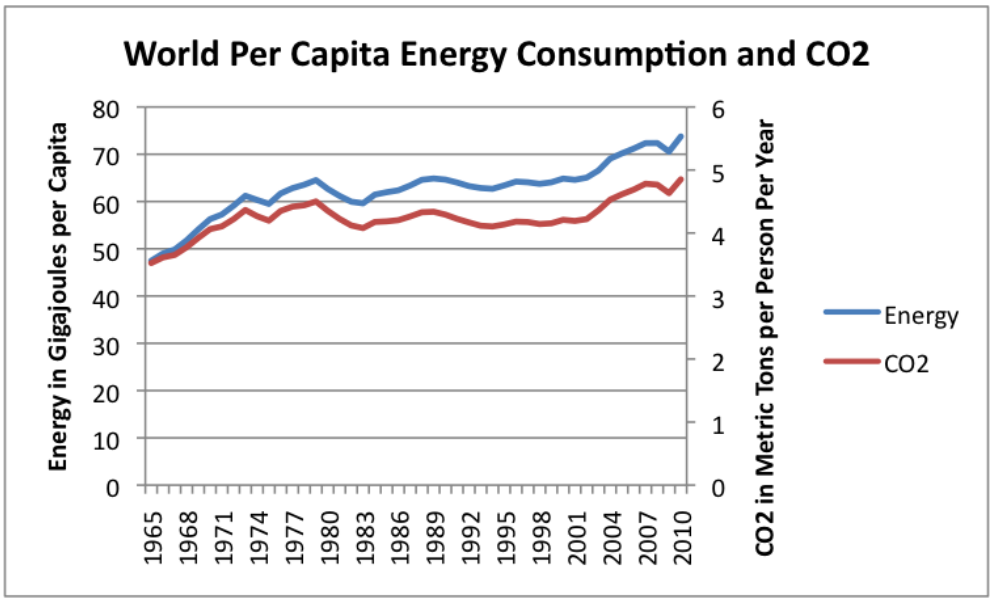

Figure 1.2 Per capita energy consumption and CO_2 emissions, based on BP statistics data [3]

The increasing world populations, the global energy demand and limitation of the fossil fuels resources require renewable and environmental friendly energy technologies to be developed. The alternative energy sources such as a solar energy, wind energy and energy of tide water are making progress. One of the ways to utilize H_2 after producing it from renewable energy is using fuel cells. Fuel cell technology is one of the promising solutions to the global energy demand. Fuel cell was discovered over a century ago and is a device that converts chemical energy to electricity. Fuel cell generates electricity and heat via an electrochemical reaction between hydrogen and oxygen to form water, and is therefore environmentally friendly. Fuel cells exhibit higher efficiency up to 65% [5], compared to conventional energy systems. Fuel cells can, generally, be classified by means of the electrolyte material and their

application depends on the type of fuel to be used (e.g. hydrogen, syngas, methane, natural gas). Even if there is a range of different fuel cells they all operate with the same basic principle. The fuel cell consists of anode and cathode, separated with an electrolyte, and the external circuit. At the anode, the hydrogen is oxidized into protons and electrons, while at the cathode oxygen is reduced to oxide ions [5]. Whether the electrolyte transports protons or oxygen ions and where water forms depend on the electrolyte. The electrons travel through an external circuit to deliver electrical power [5].

Among different types of fuel cells, solid oxide fuel cell (SOFC) with a ceramic electrolyte is one of the most promising types to operate at high temperature.

1.2 Proton conducting fuel cells

SOFCs may be divided into two subclasses: SOFC where oxide ions diffuse across the electrolyte and proton conducting SOFC (PC-SOFC) where protons are the migrating species. In traditional SOFCs the oxygen ions migrate through the solid electrolyte from the cathode to the anode, where they react with the fuel (H_2, CH_4) and produce water. These types of fuel cells require high temperature (~ 500-1000 °C), which are suffered by materials stability problem, but at the same time they are relatively tolerant to carbonaceous fuels and their impurities [6].

However, SOFCs with proton conducting electrolytes have also attracted interest. In such fuel cells the hydrogen is oxidized to form protons, which migrate across the solid electrolyte to form water at the cathode side (Figure 1.3). The main advantage of such proton conducting SOFC (PC-SOFC) is that water vapor is produced at the cathode side, thus avoiding fuel dilution. The PC-SOFC operate at lower temperature (~400-800 °C) and provides an opportunity to increase the hydrogen partial pressure at the anode side, in this way increasing the system efficiency [7].

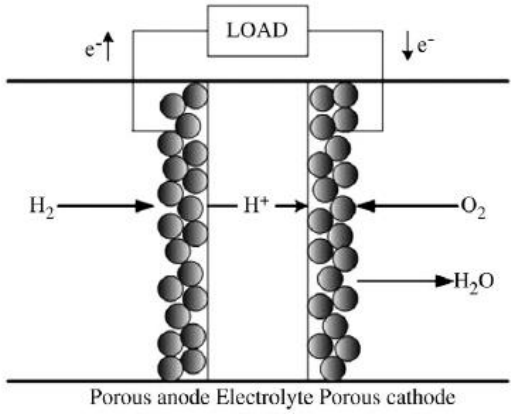

Figure 1.3. The schematic of a proton-conducting solid oxide fuel cell [7].

However, stability, performance and material properties are far from being competitive at present and need to be improved in order for SOFCs to become fully commercialized. Several challenges especially regarding stability and finding high performing compatible electrodes must be solved [6].

1.3 Gas separation membranes

Recycling and purification of hydrogen is one of the most important ways to satisfy the growing demand for hydrogen in accordance with the new environmental - friendly standards. Among different technologies of gas separation, membrane technology seems to be the most promising. The membranes for hydrogen separation differ in the nature and structure and can be classified into the following categories: polymeric membranes, porous membranes, dense metal membranes and proton conducting membranes [8]. Among all the existing potential materials for hydrogen separation membranes, non-perovskite-type dense ceramic membranes with mixed ionic-electronic conducting properties are of interest for membrane applications [9]. For such membranes, the ambipolar proton – electron conductivity, at temperatures as high as 900 °C, is the essential parameter [8, 10]. Figure 1.4 shows a schematic use of a gas separation system, consisting of an oxygen and hydrogen membranes. It illustrates how the oxygen and hydrogen permeable membranes can be used together in a combination process of partial oxidation and hydrogen extraction [10].

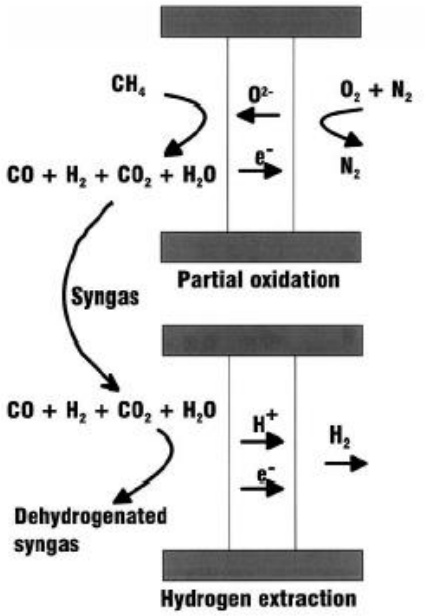

Figure 1.4. Schematic use of mixed oxygen ion – electronic conductor for oxygen separation, followed by use of mixed protonic-electronic conductor for hydrogen extraction.[10]

The driving force of such membranes is a hydrogen partial pressure gradient. Dense ceramic membranes should obtain high protonic and electronic conductivities in order to obtain a high hydrogen flux [8].

1.4 Objective of the thesis

Several potential proton conducting electrolyte materials have been discovered, among which some with perovskite structure exhibit high protonic conductivity, around 0.01 S/cm [11]. One of the main challenges with these perovskite based PCFC electrolyte materials is their low stability in CO_2 and SO_2/SO_3 containing atmospheres, making them vulnerable towards degradation. The reason for this is elements like Ba in $BaCeO_3$ and $BaZrO_3$, which have a basic character and tend to react with acidic gases [6]. Outside the perovskite structure, there are some recently discovered materials where proton conductivity was confirmed, and LWO is one of them [11, 12]. This material exhibits relatively high proton conductivity at moderate temperatures, with a maximum in proton conductivity of ~0.005 S/cm in wet hydrogen at ~900 °C [9]. Lanthanum tungstate exhibits stability against water vapor and CO_2 gas, which makes them a promising electrolyte candidates [13].

Although this oxide is chemically stable, it shows relatively lower conductivities, compared to the best perovskite materials, and the conductivity remains as the major limitation for use in technological applications such as in a PC-SOFC electrolytes. Consequently, the conductivity of lanthanum tungstate should preferably be improved before components of this material can be realized for technological application.

The primary goal of this master thesis is to study the effect on the conductivity of LWO upon cerium substitution of lanthanum in LWO54. Cerium was chosen as a dopant because it has a similar ionic radii ($r_{Ce^{4+}}$ = 0.97 Å, $r_{La^{3+}}$ = 1.16 Å [14]) and chemical properties as those of lanthanum.

Previous studies demonstrated that LWO has an inherently disordered structure, meaning that a sublattice is randomly occupied by oxide ions and oxygen vacancies [15]. Donor doping of LWO can contribute to the annihilation of oxygen vacancies and formation of oxygen ions:

$$V_{\frac{54}{56}O}^{\frac{108}{56}\bullet} + \frac{1}{2}O_2 + 2Ce_{La}^{X} = O_{\frac{54}{56}O}^{\frac{4}{56}/} + 2Ce_{La}^{\bullet} \qquad (1.1)$$

The studies will be performed on 2Ce-LWO and 5Ce-LWO, 2%Ce- and 5%Ce-doped LWO54 respectively. The samples will be synthesized by a wet-chemical gelation method and characterized by X-Ray diffraction (XRD), scanning electron microscopy (SEM) and electron probe micro-analysis (EPMA). The electrical measurements as a function of temperature, oxygen partial pressure and water vapor pressure will be performed for both samples. Thermogravimetric measurements will be used to study the hydration of the material and estimate the thermodynamic parameters. Based on these studies, the effect of donor doping on the conductivity of LWO54 will be discussed and the defect model will be determined. Based on the defect model and the total conductivity measurements, the transport and thermodynamic parameters will be estimated from curve fitting.

These studies will contribute to better understanding of the nature of LWO and other rare-earth tungstates, which is important to achieve a good proton conducting electrolyte or hydrogen separation membrane.

2 Theory

This part includes the basic principles of defect chemistry of lanthanum tungstate oxide, and the theory behind the electrical measurements.

2.1 Defect Chemistry

The theory of defect chemistry presented herein is based on Defects and Transport in Crystalline Solids by Per Kofstad and Truls Norby[16].

2.1.1 Defects and notations

In all crystalline materials atoms and ions are arranged orderly in all three spatial dimensions. At the temperatures above 0 K, the deviations from the ideal structure will occur in a form of defects. Defects and defect chemistry can explain many different phenomena that can be observed in solids. A lot of lattice properties depend on the type and concentration of the defect. There are several types of defects, depending on their dimension. Zero-dimensional defects are point defects and they are referred to imperfection which is limited to one lattice site. One-dimensional defects are line defects which comprise dislocations, while two-dimensional defects are plane defects. Table 2.1 summarizes the structural defects and gives examples for each of them.

Table 2.1. Types of structural defects in a crystalline material

Dimension	Examples
0- Dimension	Vacancies, interstitials atoms, substitutions
1- Dimension	Dislocations
2- Dimension	Grain boundaries, internal and external interfaces
3-Dimension	Pores, voids, precipitations of secondary phase

Figure 2.1 shows a schematic representation of different type of defects that can appear in a crystal.

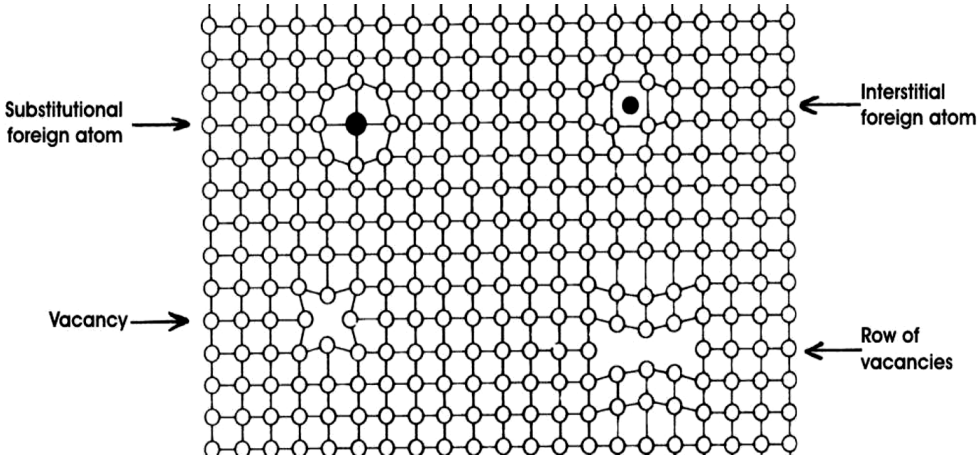

Figure 2.1 A crystal structure with different types of point defects [16]

In addition to the structural defects such as vacancies, interstitial atoms and substitutional atoms (Figure 2.1), a crystal also contains electronic defects, i.e. electrons and electron holes. The electronic defects may be formed either through internal excitation or in association with point defects. A complete description of point and electronic defects in a crystal together with their concentrations as a function of partial pressures determines the defect structure of the compound.

In order to describe the concentrations of defects under different conditions and to express defect formation into chemical equations, a system of notations requires. The most widely used system to classify the point defects is the Kröger-Vink notation. This notation describes point defects as A_s^c, where *A* in the chemical symbol for the species, *s* corresponds to the lattice site that the species occupies and *c* is an effective charge of the species, which in turn is a difference between the real charge of the defect and the real charge of the site occupied and can be negative (/), positive (•) or neutral (x).

The defects caused by ions in the material called ionic defects. Electronic defects electrons and electron holes, mentioned above, expresses as e' and $h^{\bullet}$ respectively. Table 2.2 shows the notation for some defects that are relevant for this thesis.

Table 2.2. Relevant Kröger-Vink notations for some defects relevant for this thesis.

Defect	Kröger-Vink notation
Metal on metal site	La_{La}^{X}
Metal substitution	$W_{La}^{\bullet\bullet\bullet}, Ce_{La}^{\bullet}$
Oxygen on oxygen site	O_{O}^{X}
Oxygen vacancy	$v_{o}^{\bullet\bullet}$
Defect electron	$e^{/}$
Electron hole	$h^{\bullet}$
Hydroxide ion on oxygen site	$OH_{O}^{\bullet}$

2.1.2 Defect thermodynamics and equilibrium

The formation of defects can occur through reaction with the surroundings. The rules for writing defect reactions are similar to ordinary chemical reactions and can be summarized as follows:

Conservation of mass – the total number of atoms involved in the reaction must be the same before and after the formation of defect.

Conservation of charge – the total effective charge must remain the same before and after the formation or annihilation of the defect.

Conservation of the ratio of structures sites – the number of anion sites proportional to the number of cation sites must remain the same before and after the formation or annihilation of the defect.

Equilibrium

Defect reactions can be treated the same way as chemical reactions and hence follow the same thermodynamical rules.

A reaction of a defect formation can be simply written as:

$$aA + bB = cC + dD \tag{2.1}$$

The equilibrium constant can be determined by the ratio of activity (α) of products and reactants:

$$K = \frac{\alpha_C^c \, \alpha_D^d}{\alpha_A^a \, \alpha_B^b} \tag{2.2}$$

Considering the defect formation in a crystal as a closed system, the Gibbs free energy of the reaction will be expressed as:

$$\Delta G = \Delta G^0 + RT \ln K \tag{2.3}$$

Where ΔG^0a free energy in standard state, R is the gas constant, T is the temperature and K is the equilibrium constant. The Gibbs free energy change is zero at equilibrium, hence

$$\Delta G^0 = -RT \ln K \tag{2.4}$$

The standard Gibbs energy change can be expressed in terms of the standard enthalpy change (ΔH^0) and standard entropy change (ΔS^0), so that

$$\Delta G^0 = \Delta H^0 - T\Delta S^0 = -RT \ln K \tag{2.5}$$

Solving reaction (2.5) with respect to the equilibrium constant K yields:

$$K = \exp\left(-\frac{\Delta G}{RT}\right) = \exp\left(\frac{\Delta S^0}{R}\right)\exp\left(-\frac{\Delta H^0}{RT}\right) \tag{2.6}$$

Equation 2.6 expresses the equilibrium constant K and can be applied to all the defect reactions.

2.1.3 Defects in oxides

In an oxide, many types of defects can exist, but only a small number of them can predominate. A formation of a charged point defect, accompanies with a formation of a complementary point defect with opposite effective charge with respect to electroneutrality of the stoichiometric crystal.

Defects formed as a result of internal equilibrium without interaction with the environment are called intrinsic defects. In stoichiometric oxides, two most common stoichiometric defects are *Schottky* and *Frenkel* disorders.

Under Schottky disorder, vacancies of both cations and ions are formed. In $MMeO_4$ ($M^{3+}Me^{5+}O_4$) two cation vacancies and four anion vacancies can be formed:

$$0 = V_M^{///} + V_{Me}^{5/} + 4\,V_O^{\bullet\bullet} \tag{2.7}$$

A crystal with Frenkel disorder contains the same concentration of cation (metal) vacancies as interstitials:

$$M_M^X = V_M^{///} + M_i^{\bullet\bullet\bullet} \tag{2.8}$$

In some oxides, anion-Frenkel (anti-Frenkel) disorder can be formed. This occurs when an anion (oxygen) goes into in interstitial site:

$$O_O^X = V_O^{\bullet\bullet} + O_i^{//} \tag{2.9}$$

These two defects can simultaneously be present in stoichiometric compounds, while only one usually predominates. Frenkel disorder predominates when the sizes of the anions and cations are quite different.

Another type of stoichiometric defects is electronic defects. These defects are caused by an excitation from the valence band to the conduction band and have the follow reaction:

$$0 = e' + h^{\bullet} \tag{2.10}$$

The equilibrium constant for the intrinsic ionization:

$$K_i = np \tag{2.11}$$

Defects formed due to reaction with the environment denoted *extrinsic defects*. The oxide that reacts with surrounding called a non-stoichiometric compound. The oxide can have an excess or deficit of oxygen or metal, which depends on the temperature and a crystal structure. In a close packed structure (such as LWO), formation of oxygen vacancies will be favorable. With regard to oxygen, formation of defects can occur by reducing or oxidizing processes.

At low oxygen partial pressure, oxygen vacancies and electrons can be formed:

$$O_O^X = V_O^{\bullet\bullet} + 2e' + \frac{1}{2}O_{2(g)} \tag{2.12}$$

where $[V_O^{\bullet\bullet}]$, n and p are the concentrations of vacancies, electrons and electron holes respectively. This process is called reduction and the corresponding equilibrium coefficient K_{red}, is derived:

$$K_{red} = \frac{[V_O^{\bullet\bullet}]}{[O_O^X]}\left(\frac{n}{N_c}\right)^2\left(\frac{p_{O_2}}{p_{o_2}^0}\right)^{1/2} \tag{2.13 -a}$$

where N_c is density of state of electrons, $p_{o_2}^0$ is the standard state of a gas which is 1 bar, and $[O_O^X]$ is the standard concentration of the oxygen ions at full occupancy, which with small defect concentration in an oxide is assumed to be 1. The density of state of electrons (and electron holes) is common to neglect as long as electrons or electron holes are not predominating defect in an oxide. These assumptions will be used hereafter in the calculations and formula derivations. The equilibrium coefficient of the reduction process becomes:

$$K_{red} = [V_O^{\bullet\bullet}]n^2\left(p_{O_2}\right)^{1/2} \tag{2.13 -b}$$

At high oxygen partial pressure, vacancies will be consumed and electron holes created:

$$\frac{1}{2}O_{2(g)} + V_O^{\bullet\bullet} = O_O^X + 2h^{\bullet} \tag{2.14}$$

This process is called oxidation and the corresponding equilibrium constant K_{ox} expresses as:

$$K_{ox} = [V_O^{\bullet\bullet}]^{-1} p^2 p_{O_2}^{-1/2} \tag{2.15}$$

Equation 2.13 and Equation 2.15 show that the concentration of electrons, electron holes and oxygen vacancies are dependent on the partial pressure of oxygen.

Extrinsic defects are also formed when a foreign atom is introduced to the structure, so-called doping. When the valence of this atom is different from that of the host, the doping is termed heterovalent. Heterovalent doping can be divided into donor and acceptor doping, where an ion with higher or lower valence respectively is substituted for the parent cation.

If a foreign cation is a higher-valent dopant, the effective charge will be positive and the material will be donor-doped. When Mh^{4+} dissolves substitutionally into an oxygen-deficient oxide M_2O_{3-x}, the dissolved cation has one positive effective charge, $Mh_M^{\bullet}$. The positive effective charge will be compensated either by formation of negative effective charges in form of electrons (2.16), or by annihilation of positive effective charges in form of oxygen vacancies (2.17) which depends on the properties of the oxide, the temperature and the oxygen activity.

$$MhO_2 = Mh_M^{\bullet} + e' + O_O^X + \frac{1}{2}O_2(g) \tag{2.16}$$

$$MhO_2 + \frac{1}{2}V_O^{\bullet\bullet} = Mh_M^{\bullet} + 2O_O^X \tag{2.17}$$

In the case when the concentration of dopant is below the solubility limit of the solid, the doping concentration is constant and the system is stable, otherwise a solute-rich phase of solute precipitates in grain boundaries and surfaces.

2.1.4 Hydrogen defects in metal oxides

When metal oxides are in the equilibrium with hydrogen-containing gases as $H_{2(g)}$ or $H_2O_{(g)}$, hydrogen may dissolve into the solid structure in the form of a proton (H•). These protons will associate with oxide ions as hydroxide groups and create substitutional hydroxide defects, $OH_O^{\bullet}$. When hydrogen gas is the source, the dissolution of protons can be written as

$$H_{2(g)} + 2O_O^X = 2OH_O^{\bullet} + 2e' \quad (2.18)$$

The concentration of protons in this case depends in the hydrogen partial pressure and according to Le Châtelier principle high hydrogen partial pressure will shift the equilibrium to the product side.

In the presence of water, protonic defects can form in an oxide. This can occur through one of the hydration reactions:

$$H_2O_{(g)} + 2O_O^X = 2OH_O^{\bullet} + 2e' + \frac{1}{0}O_2(g) \quad (2.19)$$

or

$$H_2O(g) + O_O^X + V_O^{\bullet\bullet} = 2OH_O^{\bullet} \quad (2.20)$$

The concentration of protons for the hydration reaction now is both dependent on the water vapor pressure and oxygen vapor pressure. Reaction 2.19 is not favor in many oxides therefore not frequently observed. The formed electrons can easily interact with other defects in the oxide, so that the protons will be compensated by formation of other negative defect or by annihilation of positive defects.

The hydration reaction is generally exothermic, which means that the hydration enthalpy, ΔH_{hydr}^0 is negative and the reaction will be driven towards the reactants (the left) at sufficiently high temperature. Protons accordingly tend to predominate at low temperatures, while at high temperatures the concentration of oxygen vacancies predominates. The hydration reaction 2.20 is of great importance for understanding of the hydration mechanism i.e. water vapor dissolves to fill the oxygen vacancies and

replace their positive charge with protons, creating two protonic defects for each water molecule.

The equilibrium constant of hydration process K_{hydr} can be expressed as:

$$K_{hydr} = \exp\left(-\frac{\Delta G^{O}_{hydr}}{RT}\right) = \exp\left(\frac{\Delta S^{O}_{hyrd}}{R}\right)\exp\left(-\frac{\Delta H^{O}_{hyrd}}{RT}\right) \quad (2.21)$$

where ΔH^{O}_{hyrd} – hydration enthalpy and ΔS^{O}_{hyrd} – hydration entropy.

2.2 Defect Chemistry in LWO

2.2.1 Kröger-Vink compatible notation for LWO

The structure of undoped LWO can be described either as an ordered defective fluorite or a disordered pyrochlore [9, 17, 18]. The defect model for this material is based on the inherently deficient disordered oxygen sublattice. In addition to the intrinsic oxygen vacancies in the structure, there is an intrinsic substitution of tungsten on lanthanum sites [15] (a more detailed description of the crystal structure is presented in subsection 3.1.1).

Generally, a formula unit of LWO is written as [15]:

$$\boldsymbol{La_{28-x}W_{4+x}O_{54+1,5x}v_{2-1,5x}} \quad \text{(Unit cell 1)}$$

where *x* value quantifies W on La sites, and *v* indicate the vacant site that can by occupied by oxygen. This value, when it is not zero, creates internal positive defect, $W_{La}^{\bullet\bullet\bullet}$. The perfect structure without this defect corresponds to *x = 0,* and refers to a parent structure:

$$\boldsymbol{La_{28}W_4O_{54}v_2} \quad \text{(Unit cell 2)}$$

The formula units presented above, correspond to the unit cells of the structures (see Figure 3.1 in subsection 3.1.1). Since the disorder is a part of structure, we get a new

nomenclature for Kröger-Vink notations [19]. In this structure, where 54 oxygens occupy 56 oxygen sites, there are 54/56 oxide ions and 2/56 vacancies. This changes the defects charge. Each oxide ion, occupying 54/56 site, has a formal charge of - 2, so that 54/56 oxygen sites have a formal charge of $-2 * \frac{54}{56} = -\frac{108}{56}$. The oxide ion, which has a real charge of - 2, now has an effective charge of $-2 - (-\frac{108}{56}) = -\frac{4}{56}$. Oxide ions are thus denoted in the modified Kröger-Vink notation: $O_{\frac{54}{56}O}^{\frac{4}{56}/}$. The vacancy has a real charge of zero, so now its effective charge is $0 - \left(-\frac{108}{56}\right) = \frac{108}{56}$, and the oxide ion vacancy is thus denoted: $V_{\frac{54}{56}O}^{\frac{108}{56}\bullet}$. Table 2.3 summarizes modified Kröger-Vink notations for LWO.

Table 2.3. Modification of Kröger-Vink notation for $La_{28-x}W_{4+x}O_{54+1,5x}v_{2-1,5x}$ structure.

Standard Kröger-Vink notation	Modified Kröger-Vink notation
$\mathbf{O_O^X}$	$O_{\frac{54}{56}O}^{\frac{4}{56}/}$
$\mathbf{v_o^{\bullet\bullet}}$	$V_{\frac{54}{56}O}^{\frac{108}{56}\bullet}$
$\mathbf{OH_O^{\bullet}}$	$OH_{\frac{54}{56}O}^{\frac{52}{56}\bullet}$

2.2.2 Electroneutrality Condition

LWO is dominated by inherent oxygen disorder and intrinsic donor doping when stoichiometric. The concentration of these defects in the lattice depends on the nominal ratio between lanthanum and tungsten ions. The inherent vacant oxygen position in the structure yields the redistribution of the effective negative charge, making oxygen vacancies less positive and oxygen ions negative (Table 2.3).

The total electroneutrality condition for lanthanum tungstate can then be written as [15]:

$$\frac{108}{56}\left[V_{\frac{54}{56}O}^{\frac{108}{56}\bullet}\right] + 3[W_{La}^{\bullet\bullet\bullet}] + \frac{52}{56}\left[OH_{\frac{54}{56}O}^{\frac{52}{56}\bullet}\right] + p = \frac{4}{56}\left[O_{\frac{54}{56}O}^{\frac{4}{56}/}\right] + n \quad (2.22)$$

where *n* and *p* are the concentrations of electrons and electron holes respectively. The concentration of last mentioned defects is assumed negligible compared to the ionic defects. The electroneutrality condition for $La_{28}W_4O_{54}v_2$ with no tungsten on lanthanum site becomes:

$$\frac{108}{56}\left[V_{\frac{54}{56}O}^{\frac{108}{56}\bullet}\right] + \frac{52}{56}\left[OH_{\frac{54}{56}O}^{\frac{52}{56}\bullet}\right] + p = \frac{4}{56}\left[O_{\frac{54}{56}O}^{\frac{4}{56}/}\right] + n \quad (2.23)$$

The total electroneutrality condition for the hydration process described by the Equation 2.21:

$$\frac{108}{56}\left[V_{\frac{54}{56}O}^{\frac{108}{56}\bullet}\right] + \frac{52}{56}\left[OH_{\frac{54}{56}O}^{\frac{52}{56}\bullet}\right] = \frac{4}{56}\left[O_{\frac{54}{56}O}^{\frac{4}{56}/}\right] \quad (2.24)$$

A particular type of defects usually predominates in the oxide. The dominating defects can change with temperature and activity of the components in the crystal. In addition to the defects presented by Equation 2.24, the crystal can also contain some other minority defects that are not of a big importance in this thesis.

Using the electroneutrality condition and a set of defect equations under reducing/ oxidizing conditions and their corresponding equilibrium expressions, a Brower diagram can be constructed. This diagram graphically presents the logarithm of the defect concentration plotted against the logarithmic oxygen partial pressure p_{O_2} or water partial pressure p_{H_2O}. The Brower diagram can be used for the interpretation of the conductivity trends in the material.

2.2.3 Concentration of defects as a function of p_{O_2}

The concentration of point defects depends on oxygen partial pressure as described by Equation 2.12 and Equation 2.14. For LWO the same rules apply with the modification of Kröger-Vink notation as mentioned at Table 2.3.

At the stoichiometric region, the site occupancy sum of oxygen ions and oxygen vacancies in terms of molar fraction for $La_{28}W_4O_{54}v_2$ is always constant [15, 19, 20]:

$$\left[O_{\frac{54}{56}O}^{\frac{4}{56}/}\right] + \left[V_{\frac{54}{56}O}^{\frac{108}{56}\bullet}\right] = 56 \tag{2.25}$$

Assuming that these two defects are the only predominant at the stoichiometric condition, and the electrons and holes are the minority defects, the fraction of the concentration of these two defects will be expressed as:

$$\left[O_{\frac{54}{56}O}^{\frac{4}{56}/}\right] = 27\left[V_{\frac{54}{56}O}^{\frac{108}{56}\bullet}\right] \tag{2.26}$$

At low oxygen partial pressure, reduction may predominate, and oxygen vacancies and electrons will be created:

$$O_{\frac{54}{56}O}^{\frac{4}{56}/} = V_{\frac{54}{56}O}^{\frac{108}{56}\bullet} + 2e^{/} + \frac{1}{2}O_2(g) \tag{2.27}$$

The corresponding equilibrium coefficient of the reduction:

$$K_{red} = \left[V_{\frac{54}{56}O}^{\frac{108}{56}\bullet}\right]\left[O_{\frac{54}{56}O}^{\frac{4}{56}/}\right]^{-1} n^2 p_{O_2}^{1/2} \tag{2.28}$$

At high oxygen partial pressure, oxidation may predominate, and the oxygen vacancies will be used to create electron holes:

$$\frac{1}{2}O_{2(g)} + V_{\frac{54}{56}O}^{\frac{108}{56}\bullet} = O_{\frac{54}{56}O}^{\frac{4}{56}/} + 2h^{\bullet} \tag{2.29}$$

The corresponding equilibrium coefficient for these conditions:

$$K_{ox} = \left[O_{\frac{54}{56}O}^{\frac{4}{56}/}\right]\left[V_{\frac{54}{56}O}^{\frac{108}{56}\bullet}\right]^{-1} p^2 p_{O_2}^{-1/2} \tag{2.30}$$

The combination of Equation 2.26, Equation 2.28 and Equation 2.30 gives the dependency of oxygen partial pressure for the electrons and holes under stoichiometric conditions:

$$n = (27K_{red})^{\frac{1}{2}} p_{O_2}^{-\frac{1}{4}} \tag{2.31}$$

$$p = (\frac{1}{27}K_{ox})^{\frac{1}{2}} p_{O_2}^{\frac{1}{4}} \tag{2.32}$$

At non-stoichiometric regions the oxygen ions and oxygen vacancies are not predominating defects anymore, and Equation 2.26 is not relevant.

At sufficiently low oxygen partial pressure Equation 2.27 will expresses the defect situation. The electroneutrality condition for this region becomes:

$$\frac{108}{56}\left[V_{\frac{54}{56}O}^{\frac{108}{56}\bullet}\right] = n + \frac{4}{56}\left[O_{\frac{54}{56}O}^{\frac{4}{56}/}\right] \tag{2.33}$$

According to Le Châtelier principle, the equilibrium of Equation 2.27 at low oxygen partial pressure will be shifted towards the product side, making oxygen vacancies and electrons the majority defects in this region. The reduced electroneutrality condition becomes:

$$n = \frac{108}{56}\left[V_{\frac{54}{56}O}^{\frac{108}{56}\bullet}\right] \tag{2.34}$$

According to Equation 2.27 the reduction in concentration of oxygen ions is accompanied by the increase of concentration of oxygen vacancies and electrons. The concentration of oxygen vacancies and electrons cannot exceed the limited value of the oxide, as thus the compound will get metallic properties.

At sufficiently high oxygen partial pressure Equation 2.29 will expresses the defect situation. The electroneutrality condition for this region becomes:

$$\frac{108}{56}\left[V_{\frac{54}{56}O}^{\frac{108}{56}\bullet}\right] = p + \frac{4}{56}\left[O_{\frac{54}{56}O}^{\frac{4}{56}/}\right] \tag{2.35}$$

Negative oxygen ions and its compensating positive electron holes will predominate in this region and the reduced electroneutrality condition become:

$$p = \frac{4}{56}\left[O_{\frac{54}{56}O}^{\frac{4}{56}/}\right] \tag{2.36}$$

According to Equation 2.29, the oxygen vacancies will be oxidized to the oxygen sites. The increased concentration of oxygen ions cannot exceed the limited value of the oxygen sites in the oxide, which is 56, as thus the decompositions of the compound may take place.

These nonstoichiometric situations are extreme situations for this compound, and not relevant to this thesis, therefore will not be detail discussed.

The p_{O_2} dependencies of the different point defect concentrations in the three regions are summarized in a Brower diagram:

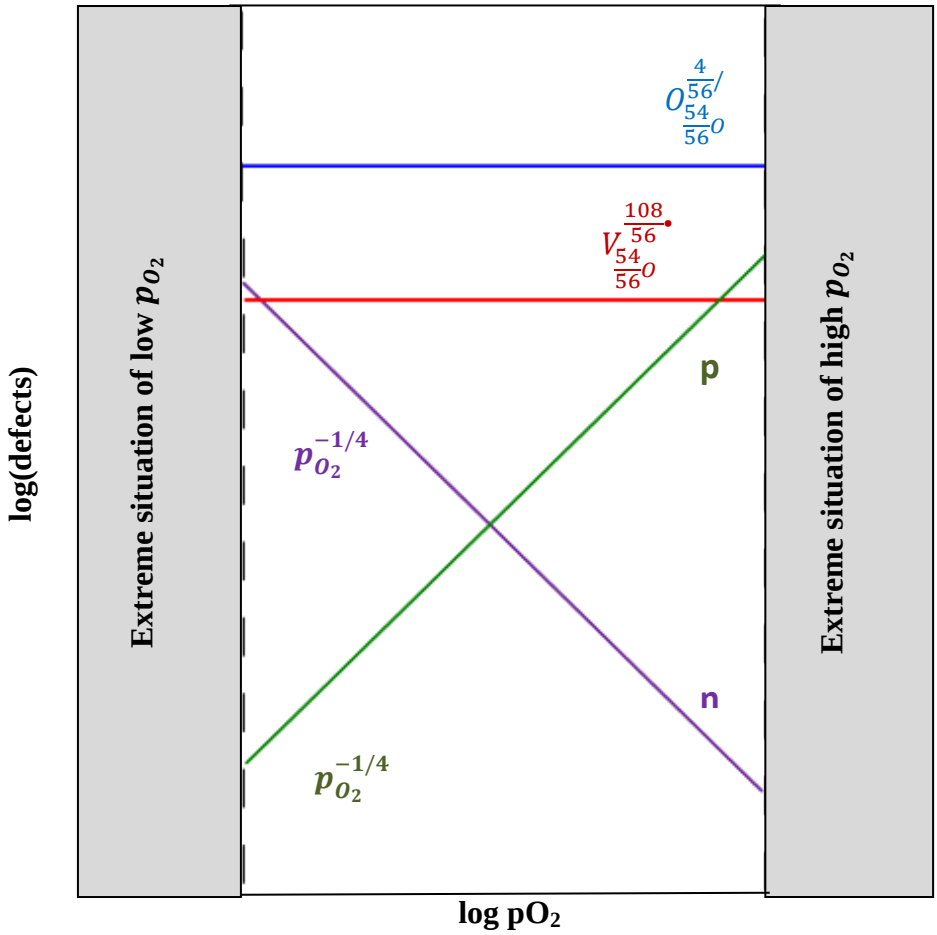

Figure 2.2. The Brower diagram of $La_{28}W_4O_{54}v_2$ shows the concentration of point defects as a function of p_{O_2}.

2.2.4 Concentration of defects as a function of p_{H_2O}

The defects can also depend on the partial pressure of water vapor. From the general hydration reaction (Equation 2.20) the increase in p_{H_2O} at constant p_{O_2} will result in the formation of protonic defect. For LWO the same rules apply with the modification Kröger-Vink notation as mentioned in Table 2.3:

$$H_2O + V_{\frac{54}{56}O}^{\frac{108}{56}\bullet} + O_{\frac{54}{56}O}^{\frac{4}{56}/} = 2OH_{\frac{54}{56}O}^{\frac{52}{56}\bullet} \quad (2.37)$$

The equilibrium coefficient of hydration:

$$K_{hyd} = \frac{\left[OH_{\frac{54}{56}O}^{\frac{52}{56}\bullet}\right]^2}{\left[O_{\frac{54}{56}O}^{\frac{4}{56}/}\right]\left[V_{\frac{54}{56}O}^{\frac{108}{56}\bullet}\right]p_{H_2O}} \tag{2.38}$$

The total electroneutrality condition for the hydration process is expressed by Equation 2.24.

Under relatively dry conditions (low p_{H_2O}), according to Le Châtelier principle, the equilibrium of Equation 2.37 will be shifted towards oxygen vacancies. The reduced electroneutrality condition in this region is similar to one expressed by Equation 2.26: $\left[O_{\frac{54}{56}O}^{\frac{4}{56}/}\right] = 27\left[V_{\frac{54}{56}O}^{\frac{108}{56}\bullet}\right]$, which corresponds to the stoichiometric condition described earlier. The concentration of protons will be expressed as:

$$\left[OH_{\frac{54}{56}O}^{\frac{52}{56}\bullet}\right] = (27K_{hyd})^{1/2}\left[V_{\frac{54}{56}O}^{\frac{108}{56}\bullet}\right]p_{H_2O}^{1/2} \tag{2.39}$$

As the water vapor pressure becomes dominating, the protonic defects take over for the oxygen vacancies, and the reduced electroneutrality becomes:

$$\frac{52}{56}\left[OH_{\frac{54}{56}O}^{\frac{52}{56}\bullet}\right] = \frac{4}{56}\left[O_{\frac{54}{56}O}^{\frac{4}{56}/}\right]. \tag{2.40}$$

In this region, the oxygen vacancies become the minority defects, and their concentration is found by the substitution Equation 2.40 into Equation 2.38:

$$\left[V_{\frac{54}{56}O}^{\frac{108}{56}\bullet}\right] = \left(\frac{1}{13K_{hyd}}\right)p_{H_2O}^{-1} \tag{2.41}$$

The concentration of oxygen ions is constant in this region, but lower compared to the region under dry conditions.

The p_{H_2O} dependencies of the different point defect concentrations in the two regions are summarized in the Brower diagram:

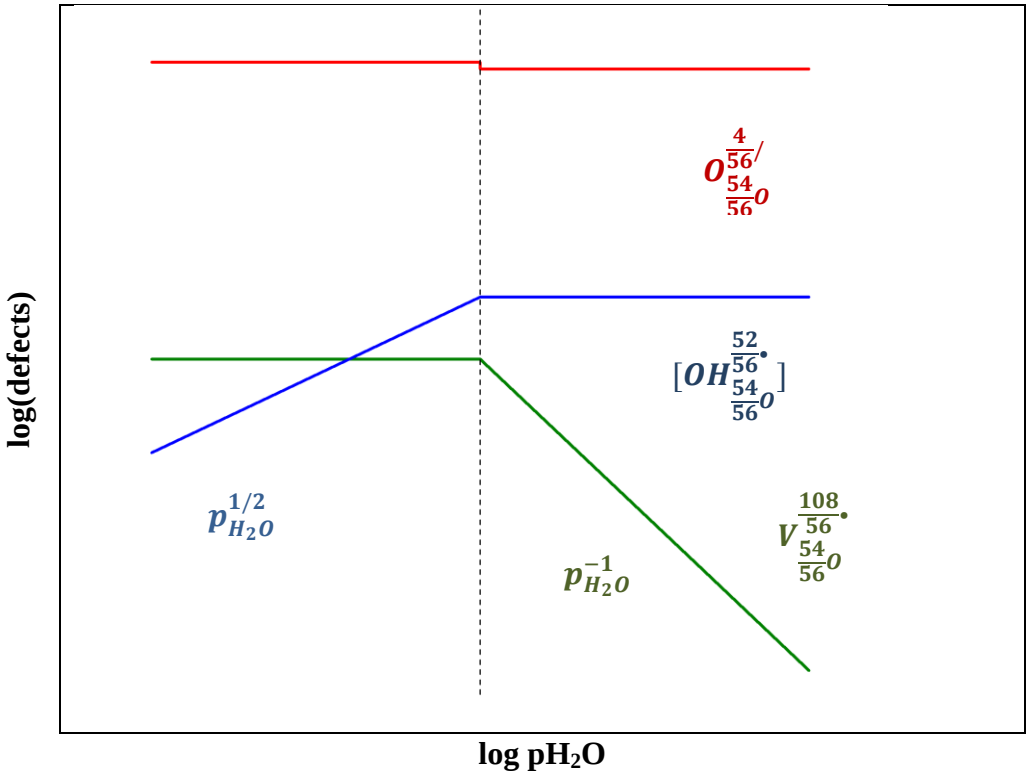

Figure 2.3. The Brower diagram of $La_{28}W_4O_{54}v_2$ shows the concentration of point defects as a function of p_{H_2O}.

2.3 Defect Chemistry in donor doped LWO

The ratio between lanthanum and tungsten in LaWO was chosen to be 5.4, which corresponds to *x=1* (unit cell 1). As it was explained above, this value means the concentration of positive intrinsic defect in the unit cell, created by substitution of lanthanum by tungstate. As the amount of oxygen and oxygen vacancies vary with this ratio, the formula unit of LWO with La/W = 5.4 becomes:

$$\boldsymbol{La_{27}W_5O_{55.5}v_{0.5}} \qquad \text{(Unit cell 3)}$$

The electroneutrality condition for this variation of LWO remains the same (Equation 2.22), but at the stoichiometric condition the appearance of positive intrinsic dopant leads to transformation of some positive oxygen vacancies to negative oxygen sites. In the Brower diagram this results in higher concentration of the negative oxygen ions and lower concentration of the positive oxygen vacancies under the stoichiometric condition. The dependencies of all defects as a function of the partial pressure of oxygen and water remain the same as was described above. The concentration of the intrinsic donor dopant is constant and does not change under different atmospheres.

For Ce-doped $La_{27}W_5O_{55.5}v_{0.5}$, the defect structure is based on that of $La_{28}W_4O_{54}v_2$ described above, with an additional substitution of Ce on La site, which creates a positive defect $Ce_{La}^{\bullet}$. The compensation of this defect can be done by increasing of negative oxygen on oxygen sites, which decreases a concentration of oxygen vacancies or by decreasing the intrinsic donor substitution of tungstate on lanthanum site. The electroneutrality condition is based on Equation 2.22 with an additional positive defect:

$$[Ce_{La}^{\bullet}] + \frac{108}{56}\left[V_{\frac{54}{56}O}^{\frac{108}{56}\bullet}\right] + 3[W_{La}^{\bullet\bullet\bullet}] + \frac{52}{56}\left[OH_{\frac{54}{56}O}^{\frac{52}{56}\bullet}\right] + p = \frac{4}{56}\left[O_{\frac{54}{56}O}^{\frac{4}{56}/}\right] + n \qquad (2.42)$$

The electrons and electron holes remain minority defects with a negligible concentration at the stoichiometric condition. The site occupancy sum in term of molar fraction will be equal to Equation 2.39.

At the stoichiometric condition the fraction of the concentration (Equation 2.40) will also include the concentrations of both donor dopants:

$$\left[O_{\frac{54}{56}O}^{\frac{4}{56}/}\right] = 27\left[V_{\frac{54}{56}O}^{\frac{108}{56}\bullet}\right] + 42[W_{La}^{\bullet\bullet\bullet}] + 14[Ce_{La}^{\bullet}] \qquad (2.43)$$

The concentration of both donor defects assumed to be constant under different oxygen partial pressure. The p_{O_2} dependencies of the different point defect concentrations for Ce-doped $La_{27}W_5O_{55.5}v_{0.5}$ are summarized in a Brower diagram:

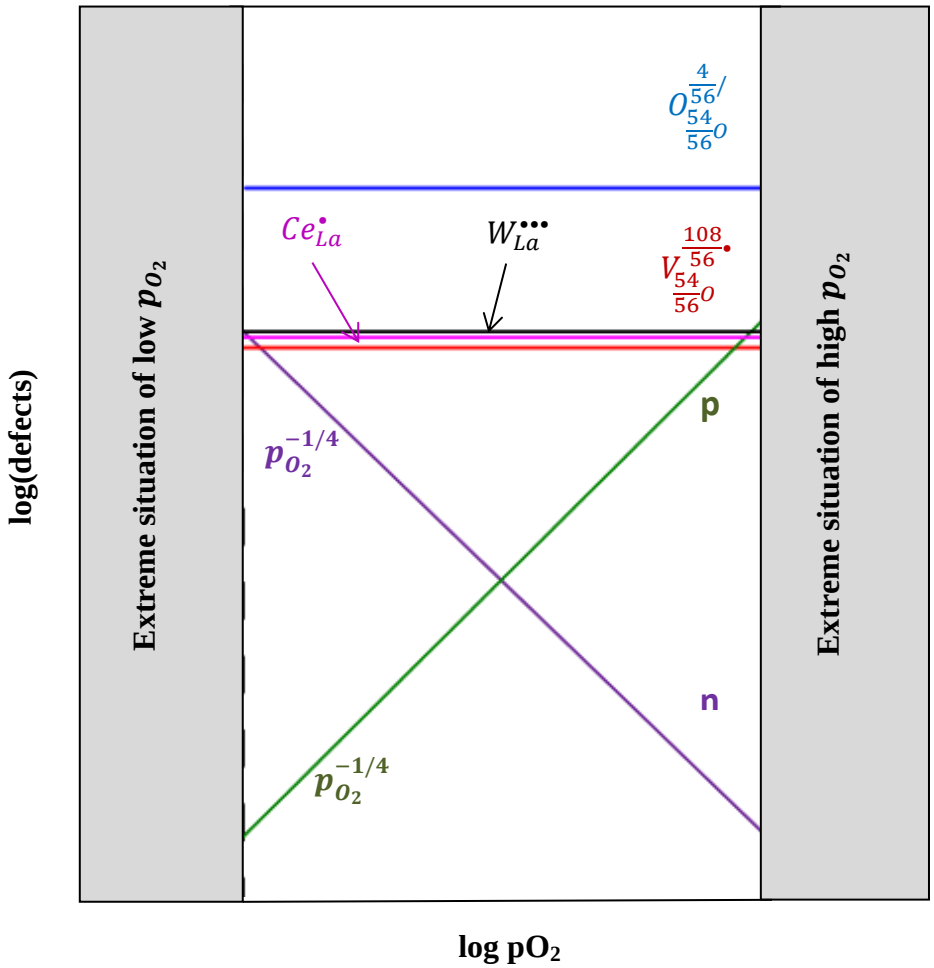

Figure 2.4. The Brower diagram of Ce-doped $La_{27}W_5O_{55.5}v_{0.5}$ shows the concentration of point defects as a function of p_{O_2}.

The concentration of both dopants assumed to be constant under the hydration process and the electroneutrality condition remains the same as for undoped LaWO (Equation 2.26).

There are no changes in the p_{H_2O} dependencies of *Ce-doped* $La_{27}W_5O_{55.5}v_{0.5}$, and the Brower diagram is similar to the diagram in Figure 2.3.

2.4 Electrical measurements

The theory of defect chemistry presented herein is based on Defects and Transport in Crystalline Solids by Per Kofstad and Truls Norby [16].

Many metal oxides, especially those with more cations exhibit mixed conductivities, which arises due to movement of charge carries. Those can be ions, electrons or holes, and their movement also depends on their mobility in a particular material.
Driving force of the diffusion of charged particles in a material is a potential gradient**:**

$$F = -z_i e \frac{d\varphi}{dx} = z_i e E \tag{2.44}$$

where φ is the electrical potential and E is the electrical field. The electrical field E acts as a driving force for the charged particles and gives rise to a flux density, j_i, for a particle *i*:

$$j_i = c_i v_i = z_i e c_i B_i E \tag{2.45}$$

where c_i in the concentration of the particles, v_i is the velocity, $z_i e$ is the particle's charge and B_i – is the particle's mobility. The net current density,i_i, can be obtained by multiplying the flux density by the particle's charge:

$$i_i = z_i e j_i = (z_i e)^2 c_i B_i E \tag{2.46}$$

The charge mobility of the particle is proportional to the particle's mobility:

$$\mu_i = z_i e_i B_i \tag{2.47}$$

Equation 2.46 can then be written:

$$i_i = z_i e c_i \mu_i E = \sigma_i E \tag{2.48}$$

The specific conductivity due to the charged particle *i* moving through the solid can therefore be defined as:

$$\sigma_i = z_i e c_i \mu_i \tag{2.49}$$

where σ_i – the specific conductivity $\left(\frac{S}{cm}\right)$, $z_i e$ – the charge of a particle i (C), c_i – the number of charged particles per unit volume $\left(\frac{N}{cm^3}\right)$ and μ_i – the mobility of a particle *i* $\left(\frac{cm^2}{Vs}\right)$.

The transport mechanism of the charge carries can vary from material to material and hence present different dependencies on temperature. In this thesis, the activated hopping mechanism is assumed to be the main for the charge carries.

The mobility of each particular charged particle in its turn depends on temperature and its enthalpy H_{mob}, which is an activation enthalpy for the transport:

$$\mu_i = \mu_0 \frac{1}{T} \exp(-\frac{\Delta H_{mob,i}}{RT}) \tag{2.50}$$

The combination of Equation 2.49 and Equation 2.50 gives the Arrhenius-type dependency of the conductivity on temperature:

$$\sigma = \frac{\sigma_0}{T} \exp\left(-\frac{E_a}{RT}\right) \tag{2.51}$$

where σ_0 in the pre-exponential factor of the conductivity, E_a – the activation energy of the conductivity. The activation energy consists of the charge mobility enthalpy, ΔH_{mob}, and the formation enthalpy, ΔH_d: $E_a = \Delta H_{mob} + \Delta H_d$.

By taking the logarithm of Equation 2.51, one can find the value for the activation energy:

$$\ln(\sigma T) = \ln(\sigma_0) - \frac{E_a}{RT} \tag{2.52}$$

The total conductivity σ_{tot} of a material is the sum of contribution of different charged species as cation, anion, electron and holes:

$$\sigma_{tot} = \sum \sigma_i = \sigma_{cations} + \sigma_{anions} + \sigma_{electrons} + \sigma_{holes} \tag{2.53}$$

The conductivities of cations and anions, $\sigma_{cations}$ and σ_{anions}, represent the ionic conductivity (Equation 2.54), while the conductivities of electrons and electron holes $\sigma_{electrons}$ and $\sigma_{holes,}$ are summed together as an electronic conductivity (Equation 2.55):

$$\sigma_{ionic} = \sigma_{cations} + \sigma_{anions} \tag{2.54}$$

$$\sigma_{electronic} = \sigma_{electrons} + \sigma_{holes} \tag{2.55}$$

The conductivity of a charge carrier (Equation 2.49) can also be related to the diffusion coefficient through the Nernst-Einstein relation:

$$\sigma_i = \frac{(z_i e)^2 c_i D_i}{k_B T} \tag{2.56}$$

where D_i is the self-diffusion coefficient of the defect species i and k_B is the Boltzmann constant. The self-diffusion coefficient D_i is proportional to the frequency of the sufficient energetic jump:

$$\omega = \nu \exp\left(\frac{\Delta S_m}{R}\right) \exp\left(-\frac{\Delta H_m}{RT}\right) \tag{2.57}$$

where ΔS_m is the entropy of mobility, H_m is the enthalpy of mobility, and ν is the vibration frequency. The vibration frequency can be approximated to:

$$\nu = \frac{\alpha}{\mathrm{a}} \sqrt{\frac{\Delta H_m}{m_{D/H}}} \tag{2.58}$$

where a is the lattice parameter, α is the mechanism-dependent factor, ΔH_m is the enthalpy of migration/hopping, m_D is the deuterium mass (2.0141 u), and m_H is the hydrogen mass (1.00794 u).

In proton conducting oxides, proton conductivity in deuterium-containing atmosphere (D_2/D_2O) is lower than that in hydrogen-containing atmosphere (H_2/H_2O). This effect is called isotope effect and related to the difference in mass between hydrogen (H) and deuterium (D).

As seen from Equation 2.58, the difference in masses in the hydrogen/deuterium atoms will change the vibration frequency, and thus, affect the protonic conductivity. The relationship between the protonic conductivity of hydrogen ion, $\sigma_{OH_O^\bullet}$, and the protonic conductivity of deuterium ion, $\sigma_{OD_O^\bullet}$:

$$\sigma_{OH_O^\bullet} = \sqrt{2}\sigma_{OD_O^\bullet} \tag{2.59}$$

2.5 Impedance spectroscopy

Impedance spectroscopy is an important technique to characterize the electrical properties of ceramic materials. This technique makes it possible to distinguish between the contribution from a grain and a grain boundary, as well as en electrode of en polycrystalline material.

2.5.1 Alternating current and Impedance

Impedance spectroscopy is based on alternating current (AC), where both the voltage (V) and current (I) vary as a sinusoidal function of time.

$$U = U_0 sin\omega t \tag{2.60}$$

$$I = I_0 \sin(\omega t + \theta) \tag{2.61}$$

where U_0 and I_0 are respectively voltage and current amplitudes, ω is an angular frequency, which depends on frequency f: ω = 2πf. As seen from Equation 2.61, the sinusoidal current is described with the same characteristic frequency at the voltage, but it is phase-shifted by an angle θ relative to the voltage. This happens due to capacitive and inductive circuit elements.

The Ohm's law introduces a constant between the current and the voltage, which is called resistance, $R = \frac{V}{I}$. For alternating currents, this constant is called impedance Z and is used to describe the ratio between voltage and current as well as the phase shift between them.

The alternating current I has two components: one that is in the phase with the voltage V and another one is $\frac{\pi}{2}$ out of phase of the voltage. As the result, the alternating resistance, which is called impedance, splits into real and imaginary components. The real part of the impedance is called resistance, R and the imaginary part – reactance, X:

$$Z = Re\, Z + i\, Im\, Z = R + iX \ (i=\sqrt{-1}) \tag{2.62}$$

The real part (R) reflects the real transport of charge carries, while the imaginary part ($R_L \ and \ R_C$) reflects the charge carries that are not really transported thought the

circuit, but stored in the capacitor or not really impeded. Those, the total impedance Z can be graphically represented as a vector in the 2-dimensional real – imaginary space:

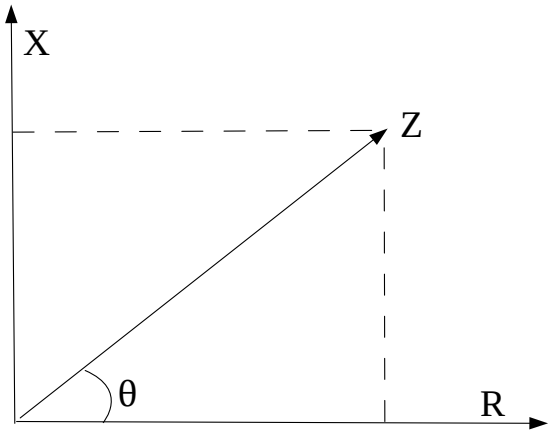

Figure 2.5. Representation of complex impedance vector Z.

The inverse of impedance is admittance Y, which measures how easily a circuit allows current to flow:

$$Y = 1/Z \tag{2.63}$$

Admittance is also a complex number, where its real part is called conductance, G, and the imaginary part is called susceptance, B. Both parts measures in Siemens, S

$$Y = Re\,Y + i\,Im\,Y = G + iB \tag{2.64}$$

The relation between impedance Z, conductance G and susceptance B is given by:

$$Z = \frac{1}{Y} = \frac{G}{G^2 + B^2} - \frac{iB}{G^2 + B^2} \tag{2.65}$$

The relation between admittance Y, resistance R and reactance X is given by:

$$Y = \frac{1}{Z} = \frac{R}{R^2 + X^2} - \frac{iX}{R^2 + X^2} \tag{2.66}$$

2.5.2 Passive electrical circuit elements

Components of en polycrystalline material can be presented as grains and grain boundaries. Under the applied alternating current, they can be charged and show resistive, inductive or capacitive properties. Therefore polycrystalline material can be presented as an electrical circuit with both passive and active elements. There are three passive electrical circuit elements that are used in order to describe and understand electrical circuits and how they depend on frequency.

Resistor

Resistor is an element of en electrical circuit with long-range transport of charge carries that can give rise to resistance R and conductance G = 1/R. In an ideal resistor, instant voltage gives rise instantly to current and vice versa, so there is no phase shift, and $\theta = 0$. The relationship between voltage and current is given by Ohm's law:

$$R = \frac{U_0 sin\omega t}{I_0 \sin(\omega t)} = \frac{U_0}{I_0} \tag{2.67}$$

Capacitor

Capacitor basically consists of two parallel conducting plates, separated by a dielectric material or vacuum. When the voltage is applied, the charge flows towards the plates, so that they are oppositely charged. The capacitance, the ability of a capacitor to store an electrical charge, depends on the distance d between the two plates, its area A and a type of dielectric:

$$C = \varepsilon_0 \varepsilon_r \frac{A}{d} \tag{2.68}$$

where ε_0 is the vacuum permittivity and ε_r is the relative permittivity of the medium or relative permittivity. When an alternating voltage is applied over the capacitor, an alternating current with a phase shift $\frac{\pi}{2}$ will be produced. The capacitive resistance will therefore comprise only an imaginary contribution and depends on angular frequency and capacitance:

$$R_C = \frac{1}{\omega C} \tag{2.69}$$

Inductor

Inductor consists of a conducting coil with no resistance. When an alternating voltage is applied over the inductor, the magnetic field is set up, which in turn induces the alternating current with a phase shift $\frac{\pi}{2}$ over the inductor. The inductive resistance of this electrical element also consists of only an imaginary contribution and is proportional to frequency and inductance:

$$R_L = \omega L \tag{2.70}$$

where L is an inductance, the property of inductor to induce the AC voltage.

2.5.3 Impedance sweep

Impedance spectroscopy implies measurements of the impedance of a material over a range of frequencies. This measurement called an impedance sweep and it can be plotted in a Nyquist diagram (Figure 2.6). This diagram presents the impedance vector Z (Figure 2.5) as a function of the imaginary impedance versus the real impedance. For a polycrystalline material the sweep is composed by one to three semicircles from high to low frequency, which can be described using different combinations of the passive circuit elements mentioned previously. Each semicircle can correspond to a contribution from the grain interiors, the grain boundaries and the electrodes.

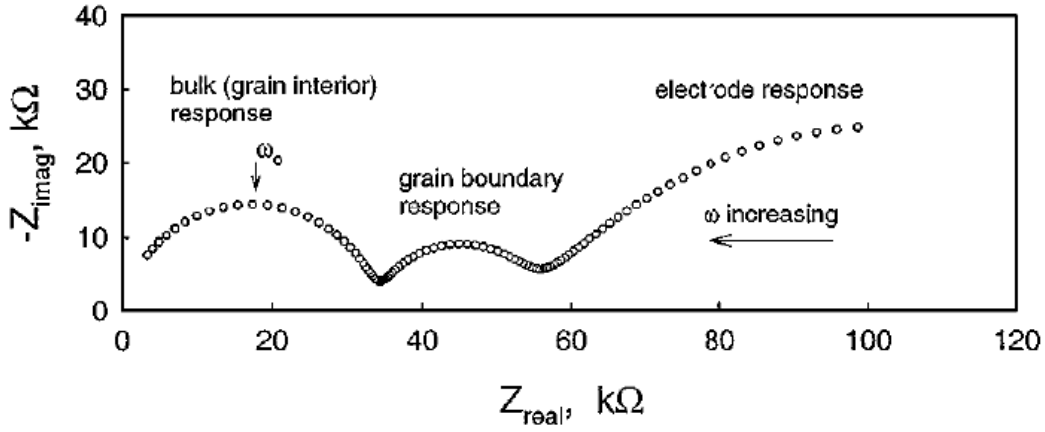

Figure 2.6. The Nyquist representation of a typical polycrystalline material [21].

The first semicircle at high frequency associated with a contribution of the grains interior or the bulk, while the second at lower frequency is a contribution of the grain boundaries. Both grains and grain boundaries can contribute with different size of the semicircle, which depends on its resistance. The resistance of grains and grain boundaries depends on the temperature and some semicircles can appear or vanish when the temperature changes.

Ideally each of the contributions is represented as an arc and the most common way of describing these contributions is a set of resistor R and capacitor C connected in parallel to each other. This combination expresses as (RC) and corresponds to a perfect semicircle, the frequency of the maximum point of which is called the characteristic frequency, ω_0, and gives by:

$$\omega_0 = \frac{1}{RC} = \frac{A}{d\rho}\frac{d}{\varepsilon_0\varepsilon_r A} = \frac{\sigma}{\varepsilon_0\varepsilon_r} \tag{2.71}$$

where A is the area of the cross-section, d is a diameter of the sample, ρ is a resistivity ($\rho = 1/\sigma$) and σ is a conductivity. The characteristic frequency, as shown in equation 2.71 is independent of the geometry of the sample, but dependent on the conductivity, which increase with temperature. Therefore the characteristic frequency increases with increasing conductivity.

At the impedance measurements the bulk resistance is represented as an average resistance of all the grains in material, and the grain boundary resistance, respectively, as an average of all the grain boundaries. If all the grains and grain boundaries were identical, they then could be presented at the Nyquist plot as two ideal semicircles, each of them as (RC) element. However in the real polycrystalline material, the grain and grain boundaries are different in size and orientation, which result in different impedances. The total impedance will be therefore reflecting this difference in parameters, and result in depression of the ideal semicircles. In order to describe the depressed semicircles, a constant phase element (CPE) is used. This element is assigned with a symbol Q and has admittance which is given by:

$$Y = Y_0(i\omega)^n = Y_0[\omega^n \cos\left(\frac{\pi n}{2}\right) + i\omega \sin\left(\frac{\pi n}{2}\right)] \tag{2.72}$$

where *n* is a constant that can vary from -1 to 1. The CPE element will represent a capacitor if n = 1, a resistor if n = 0, and an inductor if n = - 1. Grains and grain boundaries can be therefore described by the constant phase element Q, parallel with a resistor R. For such a circuit element, the characteristic frequency will be given by:

$$\omega_0 = \frac{1}{(RY_0)^{\frac{1}{n}}} \tag{2.73}$$

The real capacitance of (RQ) sub-circuit is then given by:

$$\mathrm{C} = Y_0^{\frac{1}{n}} R^{\frac{1-n}{n}} \tag{2.74}$$

Table 2.4 shows the standard capacitance for different elements, contributed to the impedance sweep.

Table 2.4. The standard capacitances for the different elements, which can contribute to the impedance sweep.

Element	**Bulk**	**Grain boundary**	**Electrode**
	C_b, F	C_{gb}, F	C_{elect}, F
Capacitance	~$10^{-12} - 10^{-11}$	$10^{-10} - 10^{-9}$	$10^{-6} - 10^{-4}$

2.5.4 Brick Layer Model

The theory behind the Brick Layer model is based on the article "Haile, S.M., D.L. West, and J. Campbell, The role of microstructure and processing on the proton conducting properties of gadolinium-doped barium cerate. Journal of materials research, 1998. ***13****(06): p. 1576-1595"[22].*

The Brick Layer model is a model that often can be used to describe the electrical properties of a polycrystalline material. Microstructure can be considered as a matrix of grains at a cubic form, which are separated from each other by the grain boundaries. The last mentioned are both parallel and perpendicular to the direction of the applied

field. Figure a shows a graphic presentation of this model, where L – the length of the sample, *A* – the cross section of the sample, *G* – the length of the grain and *g* – the thickness of the grain boundary.

Following by the model, the equivalent circuit of the elements is described by several (RQ) elements, as shown in Figure 2.7(b). The two parallel (RQ) elements correspond to the parallel grain boundaries and bulks. The second (RQ) element, which is in series to the last mentioned group, presents the grain boundaries which are perpendicular to the first mentioned. The parallel (($R_{bulk}Q$)($R_{gb,paralell}$Q)) can be simplified to one element (RQ) as shown in Figure 2.7(c).

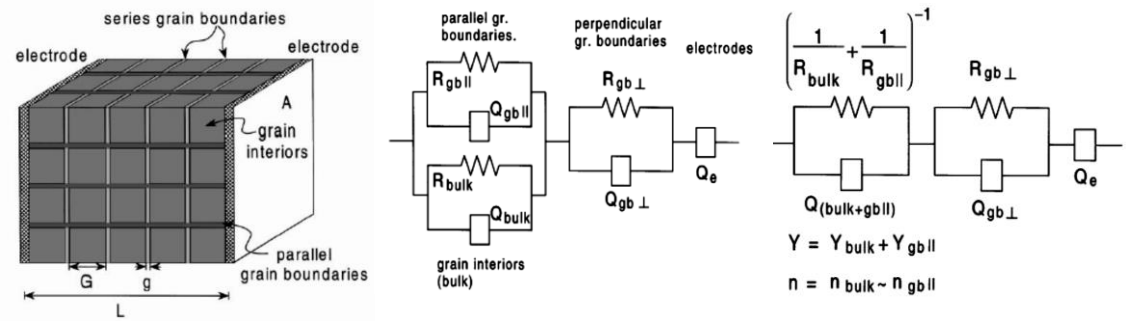

(a) (b) (c)

Figure 2.7. "Brick Layer" model of a polycristalline material (a); a complete equivalent circuit model where each component is included in the circuit (b); simplified equivalend circuit model where components in parallel have been lumped together (c) [22].

With Brick Layer model it is possible to determine a specific conductivity for the bulk, σ_b, and grain boundary, σ_{gb}: $\sigma_i = \frac{L}{AR_i}$, where R_i is the deconvoluted resistance (calculated from the sweep measurements).

Therefore, the conductivity of sum of bulk and parallel grain boundaries, σ_1, and the conductivity of perpendicular grain boundaries, σ_2, can be expressed as:

$$\sigma_1 = \frac{2g}{G}\sigma_{gb} + \sigma_{bulk} = \frac{1}{R_1} \tag{2.75}$$

$$\sigma_2 = \frac{G}{g}\sigma_{gb} = \frac{1}{R_2} \tag{2.76}$$

The ratio between σ_1 and σ_2:

$$\frac{\sigma_1}{\sigma_2} = \frac{R_2}{R_1} = 2\left(\frac{g}{G}\right)^2 + \left(\frac{g}{G}\right)\frac{\sigma_{bulk}}{\sigma_{bg}} \quad (2.77)$$

The Brick Layer model describes three different cases based on the relation between the grains and grain boundaries.

Case 1: $\sigma_{bulk} > \sigma_{gb}$, the specific conductivity of the bulk is greater than the specific conductivity of the grain boundary, and the thickness of the grain boundary is much smaller than it is at the bulk, g < G. Then the equations 2.75 becomes: $\sigma_1 = \sigma_{bulk}$, while the conductivity of grain boundary will remain the same. The contribution of these conductivities will be separated in two semicircles in the Nyquist plot. The first semicircle may be associated with bulk and the second semicircle may be associated with perpendicular grain boundaries. The ratio between the conductivities described by equation 2.77 becomes: $\frac{\sigma_{bulk}}{\sigma_{gb}} = \frac{R_2}{R_1} = \frac{g}{G}$.

Case 2: $\sigma_{bulk} < \sigma_{gb}$, the specific conductivity of the grain boundary is greater than that of the bulk, and the ratio g/G is not greater than 10^{-2}. In this case no simplification to Equation 2.75 can be made. In practice, only one semicircle will be observed in the Nyquist plot.

If $\sigma_{gb}/\sigma_{bulk} >>$ ½ (G/g), the semicircle will represent the parallel grain boundaries. If $\sigma_{gb}/\sigma_{bulk} \approx$ ½ (G/g), the semicircle will represent both parallel grain boundaries and grain. If ½ (G/g) $\sigma_{bulk} > \sigma_{gb} > \sigma_{bulk}$, the semicircle will mostly represent bulk.

Case 3: $\sigma_{bulk} \approx \sigma_{gb}$, the specific conductivity of the bulk and the grain boundary are approximately equal. This case is quite similar to case 1, when $\sigma_{bulk} > \sigma_{gb}$.

3 Literature

3.1 Crystal structure

3.1.1 Crystal structure and unit cell

LWO has a cubic fcc structure and $F\bar{4}3m$ space group. Both lanthanum and tungsten sits in octahedrons, surrounded by eight oxygen sites. The tungsten sites are fully occupied, but oxygen sites are partially filled. In the case of lanthanum, there are two types of octahedrons: La1 - eight fully occupied sites and La2 - half-occupied ones [17]. Coordination of La2 was reported to be 6.6 [20]. Since oxygen sites are not fully occupied, a formation of structural oxygen vacancies occur. After investigating this material by XRD and neutron diffraction, it was concluded that the exact stoichiometry of LWO is $La_{28-x}W_{4+x}O_{54+1,5x}v_{2-1,5x,}$ where v – represents oxygen vacancies [20]. The structure of LWO is closely related to the cubic fluorite structure of $Y_7ReO_{14-\delta}$ which is a superstructure of the CaF_2 structure [23]. The intrinsic formation of oxygen vacancies makes the structure inherently disordered, which in turn changes the standard notation of the defect chemistry (see subsection 2.2). In addition to the inherent oxygen vacancies, this material also exhibits one more interesting property determined by DFT analysis: W substitution of La on the La2 sites (Figure 3.1(a)). The substitution of La2 by W acts as a donor, and creates a positive defect $W_{La}^{\bullet\bullet\bullet}$, the concentration of which determines by the value x at the formula unit.

No intrinsic donor defect (x = 0) means 2 vacancies and 54 oxygens on oxygen sites. This gives the nominal formula $La_{28}W_4O_{54}v_{2,}$ which is the start point for defect notation (see subsection 2.2.1). The presence of the effective positive charge caused by the intrinsic substitution (x > 0) is compensated by an increased oxygen content and hence decreased vacancy amount. The structure $La_{28-x}W_{4+x}O_{54+1,5x}v_{2-1,5x}$ is more stable with lower oxygen vacancy concentration, i.e. lower La/W ratio, as the compound then becomes more disordered and hence less stable. This is why it is impossible to synthesize LWO7 ($La_{27}W_4O_{55}v_2$) [20].

The lattice parameter depends on the composition and varies from 11.17 to 11.19 Å [17].

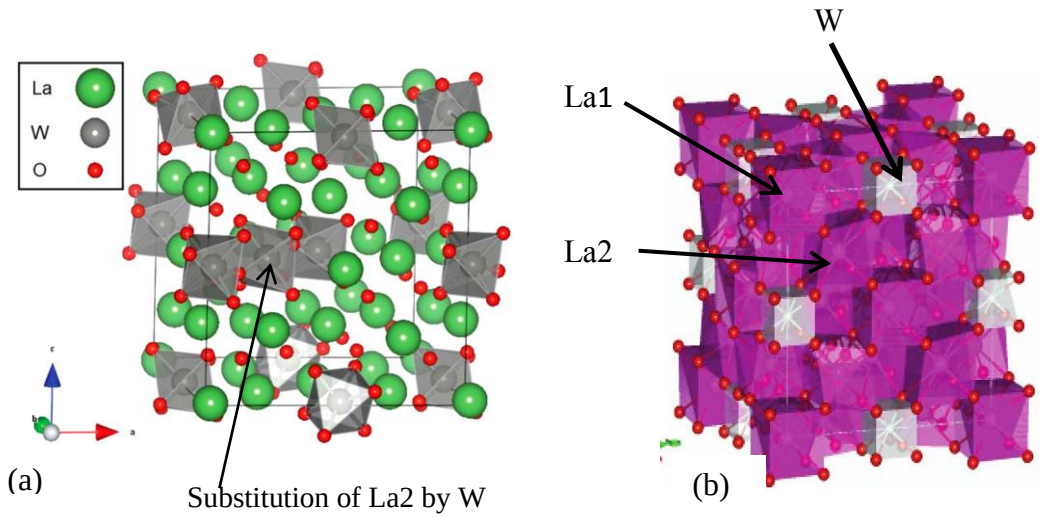

Figure 3.1. Relaxed structure of a $La_{28-x}W_{4+x}O_{54+1,5x}v_{2-1,5x}$ *unit cell with one La2 substitution[20] (a), and positions of La1, La2 and W atoms in the structure [17](b).*

3.1.2 Phase formation

There are several studies of the structure of $La28_{-x}W_{4+x}O_{54+1,5x}v_{2-\ 1,5x}$ with different x values. This ratio between La and W is the main factor which defines both lattice parameters and if the material is of single phase. There are three regions that can be distinguished based on this ratio, as can be seen at Figure 3.2(a). A region II with La/W ratio between 5.3 and 5.7 shows a single phase domain with linear dependency of the lattice parameters. A region III with high La/W ratio shows a segregation of La_2O_3 as a secondary phase. Even though a small lanthanum deficiency gives stability of the compound (region II), smaller ratio of La/W (region I) with quite high La deficiency also gives a secondary phase, which is tungstate rich [17]. The XRD patterns with formation of secondary phase as a function of the nominal La/W ratio are presented in Figure 3.2(b-c).

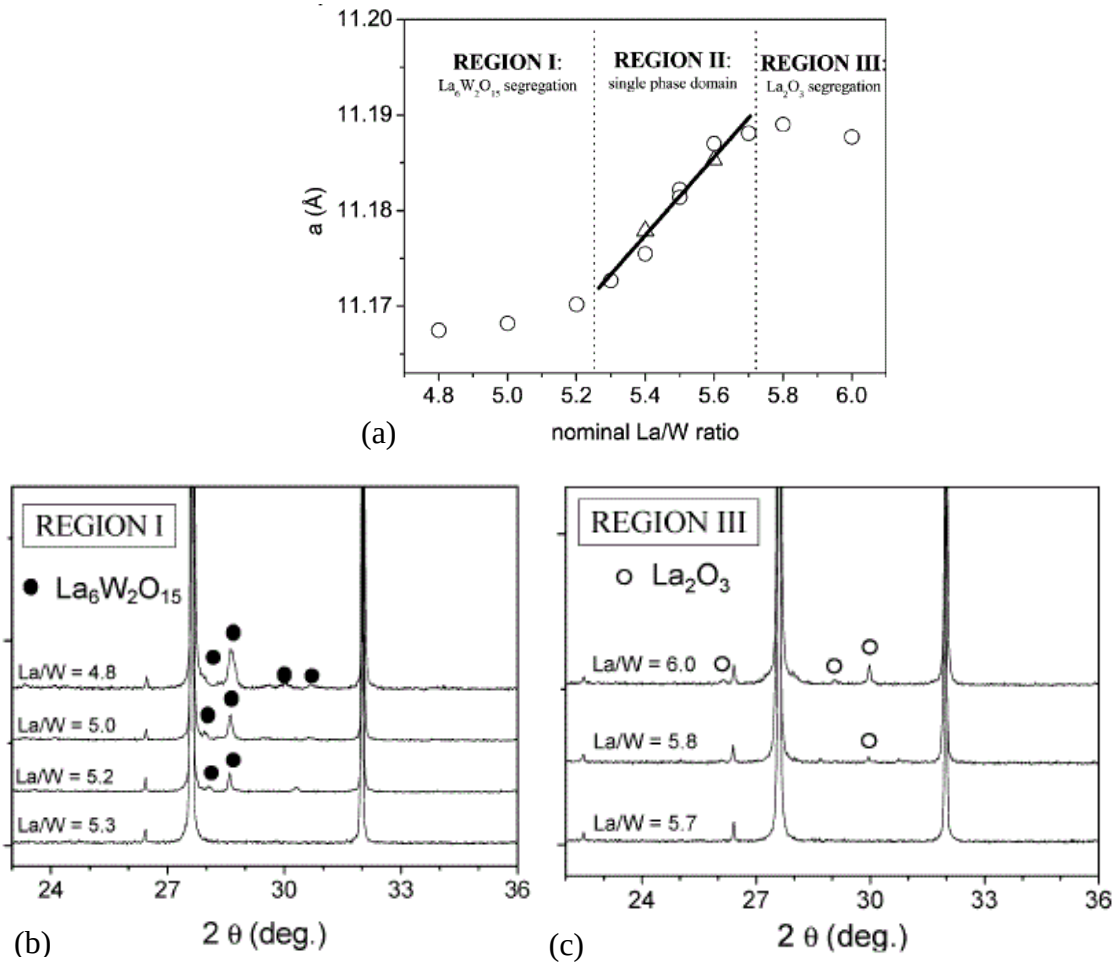

Figure 3.2. Variation of the lattice parameters as a function of the nominal La/W ratio (a), XRD patterns displaying a secondary phase appearance for region I (b) and region III (c) for different La/W ratio [17].

The formation of secondary phases is also detected for LWO from region II under calcination. The amount of secondary phase decreases with increasing the firing temperature. A higher lanthanum content in the structure need a higher firing temperature to obtain complete formation reaction [17]. This feature was used to choose the final calcination temperature for LWO54 in this master thesis.

The influence of the tungsten rich secondary phase in the electrical conductivity properties of LWO – based ceramics was studied by Ivanova et al [24]. $La_6W_2O_{12}$ phase undergoes thermal expansion, which leads to cracked microstructure. The presence of this compound as a secondary phase in LWO has a negative effect on the electrical properties of LWO. $La_6W_2O_{12}$ results in decreasing the electrical conductivity of LWO in several orders of magnitude and slowing down the hydration of LWO due to faster hydration of this phase [24].

As seen in the Figure 3.3, the La_2O_3-WO_3 phase diagram contains a number of compounds. The crystal structure and transport properties of La_2WO_6, $La_6W_2O_{15}$, $La_{14}W_8O_{45}$/$La_{18}W_{10}O_{57}$ were studied [24-26].

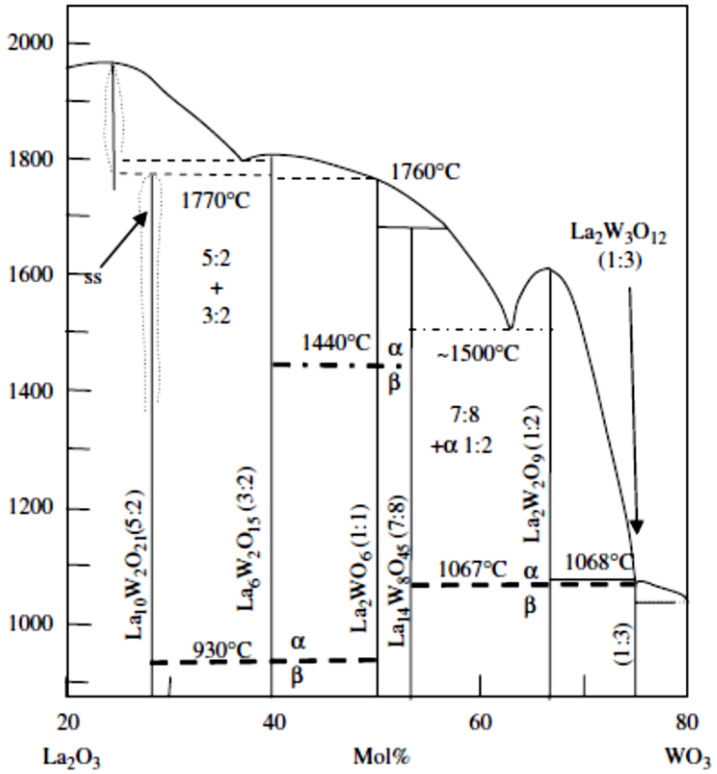

Figure 3.3. Phase equilibrium diagram for the system La_2O_3-WO_3[25].

3.2 Hydration of LWO

Hydration of LWO was studied for LWO with ratio 5.4, 5.3 and 5.6 by means of thermogravimetric analysis [17], [27]. The thorough investigation of the hydration properties of LWO53 and LWO56 was published by Hancke at al [27]. The thermogravimetric curves (Figure 3.3 (a)) show a typical behavior of a proton conducting material. The weight increase under wet reducing and oxidizing atmospheres did not show any difference, which emphasizes that the uptake is independent in oxygen partial pressure and corresponds to the formation of only protonic defects. No weight uptake was detected at dry oxidizing conditions. The proton formation for this material is independent of the oxygen partial pressure. This was also reported at Haugsrud et al [11]. LWO compounds with different nominal La/W ratio exhibit different level of hydration. LWO53 hydrates all the vacancies (0.38 per unit cell), while LWO56 hydrates only 66 % of the theoretical amount of vacancies (0.48 out 0.73 vacancies per unit cell). The reason for this is the precipitation of La_2O_3 particles which decrease the amount of free oxygen vacancies available for hydration. The standard enthalpy and entropy of hydration for LWO were estimated to be -90kJ/mol and -115 J/molK respectively [27].

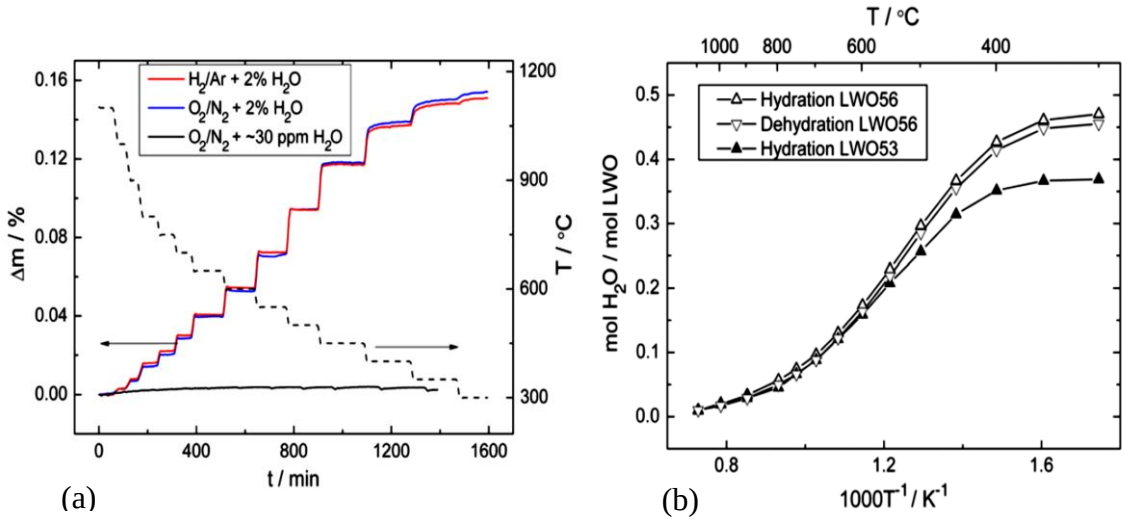

Figure 3.4. The mass change of LWO56 under wet reducing and wet and dry oxidizing conditions [27] (a); the water concentration of LWO53 and LWO56 as a function of reciprocal temperature under wet oxidizing condition [27] (b).

3.3 Electrical properties of LWO

3.3.1 Conductivity of LWO as a function of temperature

The first investigation of electrical properties of LWO was published by M. Yoshimura et al [18]. The total electrical conductivities of the solid solutions in the system CeO_2 – LWO were studied. LWO was defined as an electronic conductor at high temperatures and an ionic conductor at temperatures below 780 °C. This was also proved by different activation energies at low and high temperatures [18]. Figure 3.4 shows a conductivity dependency as a function of temperature for the range of CeO_2 – LWO systems.

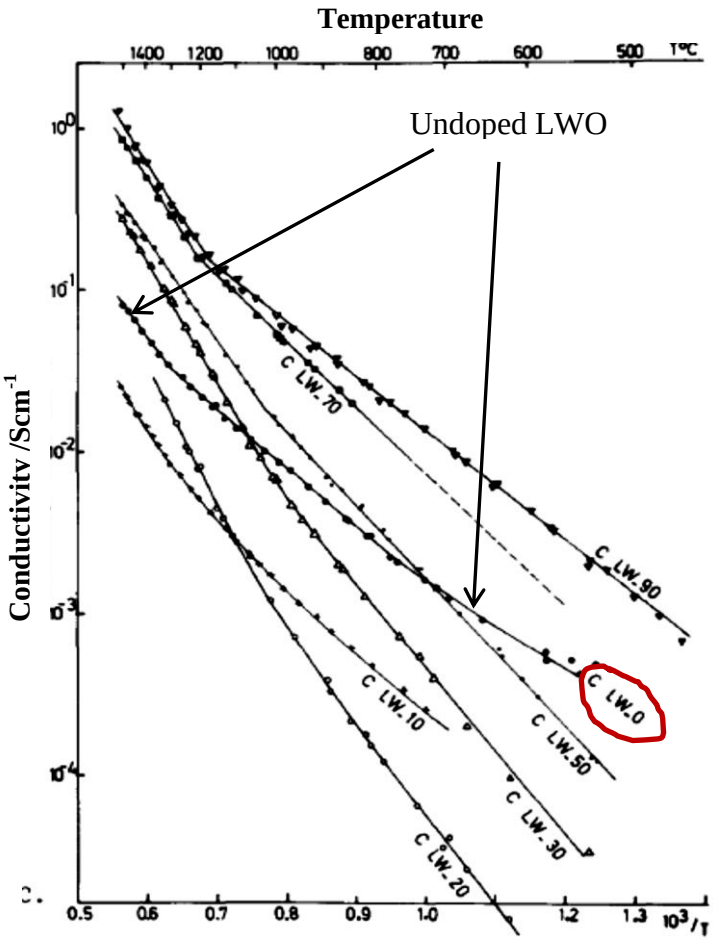

Figure 3.5 Electrical conductivity of solid solutions in the system CeO_2 – LWO [18].

Later studies of LWO were published by T. Shimura et al. [12]. The contribution of protons to the electrical conduction in LWO58 and $LaBO_3$ (lanthanum borate) were investigated in air, wet H_2 and wet D_2. An H/D isotope effect emphasized a proton contribution to the conductivity in LWO58. For the high temperature region a higher conductivity in wet hydrogen was explained by an n-type electronic contribution. Figure 3.5 presents these studies.

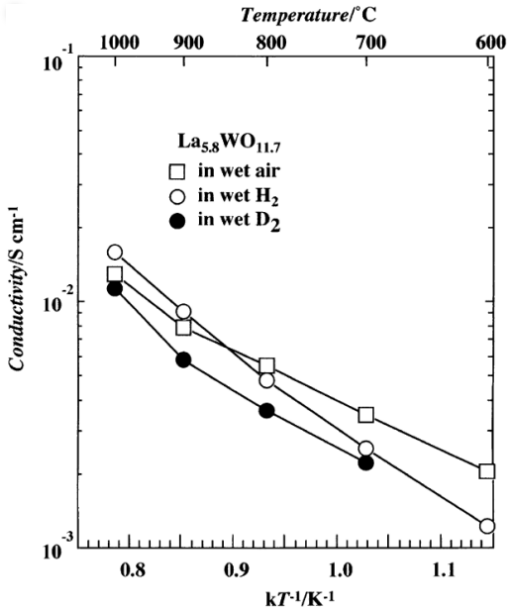

Figure 3.6. Temperature dependence of the electrical conductivity of LWO in wet air, wet H_2 and D_2 [12].

The dominating proton conductivity was proved by the isotope effect below 800 °C (Figure 3.7). The highest proton conductivity was detected at ~750 °C with a value of 3×10^{-3} S/cm in wet H_2 [11].

The protonic conductivity of LnWO – related materials (La=La, Nd, Er) upon acceptor doping was also studied. Figure 3.8 shows that the protonic conductivity decreases with decreasing radius of Ln^{3+}, and it is replaced by different species at high temperatures: electrons for ErWO and oxygen vacancies for LaWO and NbWO [9].

Hydration enthalpies for other rare-earth containing proton conductors become increasingly negative with decreasing radii of the rare – earth cations: $\Delta H^0_{hydr}(Er) < \Delta H^0_{hydr}(Nd) < \Delta H^0_{hydr}(La)$ [9].

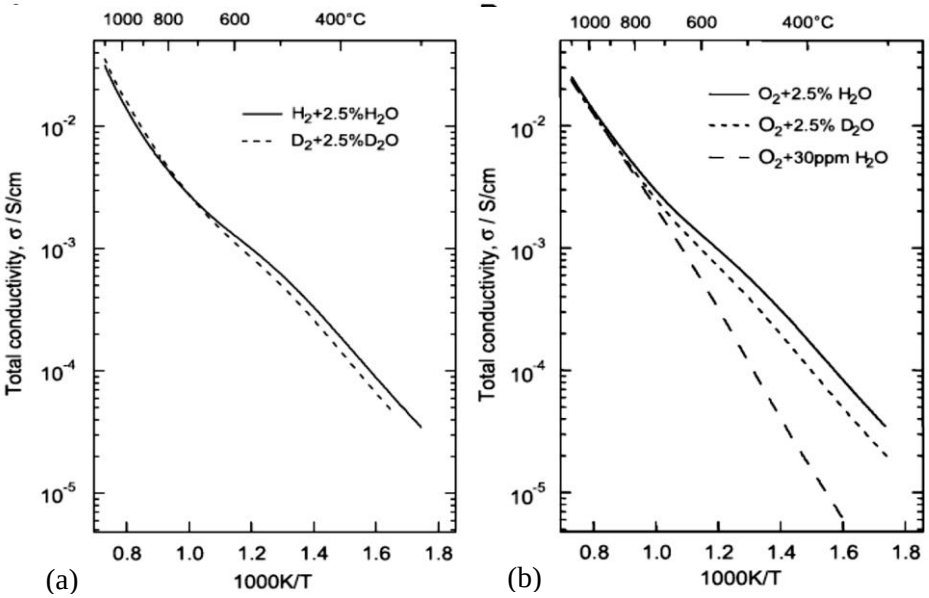

Figure 3.7. The total conductivity as a function of temperature for LWO6 under H_2 +2.5% H_2O and D_2 + 2.5% D_2O (a) and O_2 + 2.5% H_2O, O_2 + 2.5% D_2O and dry O_2 (b) [11].

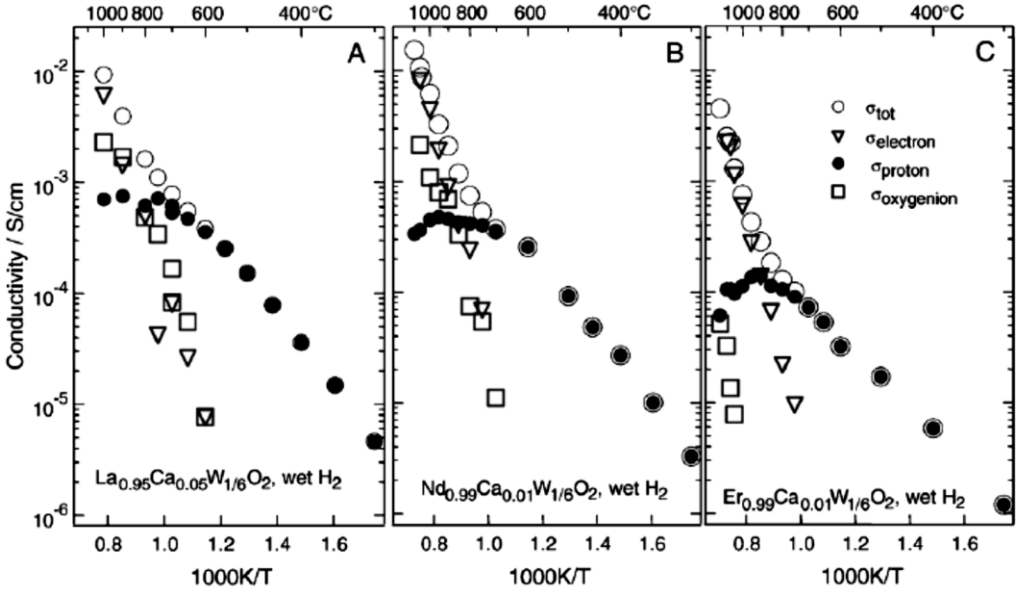

Figure 3.8. The partial conductivities as a function of temperature for Ca-doped LWO6, NdWO6 and ErWO6 under H_2+2.5%H_2O atmospheres [9].

3.3.2 Conductivity of LWO as a function of p_{O_2}

The total conductivity was studied as a function of oxygen partial pressure and results are published in several sources [9, 11, 12, 15]. The plateau in the conductivity at intermediate p_{O_2} is observed at all the temperatures and it indicates the ionic conductivity [15]. There is a small increase in the conductivities for LWO58 and LWO6 under sufficiently reducing and oxidizing conditions (Figure 3.8). This indicates a small contribution of n- and p-type electronic conductivity in these regions.

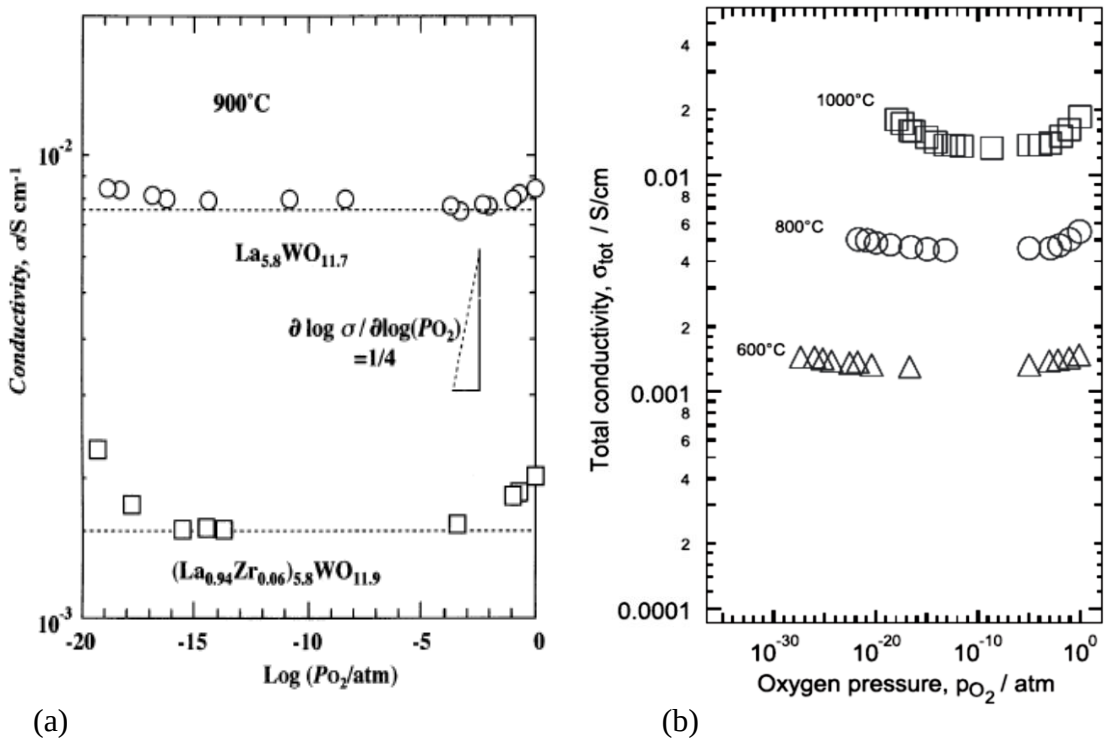

Figure 3.9. The total conductivity as a function of the oxygen partial pressure at different temperatures for LaWO58 [12] and LaWO6 [11].

However, with decreasing the nominal ratio between La and W, and hence increasing W concentration, the plateau in the conductivity at intermediate p_{O_2} decreases. This was be explained by decreasing the amount of vacancies in the structure and hence, decreasing the ionic contribution (protons and oxygen ions). As a result, the contribution of the electronic n-type conductivity becomes predominant. This effect can be seen as a steeper p_{O_2} dependency under reducing conditions, which is more

prominent at the highest temperatures (Figure 3.8). At temperatures below 800 °C the ionic conductivity predominates the total conductivity. As the temperature increases, the electronic charge carries become more mobile and start to dominate under most reducing and oxidizing conditions. The effect of p_{O_2} on the conductivity behavior at different temperatures for different compositions of LWO is presented in Figure 3.9. LWO is thus behaves as mixed ionic and electronic conductor.

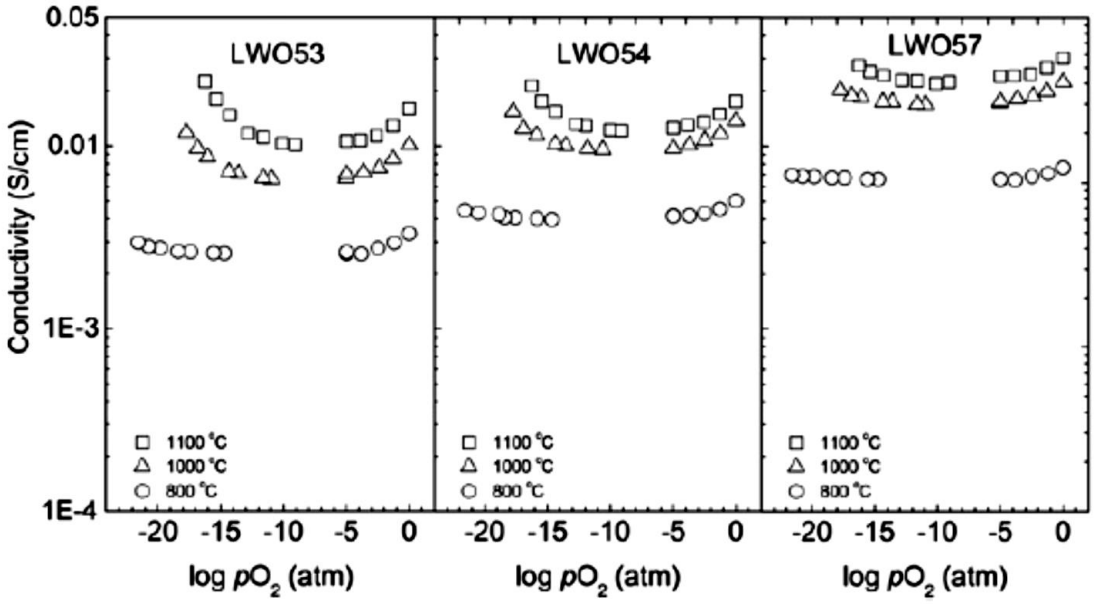

Figure 3.10. The total conductivity as a function of oxygen partial pressure at different temperatures with varying La/W ratio [15].

3.4 Electrical properties of doped LWO

Youshimura et al. [18] concluded that the ionic contribution in CeO_2 – LWO systems prevails at low temperatures, while the electronic conductivity is significant at higher temperatures, but the protonic contribution was not studied. The increase in the total conductivity in spite of the decrease in vacancy concentration in Ce-doped La_6WO_{12} was then reported [18].

Later Shimura et al. [12] investigated effects of substitution of Zr (3 mol%) and Nd (3 mol%) of the La site and observed that the ionic conductivity decreased with Zr present, while the change in conductivity upon Nd substitution was small (Figure

3.11(a)). The decrease in the total conductivity upon doping was also observed by Haugsrud et al. [9, 11], who studied the different compositions of LWO6 with 0.5 % and 5 % Ca-doped. Figure 3.11 shows the total conductivity as a function of temperature of donor doped LWO58 and acceptor doped LWO6.

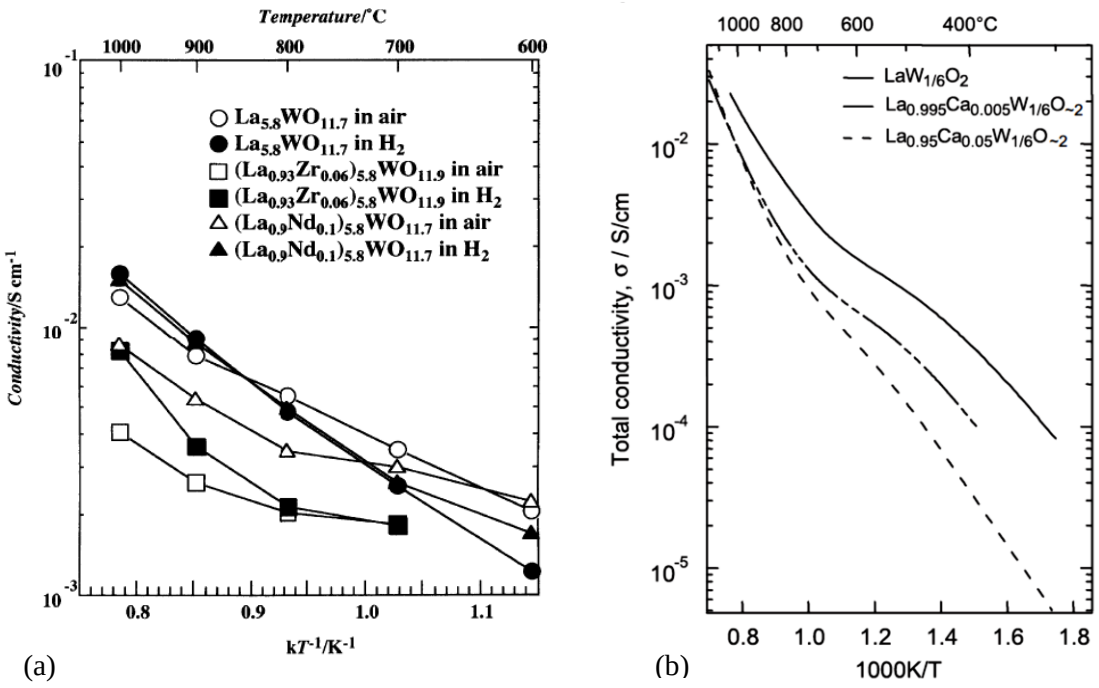

Figure 3.11. The total conductivity as a function of temperature for Zr and Nd doped LWO58 under H_2+2.5%H_2O and air +2.5%H_2O[12](a); and 0.5% and 5% Ca doped LWO6 under H_2 +2.5%H_2O [11](b).

The donor doping of LWO58 with Zr did not prove the expected increasing in the ionic conductivity reported by Yoshimura. A possible reason for this could be decrease of the lattice parameter upon donor substitution (from 11.17 Å for LWO58 to 11.14 Å for Zr-doped LWO58), comparing to the best proton conductor $BaCeO_3$, which has the largest lattice parameter among proton – conducting perovskites [12]. Haugsrud et al [9] reported two reasons of decrease in the total conductivity under acceptor doping: a possible decrease the number of protons dissolved and/or reduction the mobility of protons.

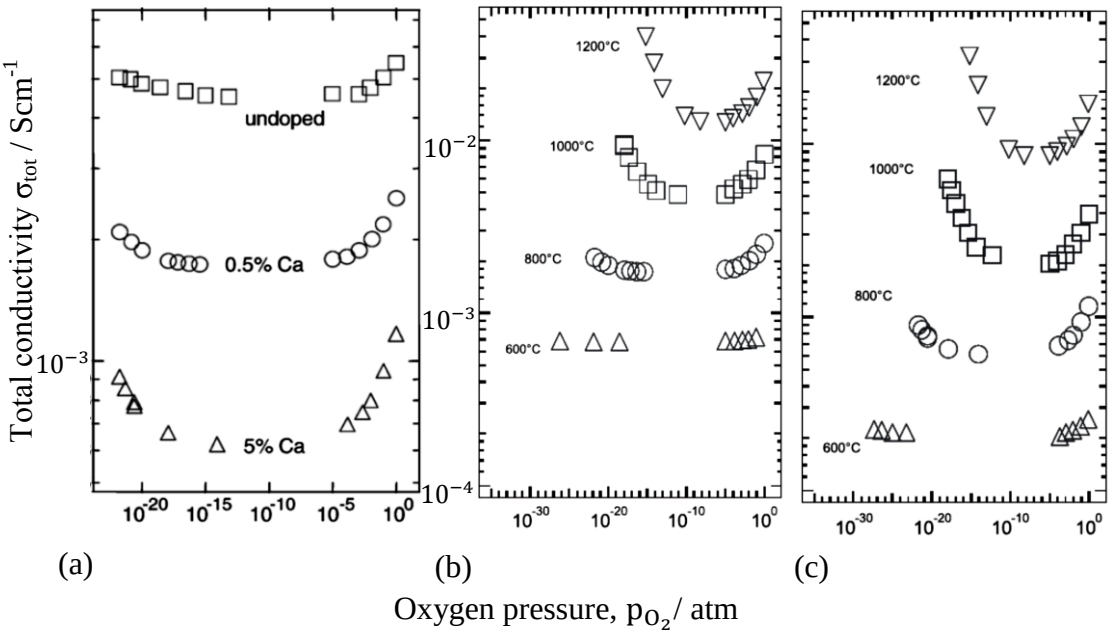

Figure 3.12. The total conductivity as a function of oxygen partial pressure for 0.5 % and 5% Ca - doped LWO6 at 800 °C [9] (a); for 0.5 % Ca-doped LWO6 (b) and 5 % Ca-doped LWO6 (c) at different temperatures from 600 to 1200 °C [11].

The enthalpy of protonic mobility increased upon acceptor doping [11]. This was explained by trapping of protons by acceptors, which caused the lower proton mobility

Figure 3.12 shows the decrease in the ionic conductivity as compared to the electronic conductivity upon acceptor doping of LWO6.

The increased conductivity with increased water vapor pressure at temperatures below 800 °C (Figure 3.12) reflects the hydration process at LWO. The conductivity increases with increasing amount of water vapor. However the conductivity decreases with increasing lever of acceptor doping. This effect can be also explained by the trapping model discussed above. As trapping is relative only to decrease in the ionic conductivity and does not influence the electronic conductivity, this effect can easy be observed experimentally.

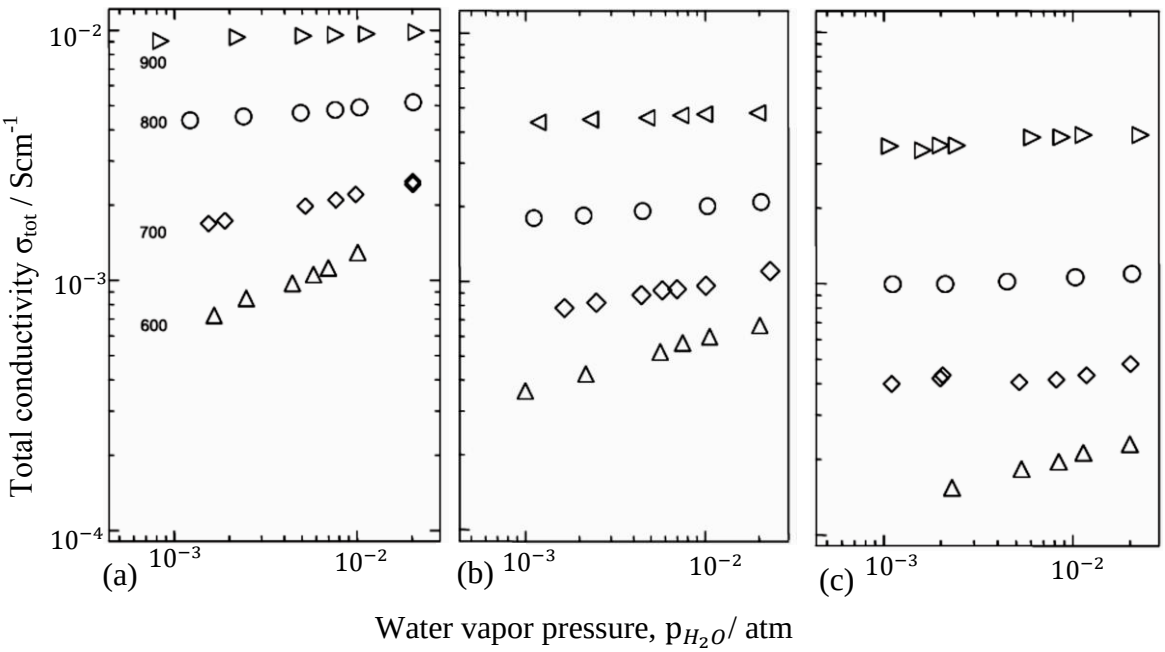

Figure 3.13. The total conductivity as a function of water vapor pressure under H_2 + 2.5 %H_2O at different temperature from 600 °C to 900 °C for undoped LWO6 (a), 0.5% Ca-doped LWO6 (b) and 5% Ca - doped LWO6 (c) [11].

3.5 Grain boundary conductivity

High grain boundary resistance may limit the performance of an oxide as a good protonic conductor. The origin of such effect explained by a space charge theory [28-30]. The grain boundary has usually a positive excess charge in a form of oxygen vacancies, which leads to the depletion of vacancies in the grain interiors. The grain boundary conductivities are more than one order of magnitude lower than that corresponds to the bulk [30].

The contribution of grain boundaries to the total conductivity in LaWO of different compositions was studied. The impedance spectra presented by Magrasó et al. [17] at low temperatures shows the contribution of grains, grain boundaries and electrodes, where the grain boundary contribution is small in hydrogen and argon, while it increases with increasing p_{O_2}(Figure 3.14).

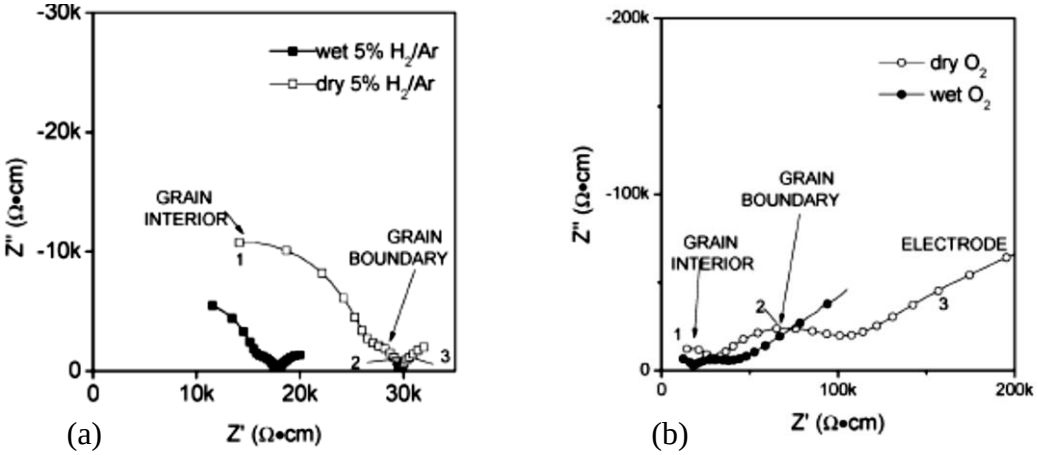

Figure 3.14. Nyquist plots for LWO56 recorded at 300°C under wet and dry H_2 (a) and wet and dry O_2 (b). Numbers 1, 2 and 3 correspond to frequencies 1MHz, 1kHz and 10 Hz respectively [17].

The conductivities of the grain interiors are not very different for $La/W_{nominal}$ composition from 6.0 to 5.4, but it was reported that La-rich phases show higher conductivity at high temperatures, while La-deficient phases show higher conductivity at low temperature (Figure 3.15). The same results were reported earlier by Yoshimura et al [18] (Figure 3.5).

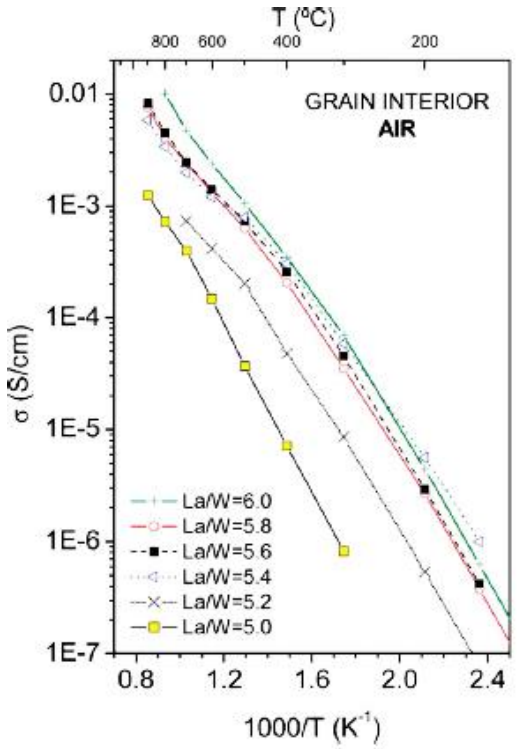

Figure 3.15. Grain interior conductivity for different La/W compositions in air [17]

4 Experimental

This chapter describes the experimental methods that were used in this master work. First, the synthesis and sintering of 2Ce-LaWO and 5Ce-LaWO will be presented. After that, the characterization will be described. The experimental part for the conductivity measurements will be provided with the setup and description of the experiment. Sources of errors and uncertainties will finally be discussed at the end of this chapter.

4.1 Sample preparation

4.1.1 Synthesis

The material investigated in this master thesis was synthesized by a wet-chemical gelation method, following the procedure as reported for synthesis of undoped LaWO. This method is "effective to obtain stoichiometrically complex polymetallic systems with milder thermal treatments compared to the conventional solid state route" [17]. One of the reasons for choosing this method for this particular material is that W forms volatile oxidic species, WOx that may evaporate at high temperature and therefore can introduce deviations from the nominal composition in the final product.
In wet chemical synthesis routes the cations are stabilized in the solution by a complexing agent with a stoichiometric ratio between the cations. The precursor usually therefore contains organic compounds that burn of easily at not very high temperatures.
The powder of lanthanum tungstate with the cation ratio La/W = 5.4 (LaWO54) and 2% (Samples 1 and 2) and 5% (Sample 3) doped with Ce was prepared starting from La_2O_3 (Sigma-Aldrich, 99.99%), WO_3 (Fluka, 99.99%) and $Ce(NO_3)_3$ (Fluka, 99.9 %). ETDA, ethylenediaminetetraacetic acid (Aldrich, 99.99%) was used as a complexing agent.
The starting compounds were first weighed roughly on an analytical balance (Sartorius, ED224S) and then dried in separated alumina beakers in order to remove the water absorbed by the powder. La_2O_3 was dried and decarbonized at 1000 °C overnight, while WO_3 and $Ce(NO_3)_3$ oxides were dried at 200 °C for 2 hours. Finally

three oxides and EDTA were weighted accurately according to the desired stoichiometry.

La_2O_3 and $Ce(NO_3)_3$ were dissolved in diluted nitric acid, and WO_3 was dissolved in an ammonium hydroxide solution. The last one was heated up under stirring until the solution became transparent.

After preparing both solutions, EDTA was added to each of them. Both solutions were neutralized to pH ≈ 7 - 8. After neutralization, they were mixed together and heated up under stirring in order to evaporate excess of ammonia. After standing overnight, the solution became dry and solid.

The precursor was then heated in a heating cabinet first at 150 °C for some minutes and then at 200 °C for approximately half an hour for initial combustion. After the combustion, solid became white and a coral-like structure was formed. The solid was crushed and the powder was calcined at 700 °C (Sample 1), 1000 °C (Samples 2 and 3) for 11 hours. After the calcination, fine, fluffy, white powder was observed. Calcination of Sampler 1 was repeated at 1000 °C.

4.1.2 Sintering

Before the sintering, the powder was ground together with a binder (polymer B-60 and B-70 dissolved in ethyl acetate) to increase the density of the green body. The powder of 2Ce-LWO was divided into two parts and three pellets from each part were cold pressed with a nominal pressure of 100 ± 50MPa. In order to reach the highest density, different pressures and sintering temperatures were applied. All the samples were porous after the sintering, and increased pressure resulted in larger porosity on the surface. The measured after sintering densities were quite similar among all the pellets (see subsection 5.1 Table 5.1) and highest pressure resulted in higher surface porosity. One pellet with the highest density from each of two parts of 2Ce-LWO was finally chosen. These pellets were labeled as Sample 1 and Sample 2, respectively. The powder of 5Ce-LWO was presented by one pellet labeled as Sample 3 and cold pressured with a nominal pressure of 100 MPa.

The samples were sintered at 1500 °C, Sample 1 for 7 hours and Sample 2 and 3 – for 5 hours. The ramp rates were slightly different as shown in the temperature profiles presented schematically in Figure 4.1. After the sintering, Sample 2 was used for the thermogravimetric analysis, whereas Sample 1 and Sample 3 were used for the electrical conductivity measurements. The relative mass density of Sample 1 and Sample 3, used for the electrical measurements, were respectively 88% and 85%, which were calculated using the theoretical mass density of LWO of 6.395 g/cm^3 [17].

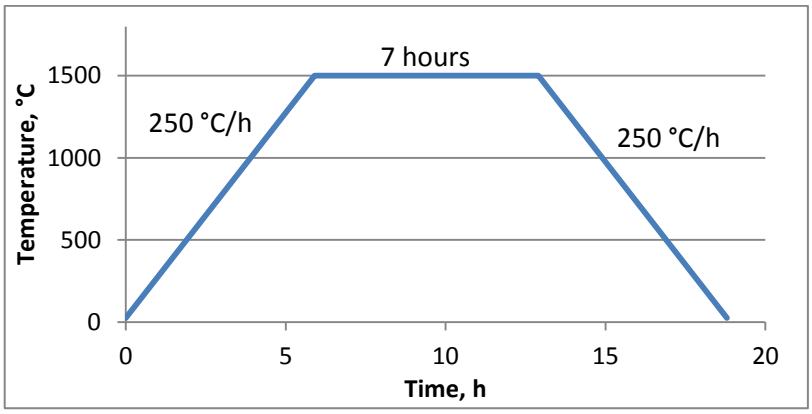

(a)

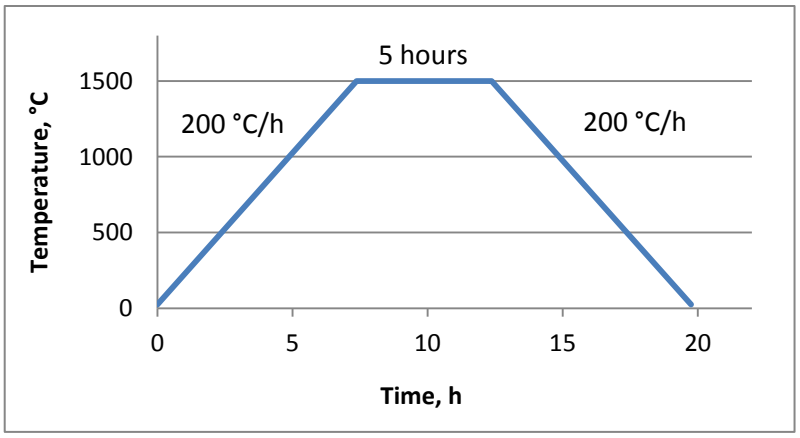

(b)

Figure 4.1. Temperature program profile for sintering Sample 1 (a) and Samples 2 and 3 (b).

4.1.3 Electrodes

Before starting the electrical measurements, the samples were assembled with Pt electrodes. For practical purposes, the electrode was in the form as squares: two square electrodes with size 0.84x0.84 cm^2 were cut from the platinum mesh and pressed flat. Then both sides of the sample (separately one by one) were painted with a layer of platinum ink with flux (Metalor Technologies Ltd, 6082 Pt – paste with flux) and dried at 150 °C for about 30 minutes. The platinum mesh was then placed on the top of each painted areas, covered with a new layer of a platinum ink and finally dried (150 °C for 30 min). The pellet with electrodes on both sides was annealed in air at 1000 °C for 3 hours to promote adherence and remove organic solvents from platinum coating. Figure 4.2 shows the pellet with electrodes ready for the electrical measurements.

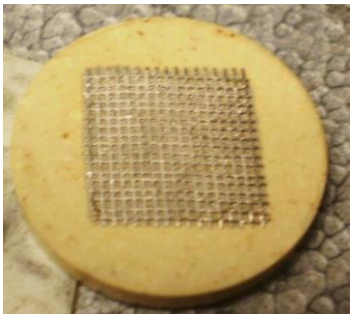

Figure 4.2. A Pellet (Sample3) with painted electrodes before the measurements.

4.2 Sample characterization

The samples were characterized with X- Ray diffraction (XRD), scanning electron microscopy (SEM) and electron probe micro-analysis (EPMA).

XRD was used to investigate for secondary phases and to determine structure of a sample, SEM with EDS detector was used to study the microstructure; surface, grains size, porosity, and also here probable precipitation of secondary phase. Additionally quantitative compositional analysis was carried out by mean of EMPA to more accurately determine the final cation stoichiometry of the samples.

4.2.1 X- Ray diffraction (XRD)

X-Ray diffraction is an analytical technique which gives information about crystal structure based on determination of the scattering of monochromatic X-Ray electromagnetic waves. These waves, called scattering beams, being reflected from the different planes, parallel to each other, give rise to a constructive interference or diffraction which obeys the Bragg's Law:

$$2dsin\,\theta = n\lambda \tag{4.1}$$

where d is the spacing of the crystal lattice planes, λ is the wavelength, θ is the angle of the scattering beam, and n is an order of reflection.
Crystallographic data is unique, when the intensity and position of the diffraction pattern is taken into account.

XRD of the samples were conducted before and after the sintering using a Bruker Advanced D8 diffractometer, running in Bragg-Brentano geometry with a Cu$K_{\alpha 1}$ radiation source with λ = 1.5406 Å in a 2θ range of 2-90°. After the electrical measurements the diffractometer of the Type Siemens D3 was used, running in Bragg-Brentano geometry with a Cr$K_{\alpha 1}$ radiation source with λ = 2.289 Å in a 2θ range of 2-90°. The experimental data was processed using FIFFRAC PLUS Eva program. The diffraction data was compared to literature and data base patterns.

4.2.2 Scanning electron microscopy (SEM)

A scanning electron microscopy can be used when characterizing microstructure and morphology of material. The surface is scanned with an electron beam, which interact with the atoms in the sample, giving different signals. These signals contain information about topography, morphology, chemistry, and crystallography of the sample. There are different detectors that catch electrons with different energies, or different signals. The analysis was carried about using a FEI Quanta 200 instrument with a field emission gun (FEG). This microscope can operate under both low and high vacuum.

The main signals that SEM detectors operate with are BSE – backscattered electrons, SE – secondary electrons and X-Rays. Secondary electrons have low energy and only those, which are coming from the surface region, can be detected. The SE gives mainly information about the topography of the sample. The BSE are elastically scattered electrons originating from the beam. They have high energy and can provide information about different type of elements presented on the surface. Those electrons are used to detect phases, contrast between areas with different chemical composition. These electrons give 3d appearance of the surface where the brightness depends on the atomic number, surface curvature and the beam energy. The main theory behind is that heavy elements with high atomic number scatter electrons more strong than light elements with low atomic number. X-Ray – photons that also being produced by the interaction of an electron beam with a sample. They appear when the electron beam remove an inner shell electron from the sample, causing the electrons with higher energy to fill the shell and thus release the energy. X-rays are a fingerprint of each element that being detected by EDS detector. The detectors that were used under the sample characterization are presented at the Table 4.1.

Table 4.1 The detectors that were used under the sample characterization.

LFD	SE detector under low vacuum
ETD	SE detector under high vacuum
SSD	BSE detector
EDS	X-Ray detector

4.2.3 Electron probe micro-analysis (EPMA)

EDS analyses in the SEM have generally rather large uncertainties and, the present composition is particularly challenging, due to the partly overlapping of La and Ce peaks in the spectrum. Consequently the EDS results can only be considered as semi quantitative and therefore electron probe micro analysis was used in addition.

This principle of material characterization with EPMS is similar to EDS, but differs by the capability of chemical analysis. Operating with a different detecting system for the X-rays, a WDS (wavelength-dispersive spectroscopy) detector reads only the x-

ray of single wavelengths at a time, which makes this technique be more precise in the element identification. EPMA measurements were carried out before and after electrical measurements for Sample 2, while Sample 3 was characterized after the electrical characterization only.

For the sample preparation a fragment of the sample was placed in a circular mold and casted into resin (DuroCit powder and DuroCit liquid in a proportion 25 : 9) and left approximately 30 minutes for drying. Then the sample was grinded and polished. Wet grinding was carried out with waterproof silicon carbide (SiC) papers (Struers), with steps of finer paper (220, 500, 800, 1000, 1200, 4000 mesh). The polishing was carried out in steps on special cloths with slurries of fine diamond particles, ranging in size from 6μm to 0.25 μm. A diamond spray (Struers) was used. After polishing, the sample was finally coated with a 30-60 nm thick carbon film. Figure 4.3 shows a picture of a 2Ce-LWO sample that was placed horizontally into the sample holder and investigated before the electrical measurements (a); in (b) one and 2Ce-LWO and 5Ce-LWO sample placed vertically together in one sample holder and investigated after the electrical measurements.

(a) (b)

Figure 4.3. The samples for EPMA analysis. 2Ce-aWO sample placed horizontally into the resin (a), 2Ce-LWO and 5Ce-aWO samples places vertically into the resin (b).

The measurements were conducted using Cameca SX100 electron microprobe instrument with nominal voltage of 15kV and current 20nA. Before the measurements, the instrument was calibrated with accuracy to $La_{L\alpha}$, $W_{M\alpha}$ and $Ce_{L\alpha}$ peaks.

Backscattered electrons (BSE) were used for imaging of the surface and locate places for the spot analysis and the element mapping.

4.3 Apparatus

4.3.1 Measurement Cell

The measurements were done with a Probostat cell (NorECs AS). The sketch of such a cell is presented in Figure 4.4(a,b). With this cell it is possible to perform electrical measurements at different temperatures and gas atmospheres.

The sample with painted electrodes was resting on top of the Probostat support tube between the bottom and the top current collector/voltage probes, as shown in Figure 4.4 (c,d). After making sure that the electrodes on both sides of the sample were in contact with the current collector/voltage probe, the assembly was spring-loaded with an alumina disc. The thermocouple was positioned as close as possible to the sample, in order to avoid deviations between the samples' temperature and the set point temperature. The set-up was sealed with an outer quartz (setup 1) and alumina (setup 2) tube.

Both outer gas tube and inner gas tube were used to supply the same gas in this project, while the cell could operate two different gasses. Both current collectors/voltage probes were Pt wires, meanwhile the thermocouple consisted Pt and 10 % Rh. Finally the cell mounted vertically into the furnace. The measurements were first carried out with Sample 2 under setup 1 and then with Sample 3 under setup 2.

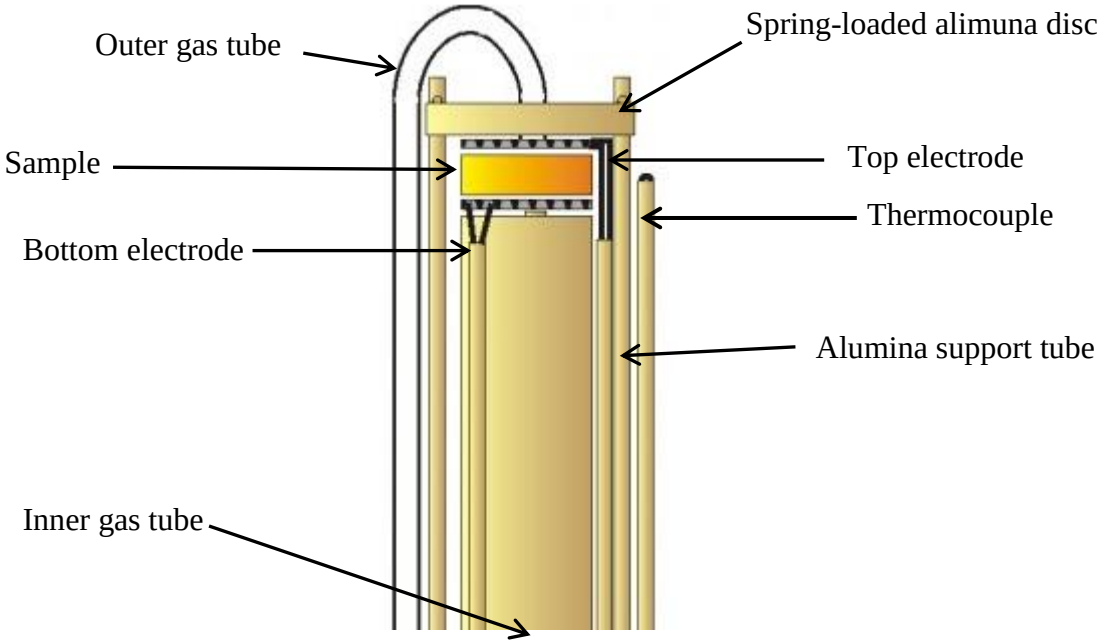

(a)

(b) (c) (d)

Figure 4.4. Sketch of the Probostat measurements cell, modified from [31] (a), and image of the measurement cell that was used during the measurements [31] (b), photos of the measurement cell after the measurements with and without a spring-loaded alumina disc (c) and (d).

4.3.2 Gas mixer

In order to supply the measurement cell with gas, it was connected to a gas mixer (Figure 4.5). To study the conductivity of a material as a function of oxygen partial pressure and water vapor pressure, the gas mixer was used to control the atmosphere in the measurements cell, obtaining the desired partial pressures..

To control the oxygen partial pressure Air, O_2, H_2 or Harmix (5% H_2 in Ar) (G1 at the scheme) could be diluted with an inert gas such as N_2, Ar or He (G2 at the scheme). Ar was chosen as G2 for all the conductivity measurements. Mixing G1 and G2 gave Mix 1, which could be further diluted with G2, giving what is denoted Mix2, etc.

There were totally 9 flowmeter in use: eight of them were connected in pairs and formed four stages of gas mixer, while last one controlled the gas flow that entered into the cell. The first 6 flowmeters gave three mixes: Mix1 (G1 + G2), Mix2 (Mix 1 + G2) and Mix3 (Mix 2 + G2). The gas composition and hence pO_2 could be controlled by varying the flow in these flowmeters. The last pair of the flowmeters was connected to wetting and drying stage and controlled the ratio between the wet and dry gas, respectively. The maximum humidification of Mix3 could be achieved by sending the gas through a bottle with H_2O/D_2O and then a saturated solution of KBr, yielding a water vapor pressure of 0.025 atm at 25 °C. Drying of Mix3 was done by sending the gas through a bottle with P_2O_5. The theoretical level of water in the gas after the drying stage is 0.1 ppm, but due to gas leakages in the set-up, the dry mixture contains a small amount of water and the estimated experimentally value of water partial pressure if about $3x10^{-5}$ atm [32]. By varying the flow in these two flowmeters, the desired p_{H_2O} of Mix4 could be achieved. The last flowmeter controls the gas flow of Mix4 that enters the cell. To establish a certain overpressure pressing the gas through gas mixer, blowing gas out in case of leakages, and "remove" excess gas due to dilution, bubblers were placed behind each mixing stage. These were filled with dibutyl phthalate in a decreasing height, from the first to the last mixing stage, so that the overpressure decreases through the gas mixer. Each bubbler was connected to the ventilation. In order to calculate p_{O_2} and p_{H_2O}, the computer program *Gasmix* version 0.5 was used [33].

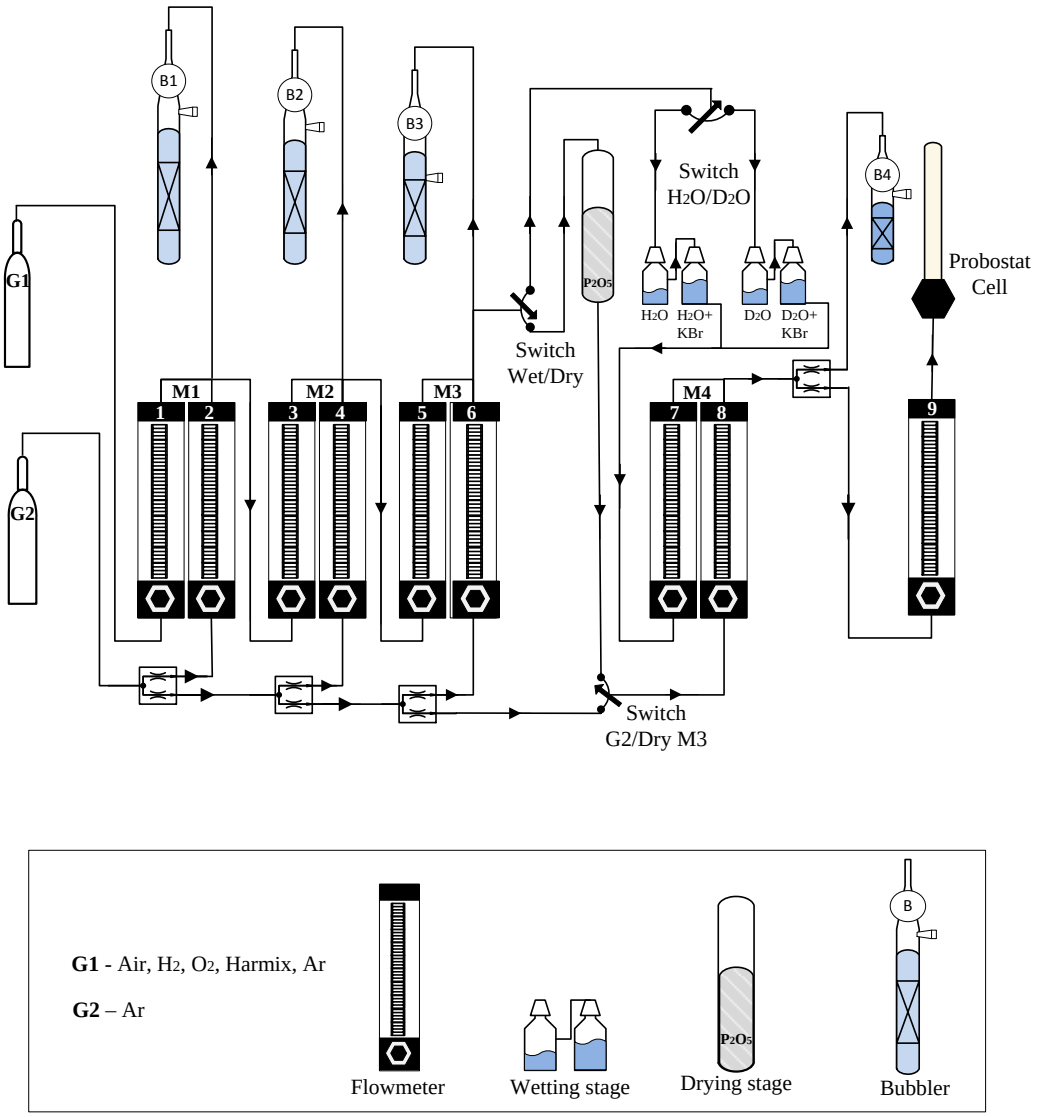

Figure 4.5. Sketch of the gas mixer used for the electrical measurements was drawn using the program Microsoft Visio [34].

4.3.3 Thermogravimetric analysis

Thermogravimetric analyses were used to monitor the relative mass change of the sample as a function of temperature under isobaric conditions. This process is described by the characteristic hydration reaction (Equation 2.41). The instrument that was used for the measurements is a Netzsch STA449 F1 Jupiter. The measurements were conducted in wet and dry oxygen; and wet and dry argon as a function of temperature (p_{H_2O} for wet and dry atmospheres are 0.025 and $3\text{x } 10^{-5}$ atm respectively as was mentioned in subsection 2.3.2).

The sintered Sample 1 was crushed into powder and then transferred to special alumina crucibles for the TG. The temperature program used for these measurements is illustrated in Figure 4.6. Starting from 1000 °C, the temperature was decreased with steps of 50 or 100 followed by isothermal annealing of 30 min – 5 hours – increasing duration as the temperature decreases. The gas atmosphere was constant during each TG measurement.

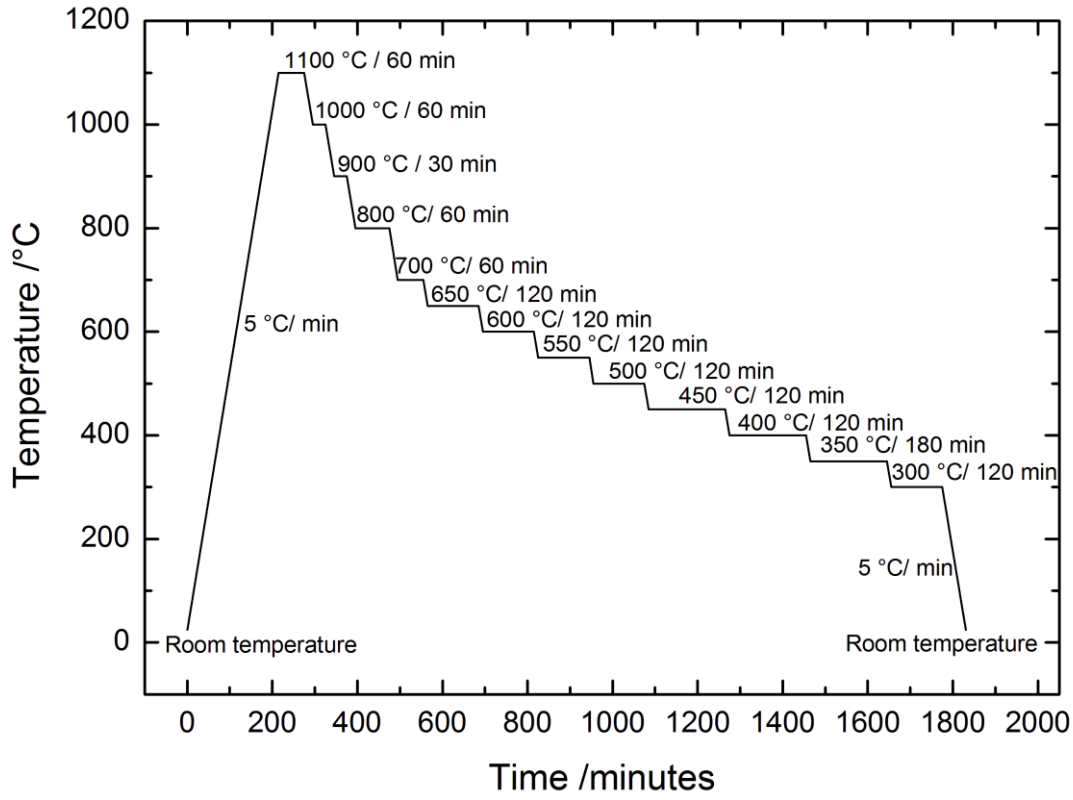

Figure 4.6. A temperature profile that was used for the thermogravimetric measurements.

4.4 Electrical measurements

The electrical measurements were conducted using a 4-wire 2-electrode set-up (two-probe technique). A HP4192A spectrometer was connected to a multiplexer (Pickering), that makes it possible to process several signals from different devices or resources. The total conductivity was measured at 10 kHz with an oscillation voltage 0.5 V.

The impedance measurements as a function of frequency between 0.5 Hz to 2 MHz were carried out with a Solatron 1260. This spectrometer was connected separately to the cell and had an input impedance of 1 MΩ, frequency range from 10μHz to 30 MHz and an accuracy of 0.12% [35]. The impedance sweeps were taken at different temperatures and atmospheres, and the data was deconvoluted and analyzed with the software Equivalent Circuit 2D (EQC), version 1.2 [36].

Figure 4.7 shows a model of an equivalent circuit that was used for the data deconvolution.

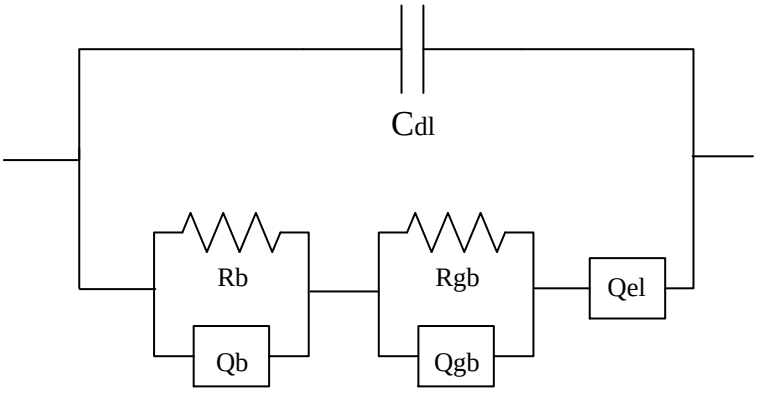

Cdl – blocking electrode	
Qb – CPE of grain interior	Rb – resistant of grain interior
Qgb – CPE of grain boundary	Rb – resistant of grain boundary
Qel – CPE of electrode	

Figure 4.7. An Equivalent Circuit model that was applied for the deconvolution of the impedance sweeps.

The measured conductivity, σ, was corrected for the sample geometry and porosity. The conductivity is material specific and the correction was done by multiplying the conductance with a geometrical factor:

$$\sigma_{measured} = G\frac{d}{A} \tag{4.2}$$

were G is a conductance taken from the measurements, d is the sample's thickness, A is the area of the electrodes [37]. The measured conductivity was also corrected for porosity:

$$\sigma_{measured} = \sigma * p^2 \tag{4.3}$$

where p is the relative density of the sample [38].

4.5 Sources of errors and uncertainties

In the experimental part of this work, some uncertainties will be presented and errors may occur. It is difficult to avoid them, however is it important to be aware of them in order to reduce them and take them critically into account when interpreting the results.

During synthesis and sintering, contamination may occur. SEM and XRD techniques were used in order to detect such potential impurities and determine the stoichiometry of the compounds. Since SEM micrographs did not show indication of any secondary phases in the bulk and EDS analysis had large uncertainties in founding a composition due to the partly overlapping La and Ce peaks, EPMA technique was used.

XRD technique has an error of each peak position of less than $\pm 0.01°$ over the entire angular range [39] and therefore, this instrument might not detect small amounts of impurities and secondary phases.

During measuring the samples geometrical parameters, their density and weight, small errors could be included. These uncertainties however have a small impact to the experiment and are as such negligible.

Large uncertainties are connected to the electrical measurements. Firstly there are relatively large uncertainties in the gas compositions. Reasons are the inaccuracy of the flowmeters and uncertainties in the values. To increase the accuracy, recommended flow at flowmeters should be higher than 20 mm and lower than 130 mm. The gasmixer itself may also have leakages, which will influence the gas composition introduced to the sample, and even leakage in the Probostat cell may be present. When using a dry gas, one should be aware that it would contain about 30 ppm of water [32].

When using argon, it will be also uncertainties in determining the oxygen partial pressure, since it contains some oxygen. These will lead to some uncertainties and deviations in calculation of partial pressures of oxygen and water. The purity of the used gases should also be considered. The gases used in the thesis had purity 99.999 %, with the exception of oxygen, which had a purity of 99.5%.

Under impedance measurements, the measurement cell will contribute with a background capacity of 5pF, which will create parasitic impedance. This value is included under the deconvolution (see Figure 4.7).

5 Results

In this chapter the results from the measurements will be presented. The first section will present an overview of the sample characterization from XRD, SEM and EPMA techniques. This will be followed by results from the electrical measurements, impedance spectroscopy and thermogravimetry.

5.1 Sample characterization

This part includes the sample characterization that was done both before and after the electrical measurements. Abbreviations for the samples were given in subsection 4.2.1, and Table 5.1 shows a review of them. All the samples were characterized after sintering, while Sample 2 and Sample 3 were also characterized after the electrical measurements.

Table 5.1. Samples composition and relative density.

Sample N		Composition	Relative density, %
Sample 1	2Ce-LWO	$La_{26.46}Ce_{0.54}W_5O_{55.5+\delta}$	88.7
Sample 2			88.5
Sample 3	5Ce-LWO	$La_{25.65}Ce_{1.35}W_5O_{55.5+\delta}$	85

5.1.1 X- Ray diffraction (XRD)

XRD was used to investigate the crystal structure of the samples and to detect possible secondary phases. XRD was performed after each calcination step and also after both samples were investigated for the electrical measurements.

Figure 5.1 shows the XRD patterns of 2Ce-LWO and 5Ce-LWO after the calcination at 1000 °C and compared to undoped LWO. New peaks emerged at $2\theta \sim 29°$ and their intensity increased with level of donor dopant. This reveals a possible formation of a secondary phase.

The peaks of the secondary phase were quite similar to those of $La_6W_2O_{15}$, reported by Magrasó et al. [17] (Figure 3.2), but they were not identified by EVA Plus program, neither any other phase.

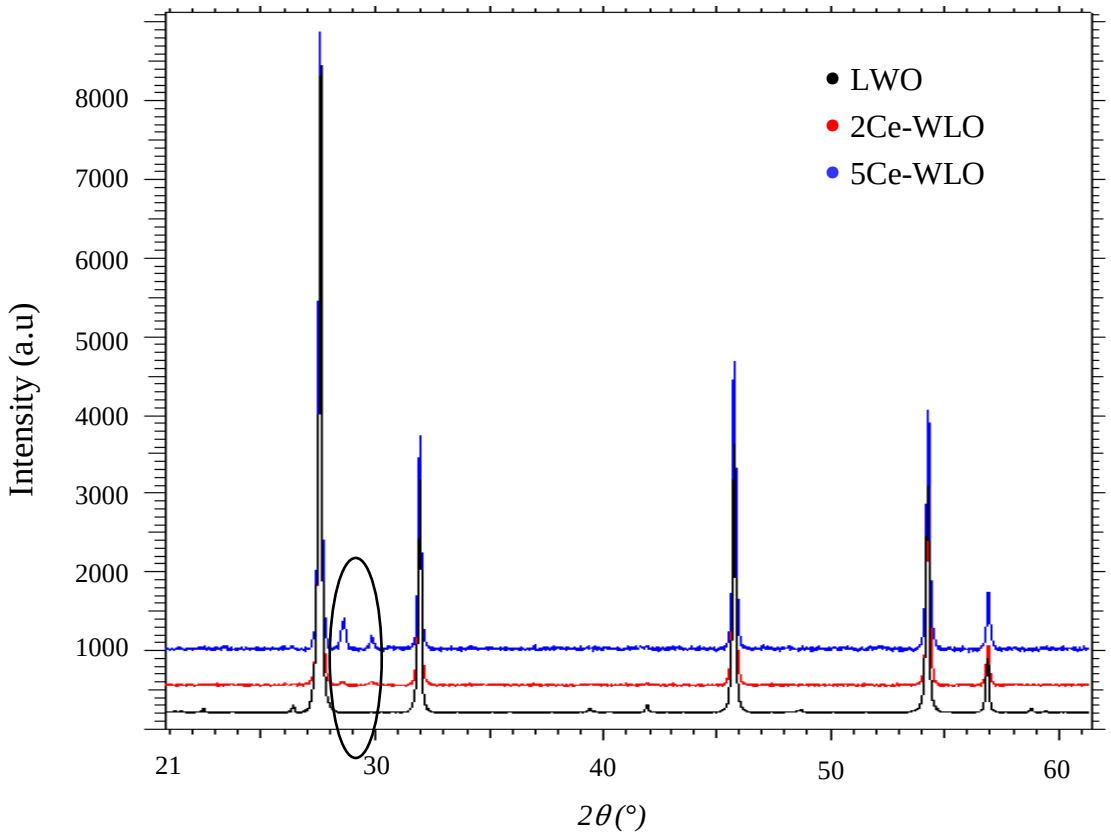

Figure 5.1 XRD patterns measured at room temperature of 2Ce-LWO and 5Ce-LWO after the calcination.

The XRD pattern of 5Ce-LWO was analyzed by the Rietveld refinement technique as it had highest intensity of the identified peaks (Figure 5.2). The pattern of 5Ce-LWO was fitted to the cubic structure with the space group $F\bar{4}3m$, as that corresponds to LWO [17]. Although the peak positions of the secondary phase did not match any of the space groups of $La_6W_2O_{15}$ reported by Chambrier et al. [26], this phase may still be ascribed to $La_6W_2O_{15}$.

The cubic lattice parameter of 5Ce-LWO was finally estimated to be a =11.163 Å being smaller than that of undoped LWO54 (a = 11.175 Å) [17].

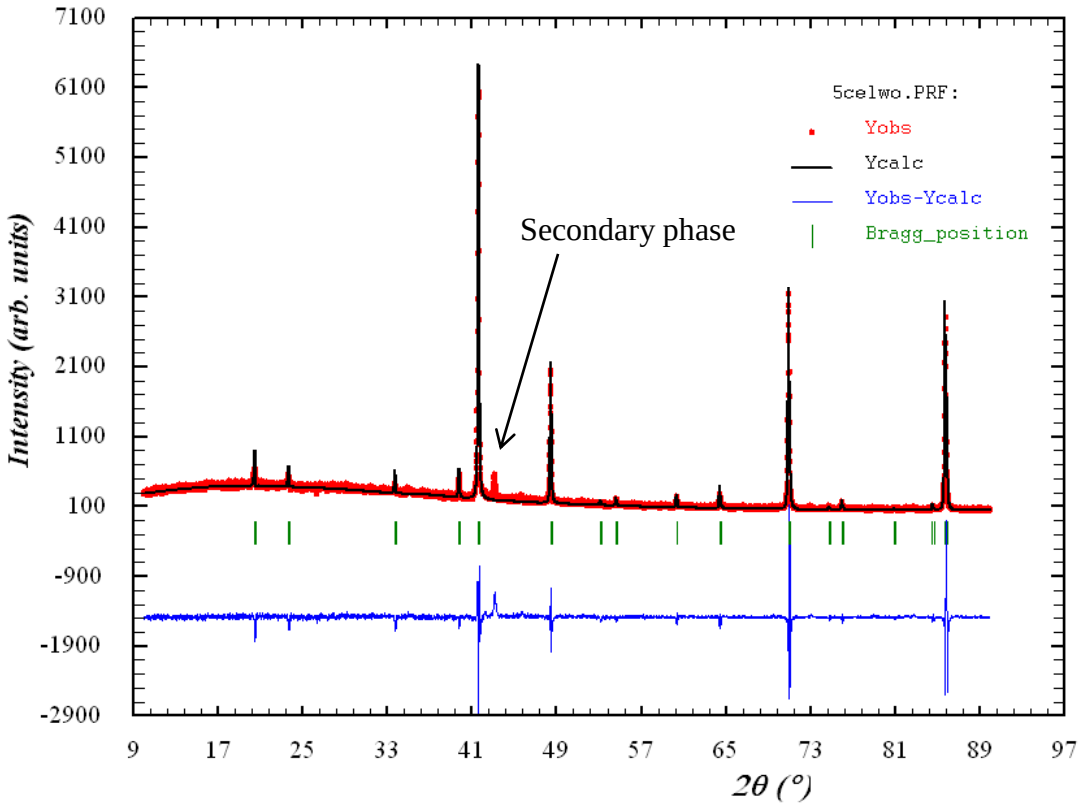

Figure 5.2. Rietveld refinement of 5Ce-LWO fitted to the cubic structure with the space group $F\bar{4}3m$.

5.1.2 Scanning electron microscopy (SEM)

All the samples were characterized with SEM both before and after the electrical measurements. SEM micrographs of 2Ce-LWO are represented by Sample 1 and Sample 2 in Figure 5.3 revealing with grain sizes ranging from 1.5 µm to 16 µm. Sample 1 was pressed under higher pressure than Sample 2 and its surface was more porous, whereas the overall final density of both samples was similar (Table 5.1). Figure 5.4 presents a SEM image of the surface of 5Ce-LWO. No secondary phase was detected and with grain sizes from 0.74 µm to 4.4 µm, i.e. smaller grains than for 2% Ce-doping.

Sample 1 and Sample 3 were used for the electrical measurements. After the measurements both pellets were broken into pieces and both the surface and cross section were investigated. The surface of 2Ce-LWO showed small grains of different phases. The particles were brighter than the main phase with a particle size less than 1

μm. This can be seen in Figure 5.5(a), which both shows the topography of the sample and the formation of a secondary phase. The surface of 5Ce-LWO after the electrical measurements also showed precipitation of a secondary phase as shows in Figure 5.5(b). This phase appeared in a form of small particles on top of the LWO grains.

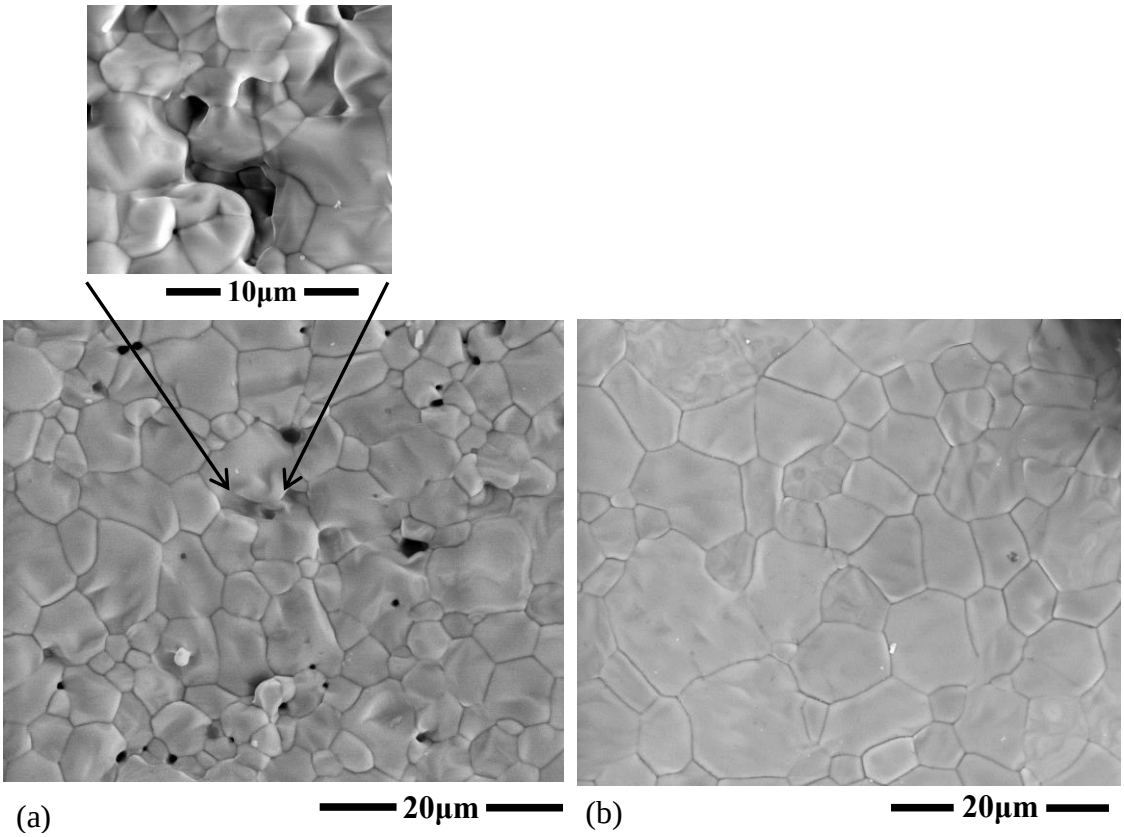

Figure 5.3. SEM images of Sample 1(a) and Sample 2(b) of 2Ce-LaWO represent the surface topography.

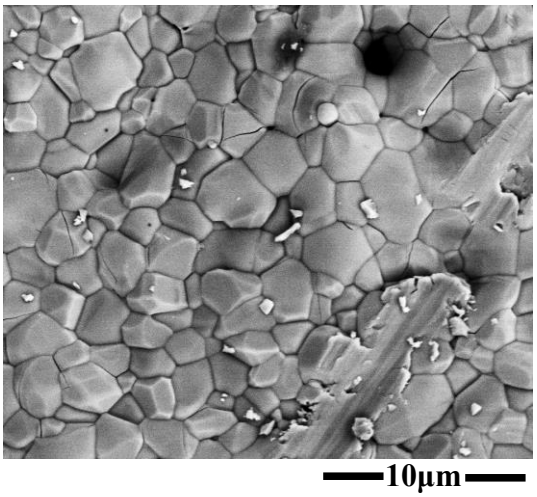

Figure 5.4. SEM image of 5Ce-LaWO represents the surface topography using both LFD and SSD detectors under high vacuum.

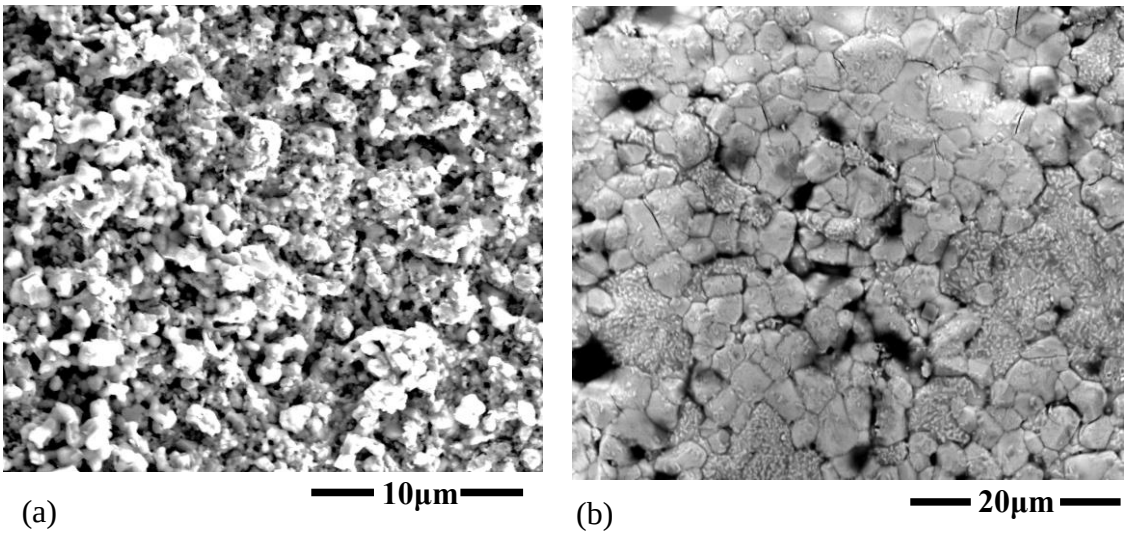

(a) (b)

Figure 5.5. SEM images of 2Ce-LWO (a) and 5Ce-LWO (b) after the measurements represent the surface topography.

The surface particles were observed most at 2Ce-LWO and in lower concentration at 5Ce-LWO (Figure 5.5), possibly because the samples had different thermal history.

The composition of the samples was determined using the SEM EDS detector both before and after the electrical measurements. The composition was slightly different than the nominal composition and changes during the electrical measurements. Table 5.2 summarizes the composition (in At %) for 2Ce-LWO and 5Ce-LWO before the measurements. The analysis of both samples indicates less La and more W and Ce on the surface than expected. The same trends were observed after the electrical measurements. The EDS spot analysis of 2Ce-LWO and 5Ce-LWO detected more La on the surface and more W inside the sample (Table 5.3). The amount of W in 2Ce-LWO is redistributed between the surface and the cross section (CS), distinguishing two phases: bulk and surface, while the amount of W in 5Ce-LWO is generally lower than it was expected (Table 5.3). Ce in both samples appears in large amount than expected, but this can be due to the uncertainties of Ce identification by EDS analysis. Tables 5.2 and 5.3 show the composition from different spots of 2Ce-LWO and 5Ce-LWO, before and after the electrical measurements respectively.

Table 5.2. At% of different elements from the spot analysis of 2Ce-LWO and 5Ce-LWO, using the EDS detector, against expected At%. Before the measurements.

	2Ce-LWO			5Ce-LWO	
Element	**Average**	**Expected**[1]		**Average**	**Expected**
La	78.16	82.7		76.13	80.15
W	18.53	15.6		17.87	15.62
Ce	3.24	1.68		5.82	4.2

Table 5.3. At% of different elements from the spot analysis of 2Ce-LWO and 5Ce-LWO, using the signal from EDS, against expected At%. After the measurements

	2Ce-LWO				5Ce-LWO		
Element	**Average CS**	**Average Surface**	**Expected**		**Average CS**	**Average Surface**	**Expected**
La	76.57	83.17	82.68		82.8	84.47	83.3
W	17.58	11.72	15.6		6.54	9.88	15.63
Ce	5.8	5.1	1.68		10.16	5.64	4.2

5.1.3 Electron probe micro-analysis (EPMA)

Since the exact composition observed by the EDS analysis is uncertain, EPMA analyses were performed to study the atomic composition of the samples (more clear-was in section 4). This analysis of the bulk discovered precipitation of a secondary W rich phase in all the samples both before and after the electrical measurements. Table 5.4 shows the composition (in At %) of the two different phases observed in 2Ce-LWO before the electrical measurements. The measured composition of phase 1 was close to the nominal one, while the composition of phase 2 corresponds essentially to $La_6W_2O_{15}$, which has been detected by XRD analysis of undoped LWO with the nominal La/W ratio less than 5.3 (section 3.1.2) [17]. Figure 5.6 shows a BSE image (a) and mapping area together with the content of La, W and Ce (b). The brighter dots the higher concentration of the element. From the mapping the secondary W rich phases (bright spots at W content) correspond to deficiency of Ce (dark spots at Ce content). La is uniformly distributed over the whole mapping area.

[1] The expected elemental compositions were calculated from the formula units presented in Table 5.1

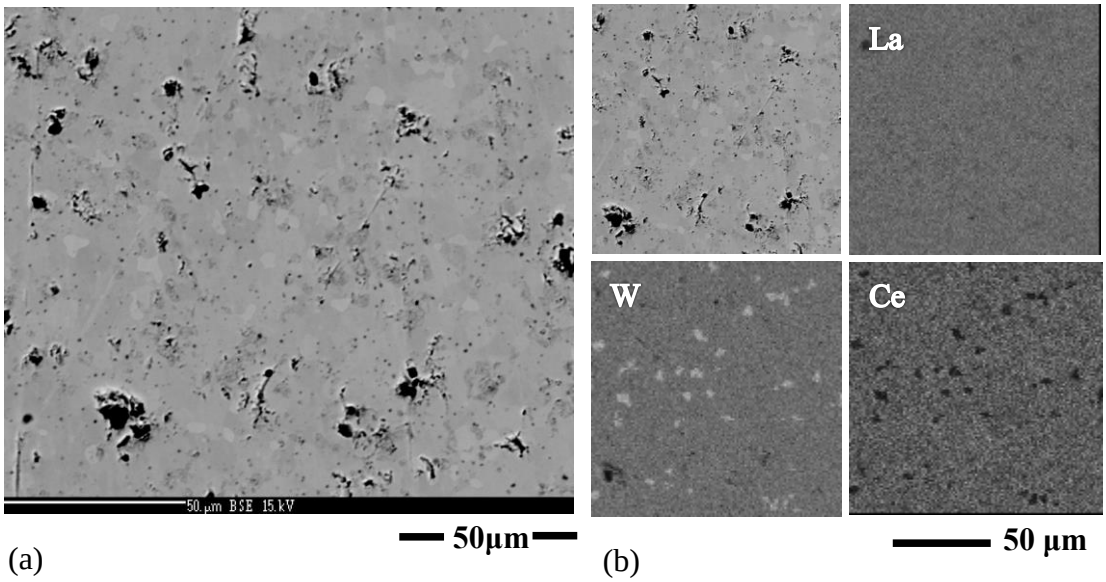

Figure 5.6. EPMA image of 2Ce-LWO before the measurements using BSE signals (a), and the content of La, W and Ce together with the scanning area (b).

Table 5.4. At% of different elements from the spot analysis of 2Ce-LWO using the WDS detector, against expected At%. Before the electrical measurements.

Element	Phase 1	Phase 2	Expected
La	30.56	27.68	30.17
W	5.5	7.7	5.7
Ce	0.62	0	0.61
O	63.3	64.62	63.51

EPMA analysis of the samples after the electrical measurements was performed as well. Figure 5.7(a) and Figure 5.8(a) show images from BSE signals of 2Ce-LWO and 5Ce-LWO respectively. The bright, dark and grey spots observed by BSE signals were analyzed by WDS detector. The measured composition did not differ much between these spots (Table 5.5 and 5.6). The mapping area together with elemental mapping of La, W and Ce of 2Ce-LWO and 5Ce-LWO is presented in Figure 5.7(b) and Figure 5.8(b) respectively. It shows W rich phases, which correspond to the bright spots in the BSE image, while the atomic composition did not show significant difference in composition between bright and other spots. This was not expected from the elemental mapping. The WDS analysis detected more La and less W compared to the expected values. The composition (in At %) of the different spots of 2Ce-LWO and 5Ce-LWO is presented in Table 5.5 and Table 5.6 respectively.

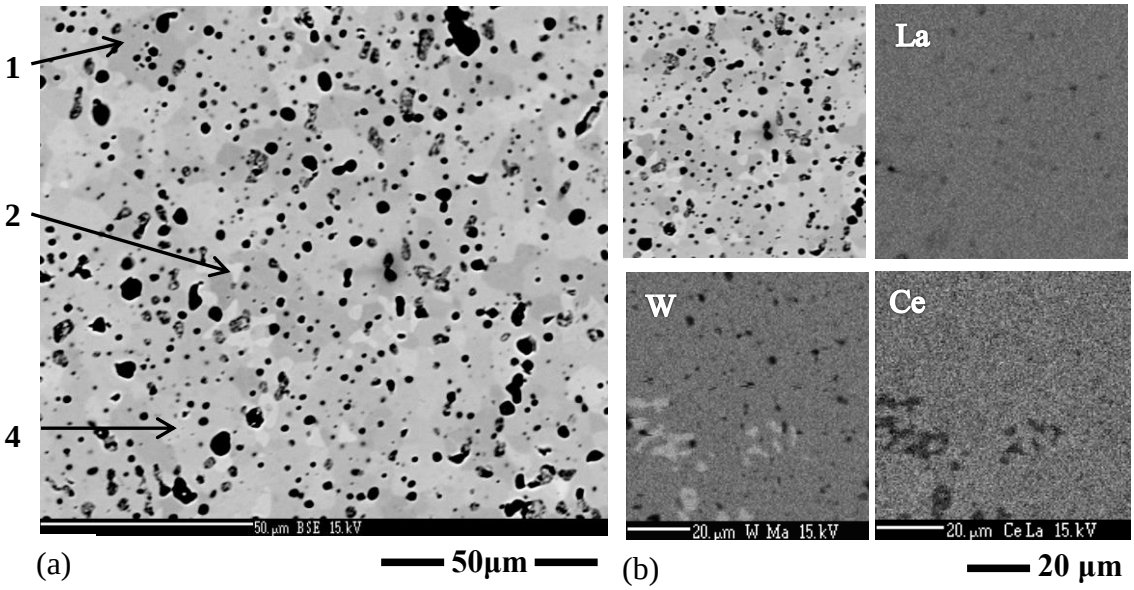

Figure 5.7. EPMA image of 2Ce-LWO after the measurements using BSE signals (a), and the content of La, W and Ce together with the scanning area (b).

Table 5.5. At% of different elements from the spot analysis of 2Ce-LWO using the WDS detector, against expected At%. After the electrical measurement.

Element	Dark		Bright		Grey	Average	Expected
	Spot 1	Spot 3	Spot 2	Spot 5	Spot 4		
La	30.72	30.67	30.71	30.7	30.67	30.7	30.56
W	5.43	5.46	5.4	5.43	5.46	5.43	5.5
Ce	0.58	0.58	0.63	0.6	0.59	0.6	0.62
O	63.2	63.27	63.24	63.26	63.27	63.24	63.3

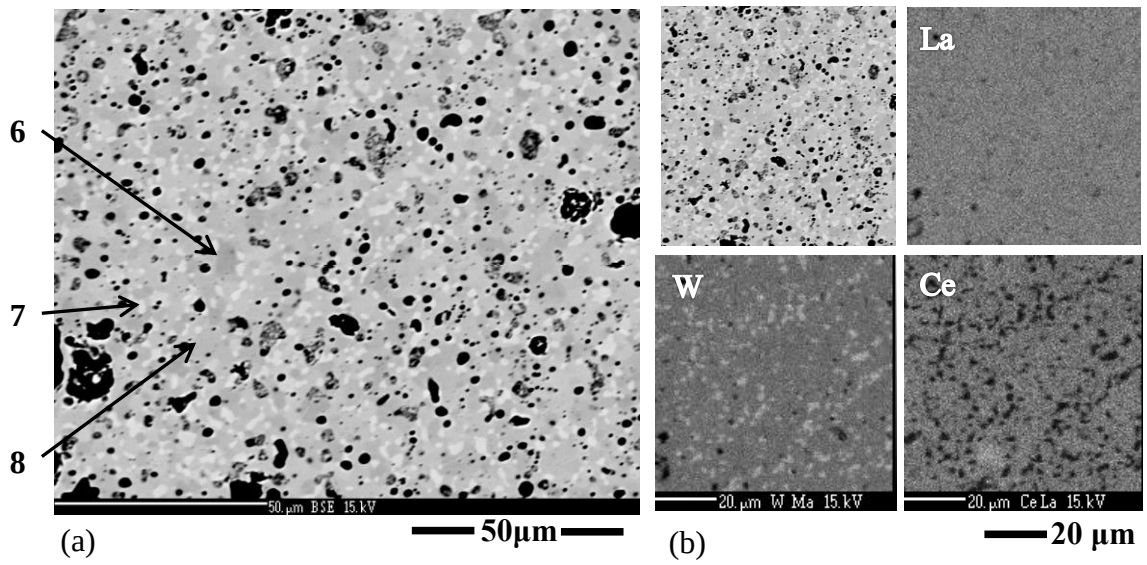

Figure 5.8. EPMA image of 5Ce-LWO after the measurements using BSE signals (a), and the content of La, W and Ce together with the scanning area (b).

Table 5.6. At% of different elements from the spot analysis of 5Ce-LWO using the signal from WDS, against expected At%. After the electrical measurements.

Element	Dark Spot 6	Bright Spot 7	Grey Spot 8	Average All spots	Expected
La	29.94	29	29.8	29.58	29.25
W	5.18	6.15	5.24	5.52	5.7
Ce	1.75	1.15	1.8	1.56	1.54
O	63.11	63.7	63.14	63.32	63.5

5.2 Electrical Characterization

5.2.1 Temperature dependency of the conductivity

The constant frequency (10kHz) total conductivity was recorded for both 2Ce-LWO and 5Ce-LWO as a function of temperature from 1000 to 300 °C in reducing (hydrogen) and oxidizing (oxygen) atmospheres. The results were plotted versus inverse temperature. Figure 5.9(a) shows the temperature ramps for the 2Ce-LWO in wet (both with H_2O and D_2O) and dry oxygen, while Figure 5.9(b) shows the total conductivity in wet hydrogen compare to wet oxygen. The total conductivity

decreases with decreasing temperature and it is lower in dry than in wet oxygen. Below 700 °C, the conductivity is higher in H_2O - wetted than in D_2O - wetted oxygen, which reflects effects of the protons on the conductivity. This indicates that the material has mixed conductivity: protons contribute at low temperature and dehydrate to form oxygen vacancies at higher temperature. It is expected that electrons and electron holes contribute as well, which will be verified by p_{O_2} dependencies.

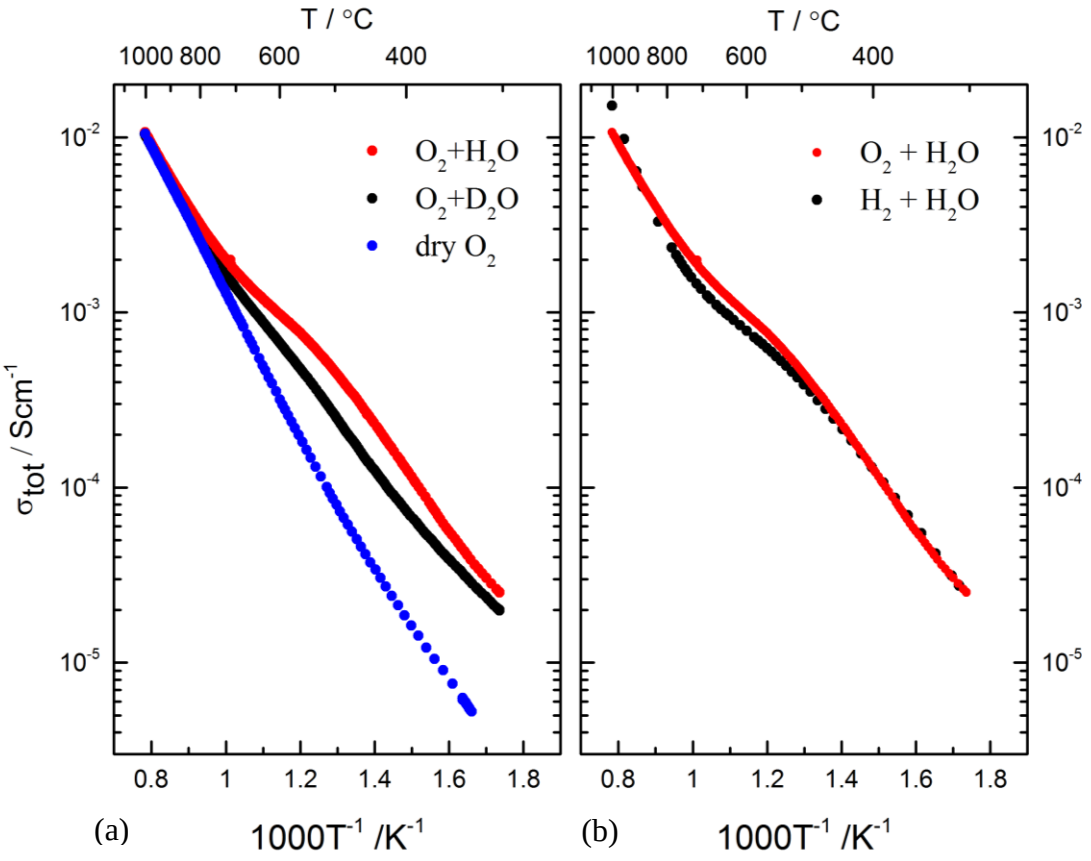

Figure. 5.9. The total conductivity as a function of temperature for 2Ce-LWO under O_2 + 2.5% H_2O, O_2 + 2.5% D_2O and dry O_2 (a); and O_2 + 2.5% and H_2 + 2.5% (b).

The indication of contribution from electronic defects to the total conductivity can be proved by comparing the temperature ramps for wet and dry argon, wet hydrogen and wet oxygen (Figure 5.10). There is no difference in the total conductivity for wet and dry argon at high temperature, while below 900 °C the conductivities in wet argon increases which indicates contribution of protons to the overall conductivity. Figure 5.10(a) shows the difference in the conductivities for wet hydrogen and wet argon at high temperature above 800 °C, which indicates contribution from electrons. Figure

5.10(b) shows the difference in the conductivities for wet oxygen and wet argon above 800 °C, which indicates contribution from electron holes.

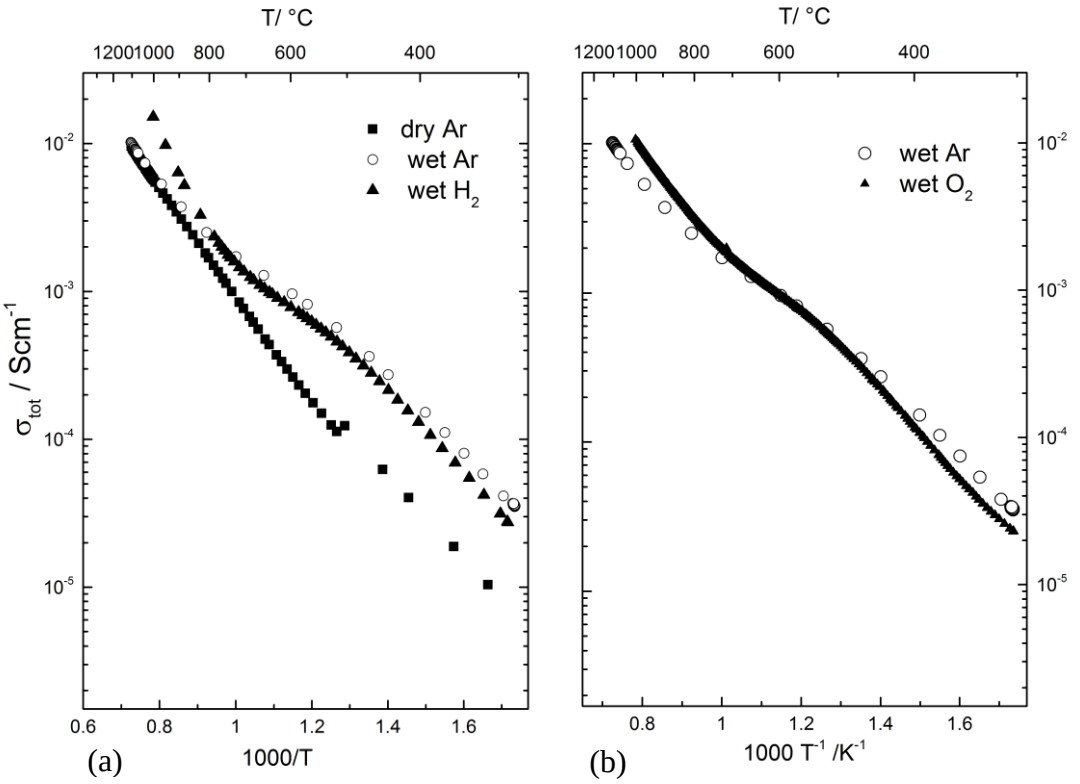

Figure 5.10. The total conductivity as a function of temperature for 2Ce-LWO under H_2 + 2.5% H_2O, Ar + 2. 5% H_2O and dry Ar (a) and under O_2 + 2.5% H_2O, Ar + 2. 5% H_2O (b).

The temperature ramps of the conductivity of 5Ce-LWO are presented in Figure 5.11. The conductivity in wet hydrogen is lower than in wet oxygen at the temepratures below 800 °C, but it is higher above this temperature, otherwise these two temperature ramps are almost identical to those for 2Ce-LWO (Figure 5.9(b)). The conductivity at high temperature is predominated by the electrons under reducing condition, while under oxidizing conditions the electron holes predominate. Comparing the dependencies of wet hydrogen for 2Ce-LWO and 5Ce-LWO, one can observe a steeper slope for the latter, which indicates an increasing contribution of electrons in this region.

To study the effect of different amount of Ce doping in LWO, the temperature ramps at wet oxygen and hydrogen were compared to each other for respectively 2Ce-LWO and 5Ce-LWO (Figure 5.12).

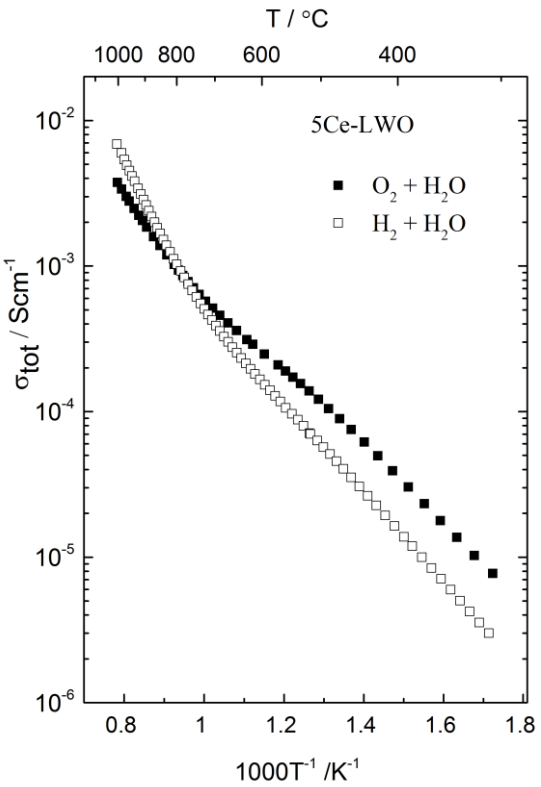

Figure 5.11. The total conductivity as a function of temperature for 5Ce-LWO under O_2 + 2.5% H_2O and H_2 + 2.5% H_2O.

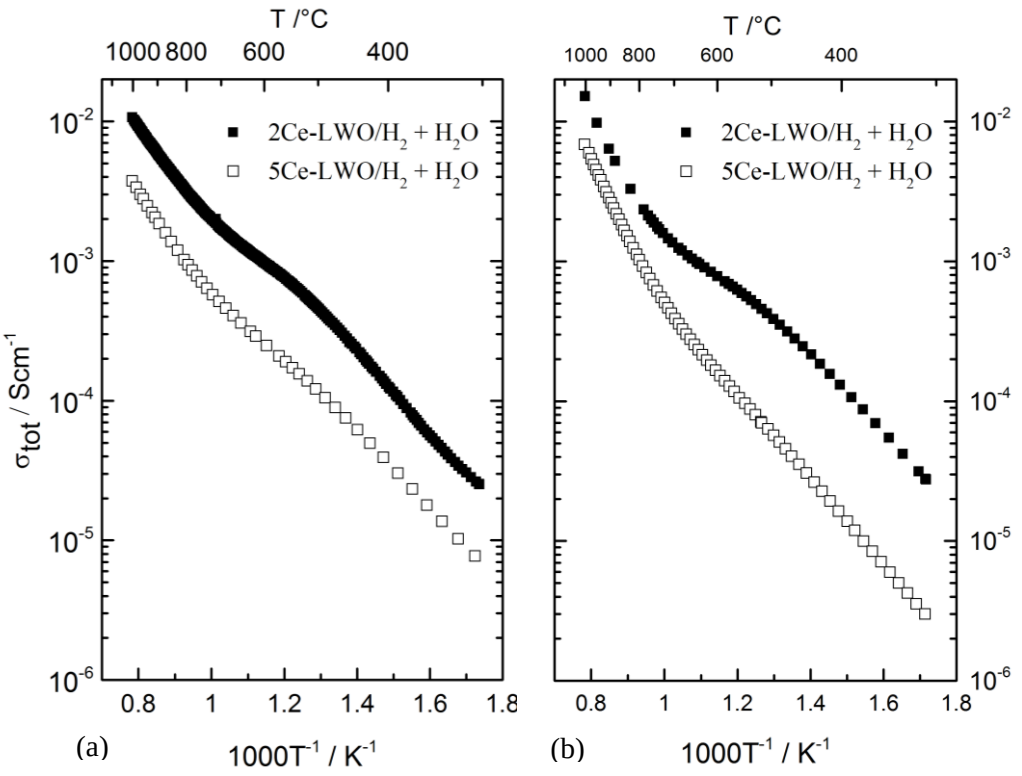

Figure 5.12. The total conductivity as a function of temperature for 2Ce-LaWO and 5Ce-LaWO under O_2 + 2.5% H_2O (a) and under H_2 + 2.5% H_2O.

5.2.2 p_{O_2} Dependency of the conductivity

The oxygen partial pressure dependency of the conductivity can give further insight into the defects contribution to the total conductivity. Figure 5.13 shows the total conductivity as a function of p_{O_2} at different temperatures for 2Ce-LWO and 5Ce-LWO. The measurements were performed at 10 kHz in wet atmospheres and constant water partial pressure (p_{H_2O} = 0.025 atm). After the measurements were completed (Measurement 1), additional measurements were taken (Measurement 2) to check reproducibility.

From the Figure 5.13(a) it can be seen that the measurements of 2Ce-LaWO are quite reproducible at 1000 °C and less reproducible at lower temperatures. Figure 5.13(b) shows the same measurements for 5Ce-LWO. It can be observed that the points from Measurement 2 for this sample are not reproducible. The reason for irreproducible points can be some changes that occurred with the sample composition at 1100 °C (e.g. cation diffusion can occur at these temperatures).

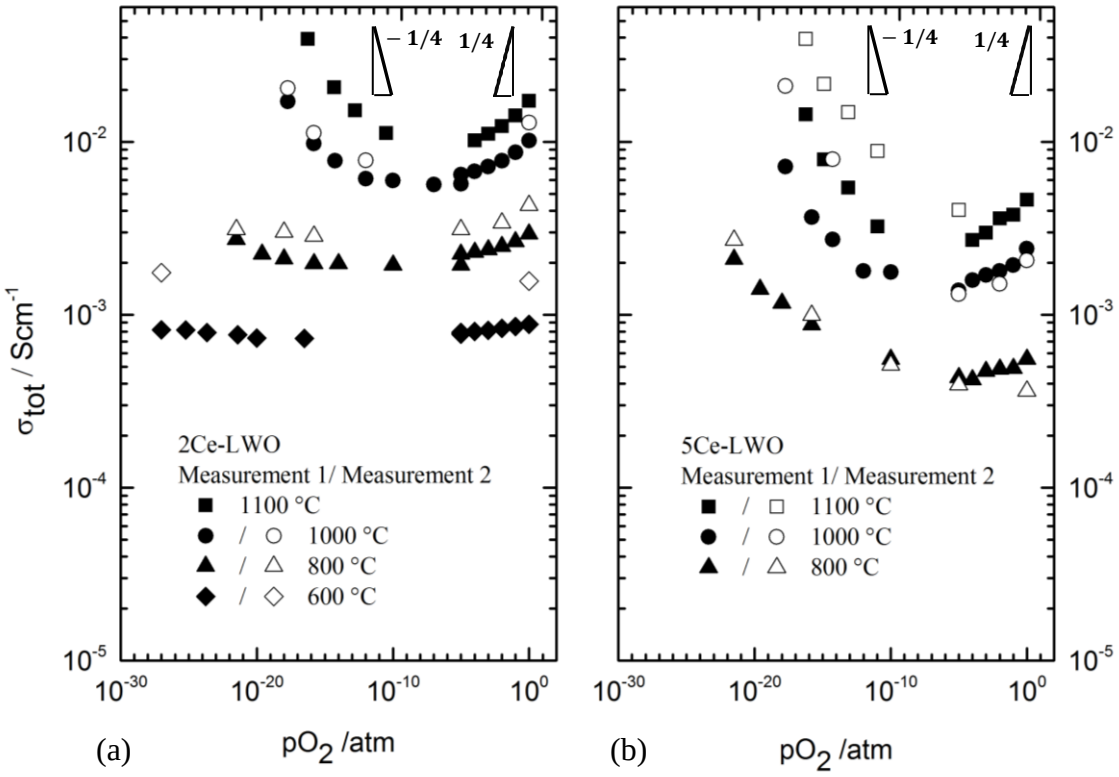

Figure 5.13. The total conductivity of 2Ce-LWO (a) and 5Ce-LWO (b) as a function of oxygen partial pressure at different temperatures from 600 °C to 1000 °C: Measuremt 1 versus Measurement 2.

For both samples the conductivity increases with increasing p_{O_2} under oxidizing conditions, and increases with decreasing p_{O_2} under reducing conditions. The conductivity has generally steeper dependency under reducing conditions at higher temperatures.

Figure 5.14 compares the total conductivity measurements as a function of p_{O_2} for 2Ce-LWO and 5Ce-LWO at 1100 °C, 1000 °C and 800 °C. The total conductivity is significantly lower for 5Ce-LWO and the relative contribution from electrons increases with increasing Ce content. Under oxidizing condition the slopes for two samples are similar, indicating that p-type conductivity is not significantly affected by Ce-doping. The increased n-type electronic conductivity may be explained by an increased donor doping concentration.

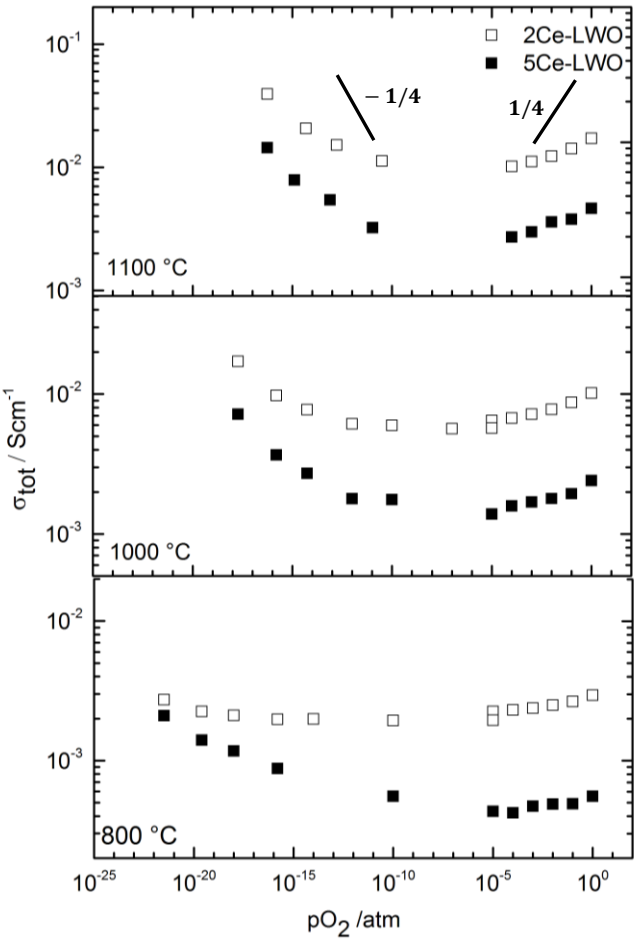

Figure 5.14. The total conductivity of 2Ce-LWO and 5Ce-LWO as a function of oxygen partial pressure at 1100 °C, 1000 °C and 800 °C.

5.2.3 p_{H_2O} dependency of the conductivity

The water vapor pressure dependency of the total conductivity under reducing and oxidizing conditions from 400 °C to 1000 °C for 2Ce-LWO is shown in Figure 5.15. The conductivities increase with increasing water vapor pressure and increasing temperature. At higher temperatures the conductivities are weekly dependent of p_{H_2O}. The difference between the conductivities in wet hydrogen and wet oxygen at 400 °C can be explained by slow equilibrium at low temperatures.

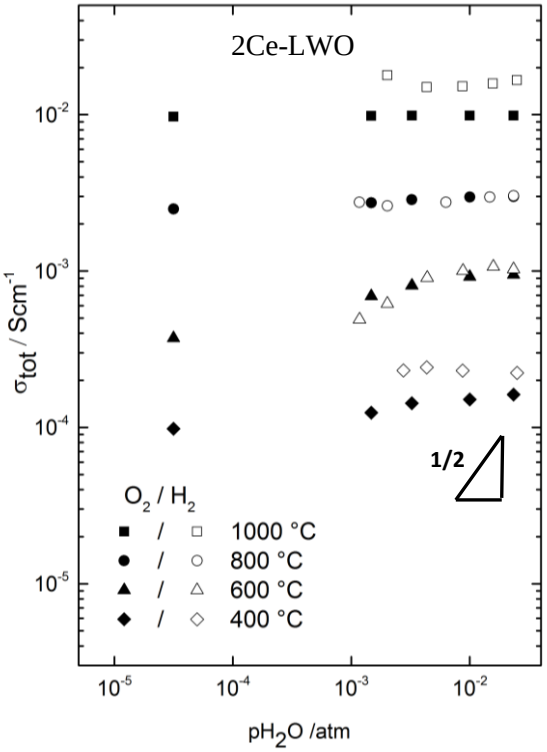

Figure 5.15. The total conductivity as a function of water partial pressure under O_2 + 2.5% H_2O and under H_2 + 2.5% H_2O at different temperatures from 400 °C to 1000 °C for 2Ce-LWO.

Figure 5.16 presents the p_{H_2O} dependencies in wet oxygen for 2Ce-LWO and 5Ce-LWO.

As mentioned earlier, the conductivity of 5% Ce - doped LWO54 is generally lower than that of 2 % Ce - doped LWO54. This can be explained by the reduction in the amount of oxygen vacancies that hydrate under wet conditions.

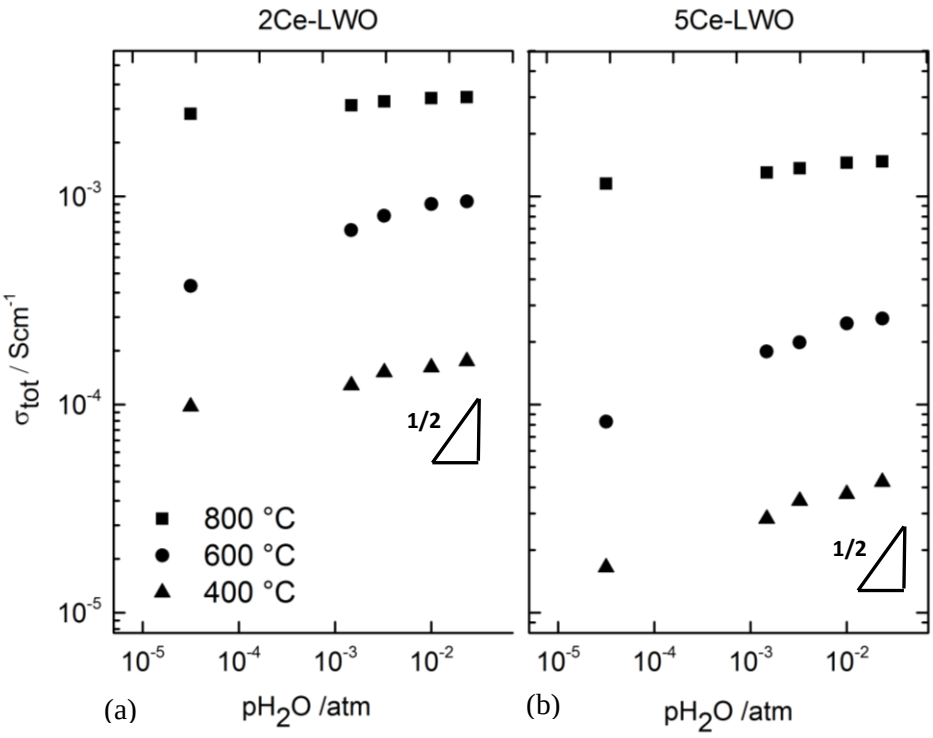

Figure 5.16. The total conductivity as a function of water partial pressure under O_2 + 2.5% H_2O at 800 °C, 600 °C and 400 °C for 2Ce-LWO (a) and 5Ce-LWO (b).

5.2.4 Impedance measurements

The impedance spectra was recorded for both 2Ce-LWO and 5Ce-LWO in the temperature range between 300 °C and 1000 °C under oxidizing and reducing conditions. Figure 5.17 shows the impedance sweeps for 2Ce-LWO (a,b) and 5Ce-LWO (c,d) at 300 °C, 350 °C, 400 °C and the corresponding frequency 10 kHz for each sweep, measured under equilibrium condition at wet oxygen (a,c) and wet hydrogen (b,d). The impedance spectra were deconvoluted using the program Equivalent Circuit, EQC [36], and the Brick-layer model (see subsection 2.5.4) was applied to calculate the conductivities of the bulk and grain boundary.

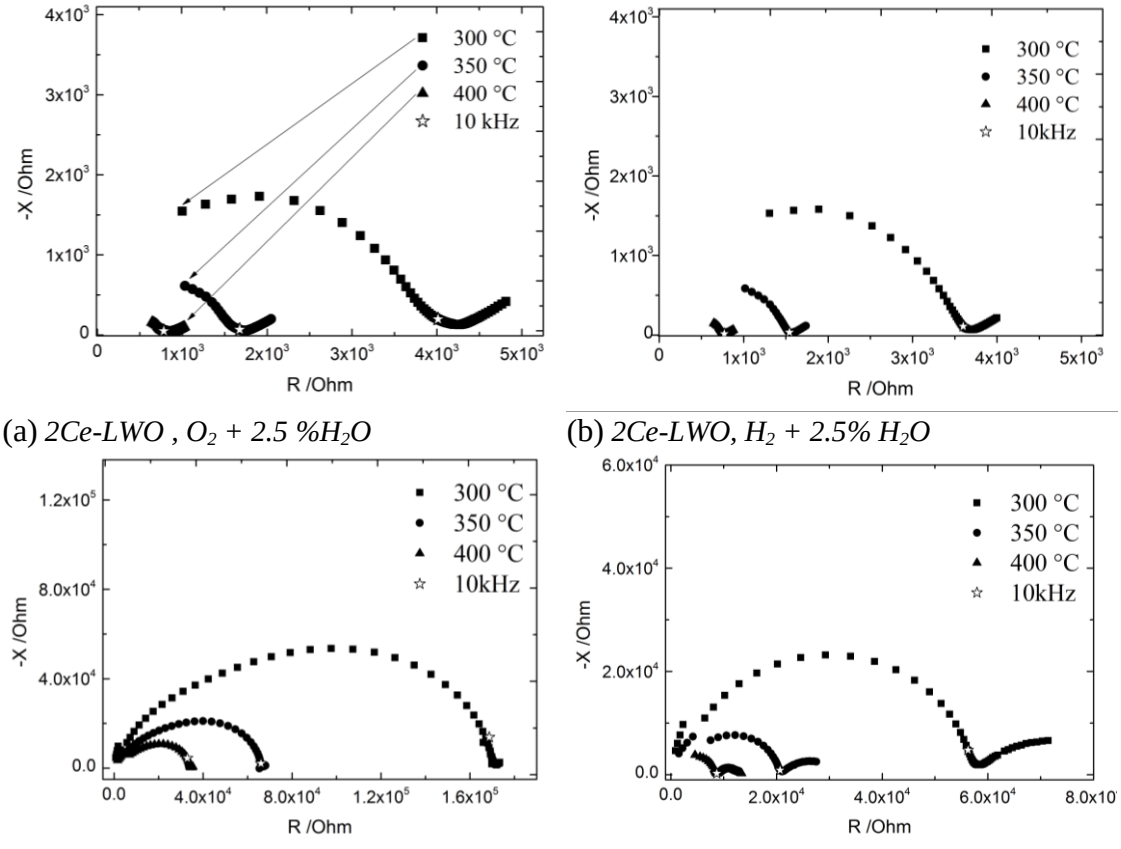

(a) *2Ce-LWO , O_2 + 2.5 %H_2O* (b) *2Ce-LWO, H_2 + 2.5% H_2O*

(c) *5Ce-LWO , O_2 + 2.5% H_2O* (d) *5Ce-LWO, H_2 + 2.5% H_2O*

Figure 5.17. Nyquist plots of 2Ce-LWO under O_2 + 2.5% H_2O (a) 2Ce-LWO under H_2 + 2.5% H_2O (b) 5Ce-LWO under O_2 + 2.5% H_2O(c) 5Ce-LWO under H_2 + 2.5% H_2O (d).

The spectra from wet oxygen for 2Ce-LWO (Figure 5.17(a)) consist of two semicircles at high frequency, corresponding to bulk and grain, and a smaller one at lower frequency, corresponding to electrodes. The spectra in wet hydrogen (Figure 5.17(b)) show only one semicircle at high frequency. A similar behavior is observed for 5Ce-LWO. The grain boundary contribution is more visible for 5Ce-LWO compared to 2Ce-LWO.

The deconvolution shows that there is a contribution from both grain interior and grain boundary under wet oxygen and no grain boundary contribution under wet hydrogen for both samples.

Table 5.7 presents the results from deconvolution of the impedance spectra at 300 °C.

Table 5.7. Results from the deconvolution of the impedance spectra of 2Ce-LWO (a,b) and 5Ce-LWO (c,d) at 300 °C under oxidizing (a,c) and reducing (b,d) conditions.

(a)			
2Ce-LWO , O_2 + H_2O, 300 °C	***C /F***	***G /S***	***σ /Scm^{-1}***
Grain interior	3,83E-11	2,70E-04	5,09E-05
Grain boundary	6,99E-09	8,05E-06	1,51E-06
(b)			
2Ce-LWO , H_2 + H_2O, 300 °C	***C /F***	***G /S***	***σ /Scm^{-1}***
Grain interior	1,30E-11	2,11E-04	3,98E-05
Grain boundary	-	-	-
(c)			
5Ce-LWO , O_2 + H_2O, 300 °C	***C /F***	***G /S***	***σ /Scm^{-1}***
Grain interior	2,76E-11	1,42E-05	3,57E-06
Grain boundary	1,47E-10	1,80E-06	4,52E-07
(d)			
5Ce-LWO , H_2 + H_2O, 300 °C	***C /F***	***G /S***	***σ /Scm^{-1}***
Grain interior	1,78E-11	1,79E-05	4,49E-06
Grain boundary	-	-	-

Under oxidizing conditions the conductivity of grain boundary for 5Ce-LWO is lower than for 2Ce-LWO, indicating that the grain boundaries are also more resistive with increasing Ce content.

5.3 Thermogravimetric characterization

2Ce-LWO was investigated by Thermogravimetric measurements (TG) where the relative weight change is monitored as a function of temperature. The measurements were done as a function of temperature under isobaric conditions in different atmospheres. Figure 5.18(a) presents the relative weight change in wet oxygen as a function of time at different temperatures. The measurements were corrected for appropriate background.

The weight gain is caused by the water vapor uptake in 2Ce-LWO, which increases with lower temperature. The water vapor causes the hydration of oxygen vacancies to form protons as described by Equation 2.41. Figure 5.18(b) shows the concentration of moles of proton per mole of 2Ce-LWO as a function of reciprocal temperature.

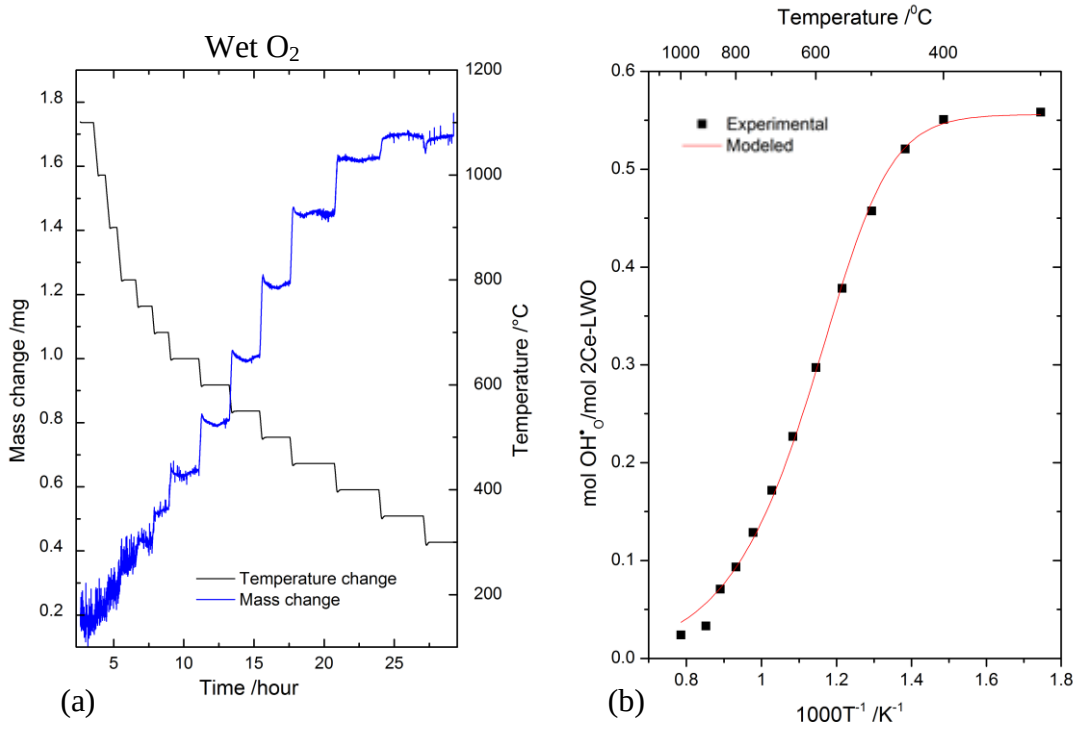

Figure 5.18. The weight change under O_2 + 2.5% H_2O (left y-axis) in response to the stepwise temperature decrease from 1000 °C to 300 °C (right y-axis) (a), and the proton concentration of 2Ce-LWO as a function of reciprocal temperature (b).

To investigate whether the weight uptake is caused only by hydration or an oxidation of the oxygen vacancies, the thermogravimetric measurements were carried out in wet Ar. In this atmosphere, the oxygen vapor partial pressure is much lower (10^{-5} atm)

than in O_2 (1 atm), so if oxygen gas uptake occurs, different weight uptake will be observed.

Figure 5.19(a) shows the relative weight change in wet Ar as a function of time, which was not corrected to the background. In order to reach equilibrium at low temperatures, the isothermal annealing was prolonged, and thus, the background could not be subtracted due to difference in temperature program. The correction was done manually later to calculate of proton concentration, and Figure 5.19(b) shows the corrected data.

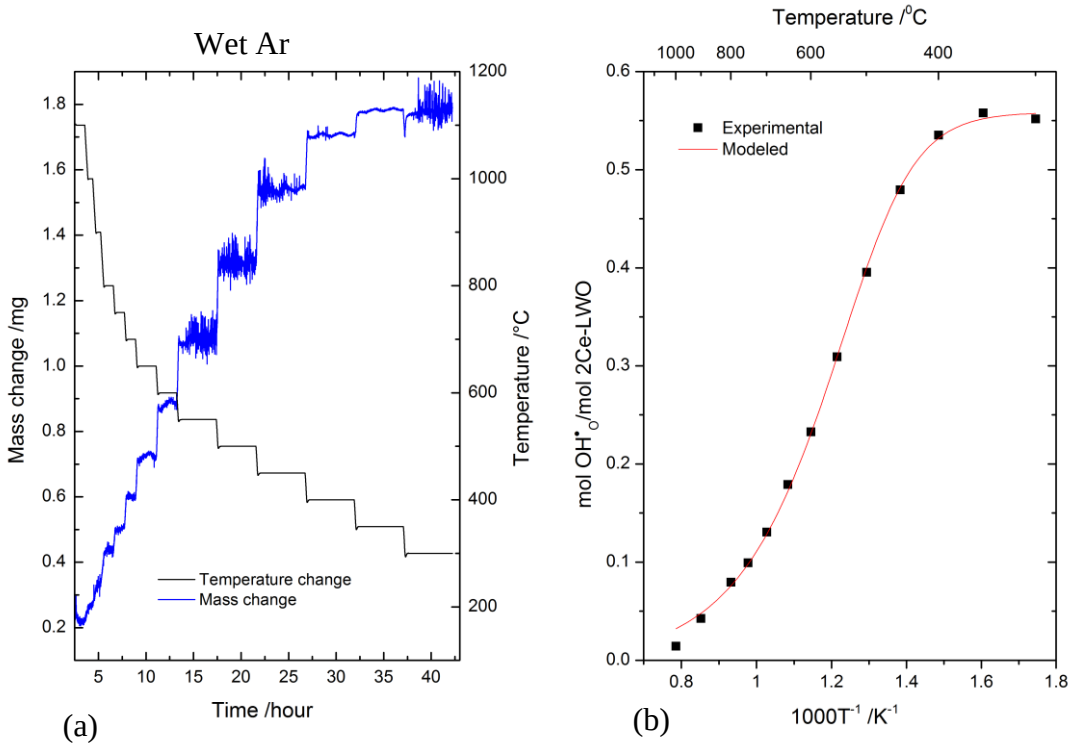

Figure 5.19. The weight change under Ar + 2.5% H_2O (left y-axis) in response to the stepwise temperature decrease from 1000 °C to 300 °C (right y-axis) (a), and the proton concentration of 2Ce-LWO as a function of reciprocal temperature (b).

Figure 5.20 shows the experimental (a) and modeled (b) concentration of protons per mole of 2Ce-LWO in wet Ar and wet O_2. It is clear that the curves are quite comparable with an acceptor level (see Appendix A1) equal for both plots ($[Acc^{/}] = 0.52$). The small difference in the temperature dependence between wet Ar and wet oxygen may be explained by the different ways of background correction. On these

bases one may conclude that the majority of the weight gain observed corresponds to hydration of the materials.

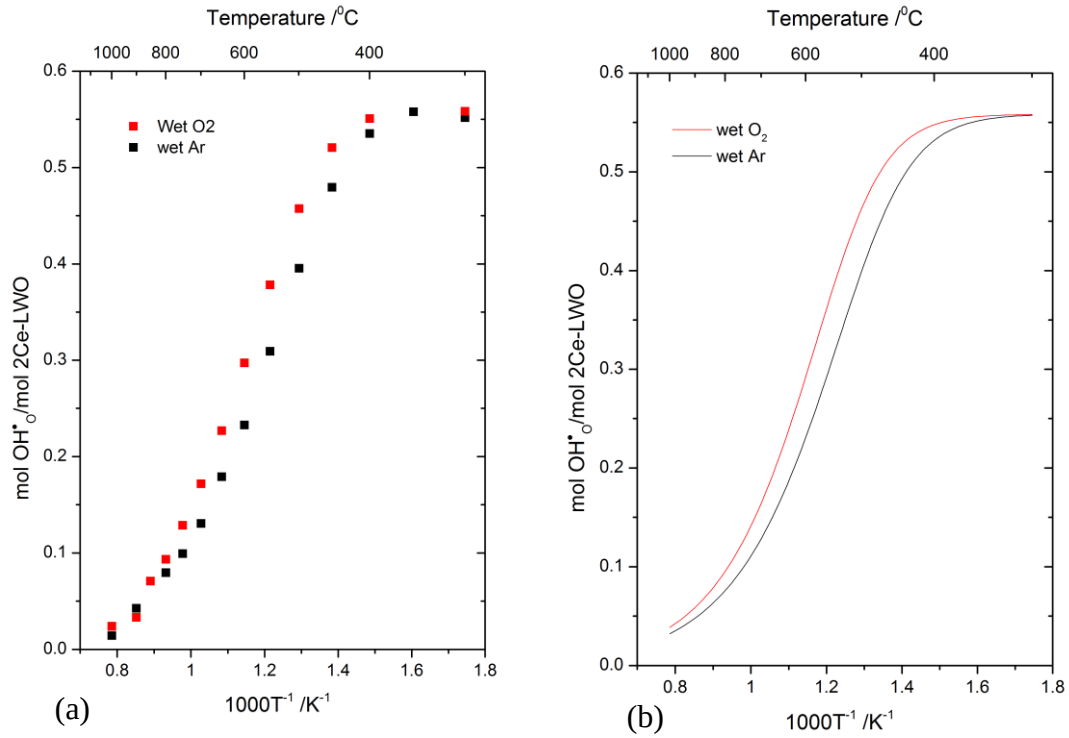

Figure 5.20. The experimental (a) and modeled (b) proton concentration of 2Ce-LWO as a function of reciprocal temperature under O_2 and Ar+ 2.5% H_2O.

The measurements were also performed in dry atmospheres. Figure 5.21 shows the relative weight change as a function of temperature in dry oxygen and dry argon respectively. There is no weight change occurring at high temperatures, which support that there is no oxidation of oxygen vacancies. There is a small weight change only at temperatures below 500 °C. The reason for this may be that the nominally dry gas still contains some water vapor.

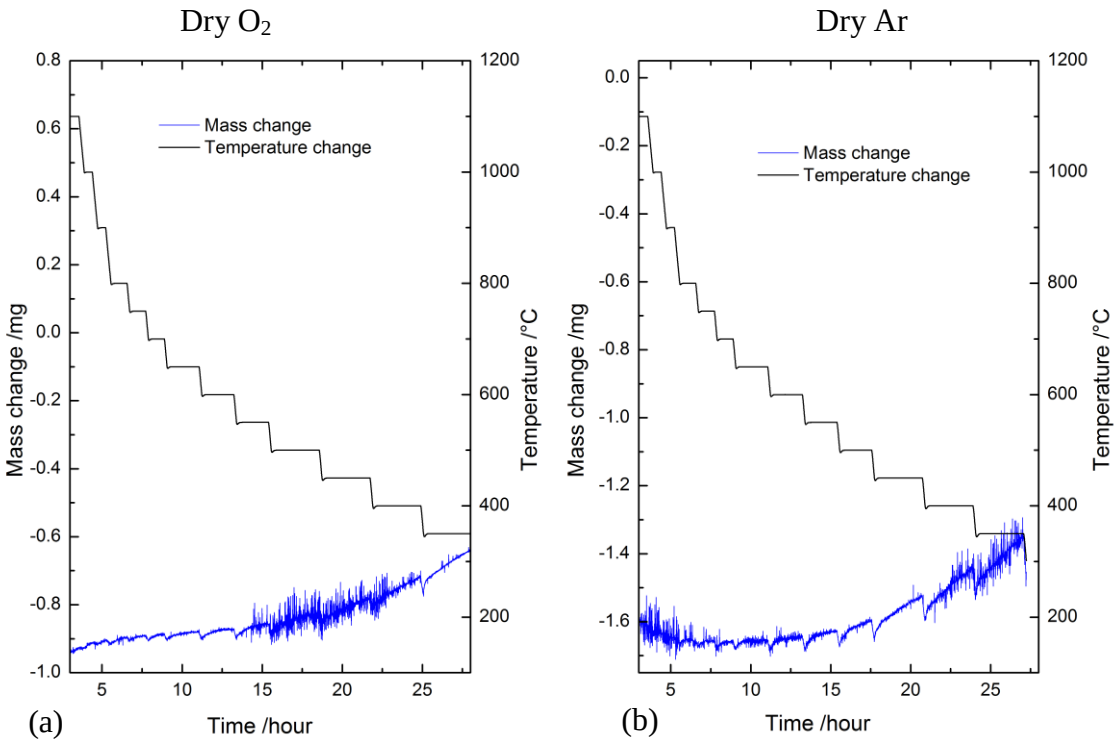

Figure 5.21. The relative weight change under O_2 + 30ppm H_2O (a) and Ar + 30ppm H_2O (b) in response to the stepwise temperature decrease from 1000 °C to 300 °.

6 Discussion

This part contains interpretations of the experimental results presented in chapter 5. The main discussion will be based on the results obtained by the electrical conductivity and TG- measurements in comparison to undoped LWO. The results from sample characterization will be also used to support the defect structure of 2Ce-LWO and 5Ce-LWO. At the end, the thermodynamic and transport parameters, extracted from the total conductivity and TG – measurements will be presented and discussed.

6.1 Defect structure

All the observed total conductivity dependencies of 2Ce-LWO and 5Ce-LWO will be explained with respect to the Brower diagrams given in subsection 2.3 and the full electroneutrality condition:

$$\mathrm{n} + \left[Acc'\right] = \frac{108}{56}\left[V_{\frac{54}{56}O}^{\frac{108}{56}\bullet}\right] + \frac{52}{56}\left[OH_{\frac{54}{56}O}^{\frac{52}{56}\bullet}\right] + p \tag{6.1}$$

where $\left[Acc'\right]$ is the concentration of the acceptor in the sample. For Ce-doped LWO this concentration equals to the concentration of the dopants and oxygen ions:

$$\left[Acc'\right] = \frac{4}{56}\left[O_{\frac{54}{56}O}^{\frac{4}{56}\prime}\right] + 3[W_{La}^{\bullet\bullet\bullet}] + [Ce_{La}^{\bullet}] \tag{6.2}$$

The material shows the typical behavior of a mixed ionic-electronic conductor, as observed from the p_{O_2} dependencies (Figures 5.13, 5.14). The conductivity of both samples increases with increasing p_{O_2} under oxidizing conditions, and increases with decreasing p_{O_2} under reducing conditions. Electrons and electron holes, which act as a minority defects, dominate the conductivity at low and high p_{O_2} respectivley at the temperatures above ~800 °C due to the high mobility of electronic defects. The total conductivity of both materials approaches $p_{O_2}^{-1/4}$ dependency under reducing

conditions, corresponding to the left part of the stoichiometric region of the Brower diagram in Figure 2.4 $\left(\frac{108}{56}\left[V_{\frac{54}{56}O}^{\frac{108}{56}\bullet}\right] = n + \frac{4}{56}\left[O_{\frac{54}{56}O}^{\frac{4}{56}/}\right]\right)$ and reflecting the n-type electronic conductivity. The total conductivity approaches $p_{O_2}^{1/4}$ dependency under oxidizing atmosphere corresponding to the right part of the stoichiometric region of the Brower diagram $\left(\frac{108}{56}\left[V_{\frac{54}{56}O}^{\frac{108}{56}\bullet}\right] = p + \frac{4}{56}\left[O_{\frac{54}{56}O}^{\frac{4}{56}/}\right]\right)$ and reflecting the p-type electonic conductivity at high temperatures. Below 900 °C, the contribution of electronic conductivity decreases due to lower mobility of electrons and electron holes, and the total conductivity is predominated by ionic charge carrier for both samples.

The total conductivity is slighly dependent of p_{H_2O} at 800 °C, as shown in Figure 5.16, indicating an unfavourable hydration at this temprature and reflecting that the total conductivity is predominated by the oxygen ions. Upon decreasing the temperature below 800 °C, the conductivity becomes more dependent on p_{H_2O}, reflecting that the oxygen vacancies hydrate, that protons form and contribute to the total conductivity. At the temperatures below 800 °C with low water partial pressure $\left(\left[Acc^{/}\right] = \frac{108}{56}\left[V_{\frac{54}{56}O}^{\frac{108}{56}\bullet}\right]\right)$ the protonic defects are minority defects and the total conductivity predominated by the oxygen ions. As p_{H_2O} increases the total conductivity increases, reflecting a transition from dry condition to wet conditions $\left(\left[Acc^{/}\right] = \frac{52}{56}\left[OH_{\frac{54}{56}O}^{\frac{52}{56}\bullet}\right]\right)$, where the protonic defects predominate. At temperatures below 800 °C the dependency is close to $p_{H_2O}^{1/2}$, which corresponds to the Brower diagram (Figure 2.3). These dependencies are in agreement with the TG measurements (Figures 5.18-5.19).

The total conductivity measurements of both samples as a function of temperature in different atmospheres indicate clearly the protonic and electronic contributions (Figures 5.9, 5.11). The protonic contribution was proved by the H/D isotope effect and difference in the total conductivity under wet and dry atmospheres below 800 °C (Figures 5.9, 5.10), which corresponds to the results from water vapor dependency

discussed above. The electronic contribution was proved by the electrical measurements of the total conductivity at hydrogen, argon and oxygen (Figure 5.10).

The different relation between electronic and ionic conductivities in wet reducing and oxidizing atmospheres in the temperature range between 600 and 800°C that presented in Figure 5.9(b), indicates different contribution of oxygen ions and electronic defects to the total conductivity.

6.2 Effect of donor doping

The measured dependencies of both 2Ce-LWO and 5Ce-LWO show decreasing in the total conductivity compared to undoped LWO54. The conductivity decreases with increaing level of donor dopant. This may be caused by decreasing in the oxygen vacancies upon donor substitution as was expected and discussed in subsection 1.4.

In Figure 6.1 the oxygen partial pressure of the total conductivity of 2Ce-LWO is compared to that of undoped LWO54 and LWO53 from 1100 to 800 °C. The ionic conductivity of 2Ce-LWO is lower than that of LWO54 at all presented temperatures, and the difference increases with decreasing temperature. The decrease in the ionic conductvity can be explained by lower concentration of oxygen vacancies, which was expected from defect chemistry (Equation 1.1). The decrease in the concentration of oxygen vacancies can be supported by comparing the p_{O_2}dependency of 2Ce-LWO with LWO53, which has less oxygen vacancies in its structure (0.38 versus 0.5 at LWO54) (Figure 6.3).

The decrease in the ionic conductivity with higher level of the donor dopant is clearly seen in Figure 6.2. This proves the expectations about that the positive defect, created by donor doping, will be compensated by consumption of the positive oxygen vacancies. The decrease of the oxygen vacancies for 5Ce-LWO is larger than that for 2Ce-LWO and it can be seen by comparing the p_{O_2} dependency of 5Ce-LWO with LWO52 (0.26 vacancies) as presented in Figure 6.2(b).

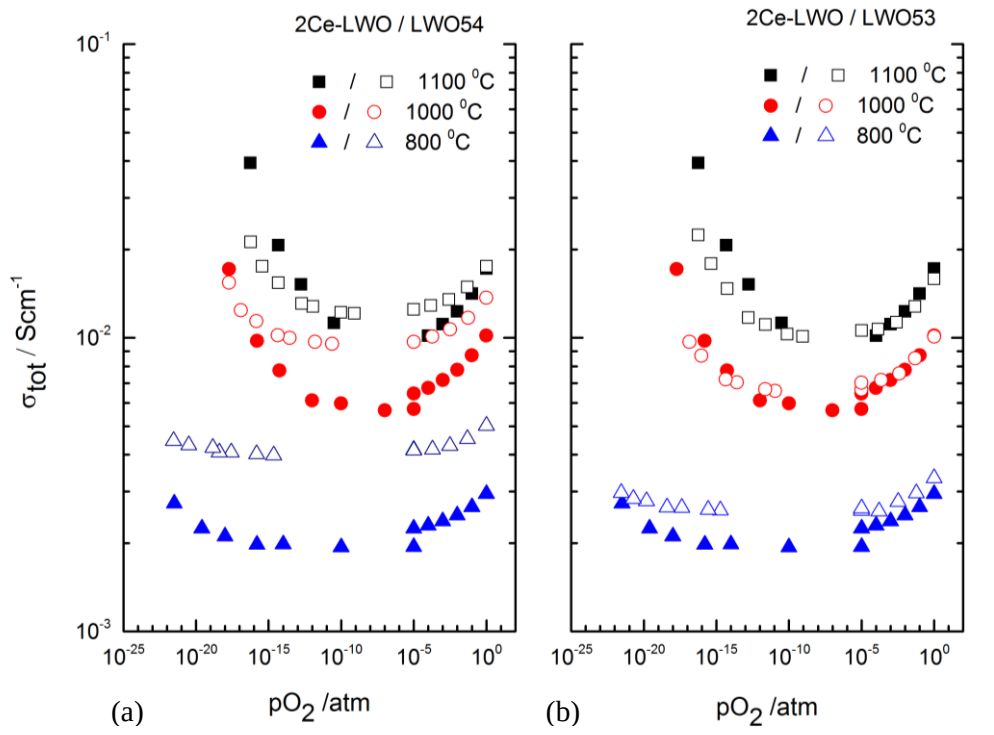

Figure 6.1. The total conductivity of 2Ce-LWO as a functionf of oxygen partial pressure at different temperatures from 600 °C to 1000 °C versus the total concutivity of LWO54 (a) and LWO53(b).

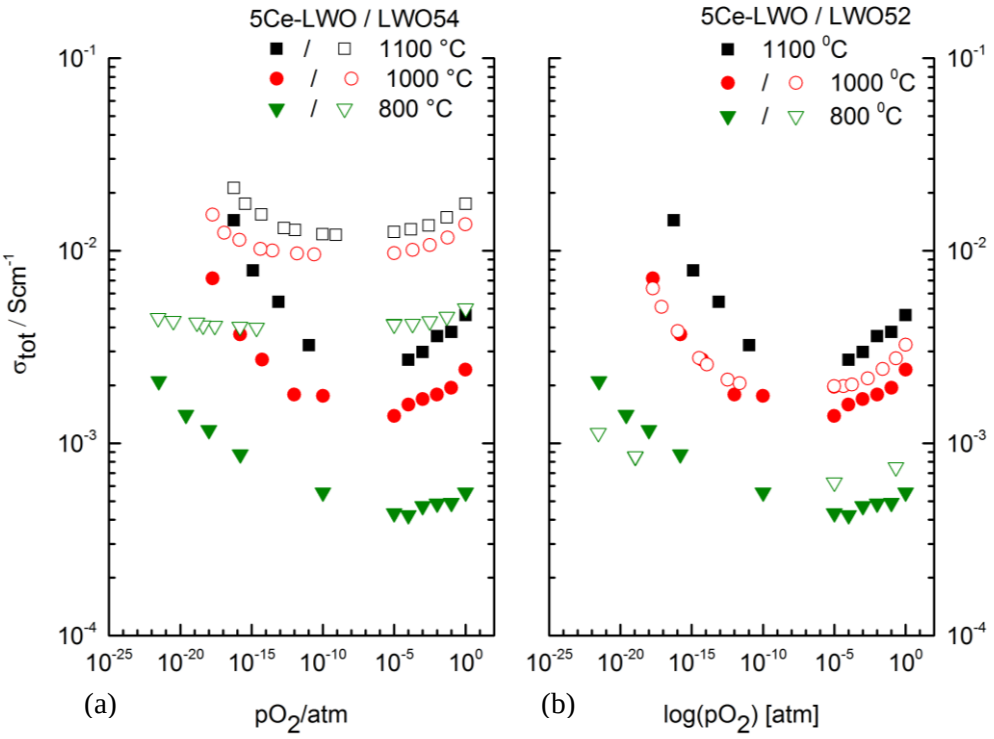

Figure 6.2. The total conductivity of 5Ce-LWO as a functionf of oxygen partial pressure at different temperatures from 600 °C to 1000 °C versus the total concutivity of LWO53 (a) and LWO52(b).

The decrease in the ionic conductivity for both samples accompanied with the increase in p_{O_2} dependency under reducing conditions at high temperatures, thus indicate the increase in n-type electronic conductivity, which is mainly resulting from the high mobility of electrons and increased concentration of the electronic species due to donor doping. The contribution of the electrons increases with Ce content, which proves the expectations about higher donor doping concentration. Another contribution to the increased n-type electronic conductivity at high temperatures may be resulted from the reduction of Ce^{4+} to Ce^{3+} under reducing conditions [40].

Figure 6.3 accompanies earlier findings about decreasing amount of oxygen vacancies to that of LWO53 ($La_{25.92}W_{5.08}O_{55.62}v_{0.38}$). The water vapor dependencies at 400 and 500 °C for 2Ce-LWO are quite uncertain due to low equilibrium at these temperatures. Nevertheless, at 600 and 800 °C the dependency is similar to that of LWO53, indicating similar amount of oxygen vacancies that hydrate.

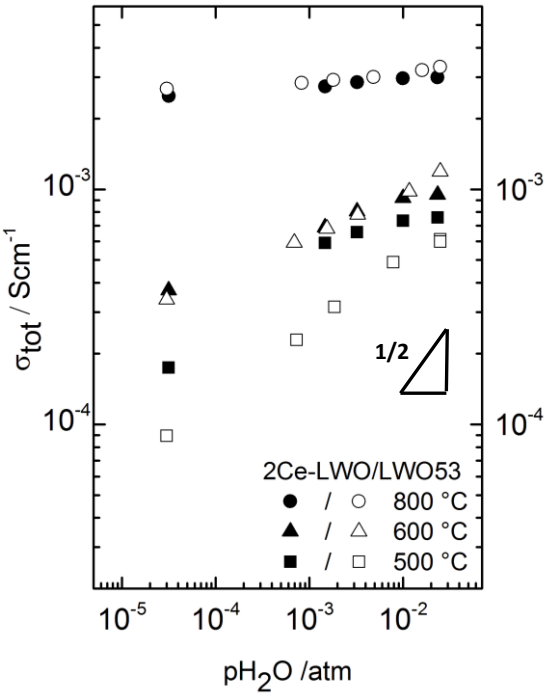

Figure 6.3. The total conductivity as a function of water partial pressure under O_2 + 2.5% H_2O at different temperatures for 2Ce-LWO versus LWO53.

Impedance spectroscopy measurements show contributions from grain boundaries under oxidizing conditions (Figure 5.17). The contribution increases with increasing level of donor content, which reflects the influence of Ce on the grain boundary. Both

grain interior and grain boundary conductivities decrease with increasing level of donor dopant (Table 5.7). The reason for this may be a potential barrier inherently at the grain boundaries, which impede the transport of oxygen ions and protons across them. Earlier studies of donor doped ceria [29, 41] and yttrium doped $BaZrO_3$ [28] applied a space charge theory to the grain boundary impedance and revealed a positive excess charge at the grain boundary core.

The absence of grain boundary semicircles on the impedance spectra of 2Ce-LWO and 5Ce-LWO under reducing conditions can be explained by either depletion of effectively positive defects at the grain boundary by decrease in the concentration of these defects or by accumulation of negatively charged defects. However, this thesis did not imply to study the effect of donor doping of LWO54 on grain boundary behavior, thus, due to lack of information, the origin of the grain boundary conductivity has not been fully addressed.

Figure 6.4 presents the grain interior conductivities of 2Ce-LWO and 5Ce-LWO which correspond essentially to its appropriate temperature dependencies under reducing conditions. The slightly shift between them may be due to changes in the chemical composition, since these measurements were performed with some time interval.

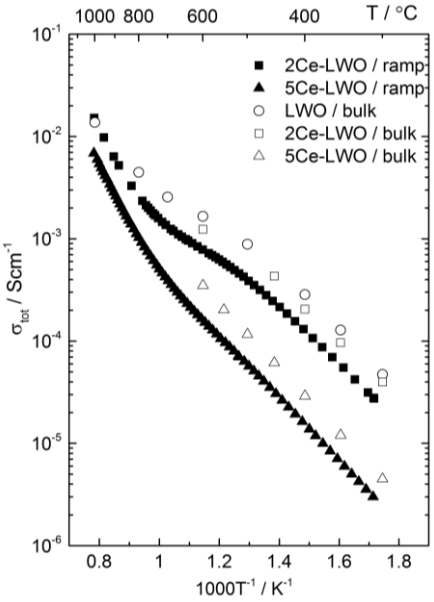

Figure 6.4. The grain interior conductivity of 2Ce-LWO and 5Ce-LWO versus appropriate total temperature dependencies and the grain interior conductivity of undoped LWO54 under reducing conditions.

6.3 Curve fitting

The curve fittings were performed with the program TableCurve2D [42]. The data from the thermogravimetric analysis was first used to estimate the enthalpy and entropy of hydration. The equilibrium constant from the hydration reaction (Equation 2.38) was combined with an Expression 2.22 to express the protonic concentration as a function of temperature. The enthalpy and entropy of hydration were then extracted. The experimental and modeled concentrations of moles protons per mole of 2Ce-LWO as a function of reciprocal absolute temperature were shown in Figure 5.18(b) for wet oxygen and Figure 5.19(b) for wet argon. The thermodynamic parameters derived from fitting of these data are presented in Table 6.1.

Table 6.1. Thermodynamic parameters extracted from the curve fitting of the thermogravimetric measurements of 2Ce-LaWO.

	ΔS_{hydr} , J/mol K	ΔH_{hydr}, kJ/mol	$[Acc']$
Wet O_2	-129	-109	0.52
Wet Ar	-127	-102	0.52

Without any transient measurements, fitting of the thermogravimetric data only gives the thermodynamic parameters of the hydration reaction. However, these parameters are important to find, since they express only one process and hence don't include much uncertainties. The thermodynamic parameters were used to estimate the transport properties by fitting the total conductivities as a function of temperature.

The curve fitting was performed for the temperature dependencies, which were measured at temperature range from 1000 to 300 °C under reducing and oxidizing conditions for 2Ce-LaWO and 5Ce-LWO. The electroneutrality condition (Equation 2.42) in combination with the hydration reaction (Equation 2.38) and expression for the partial conductivity (Equation 2.49) were used to model the total conductivity as a function of inverse temperature (Appendix A8). In order to estimate the transport parameters of electrons and electron holes, the electronic conductivities were extracted from p_{O_2} dependencies at high temperatures (Figure 5.13).

The concentration of electrons and electron holes in correspondingly wet hydrogen and wet oxygen were calculated using Equation 2.12 and Equation 2.15. The standard

state of electrons and holes is not defined in LWO. A model of a small polaron, which was used to estimate these values in $BaPrO_3$ [43] was reviewed relative to LWO oxide. $BaPrO_3$ is a perovskite oxide with p-type dominating conductivity in the temperature range 1100 to 200 °C and defining the standard density of state of electrons and electron holes was a critical step on the way of fitting the conductivity. However, LWO is a mixed ionic-electronic conductor [9, 12, 15] and it is estimated that for stoichiometric condition the only dominating defects are the positive oxygen vacancies and negative oxygen ions. Therefore, the standard state of electrons and electron holes is neglected here. The concentration of the electrons is inversely proportional to the concentration of the oxygen vacancies and the proportional to $p_{O_2}^{-1/4}$ (Appendix A5). The oxygen partial pressure is temperature dependent under reducing conditions. The p_{O_2} dependency as a function of temperature at reducing atmosphere was estimated by a linear fit at Origin 8.6 program [44]. The concentration of electron holes is inverse proportional to the concentration of oxygen vacancies and $p_{O_2}^{1/4}$ (Appendix A6). The oxygen partial pressure is constant and equal 1atm through the whole temperature range under oxidizing conditions. Figure 6.5 and Figure 6.6 show the measured total conductivity and modeled partial conductivities for protons, oxygen ions, electrons (a) and electron holes (b) as a function of reciprocal temperature for 2Ce-LaWO and 5Ce-LWO, respectively. Tables 6.2 and 6.3 show the corresponding thermodynamic and transport parameters from the curve fitting for 2Ce-LWO and 5Ce-LWO respectively.

Both 2Ce-LWO and 5Ce-LWO showed that protonic conductivity dominated below ~800 °C. At this temperature the protonic conductivity was 1×10^{-3} S/cm and 1.33×10^{-3} S/cm for 2Ce-LWO respectively under wet hydrogen and wet oxygen. For 5Ce-LWO the values were one order of magnitude lower of 2.68×10^{-4} S/cm and 3.52×10^{-4} S/cm under wet hydrogen and wet oxygen respectively. At the temperatures above 800 °C, electrons take over under reducing conditions; while under oxidizing conditions oxygen ions and electron holes predominate almost equally.

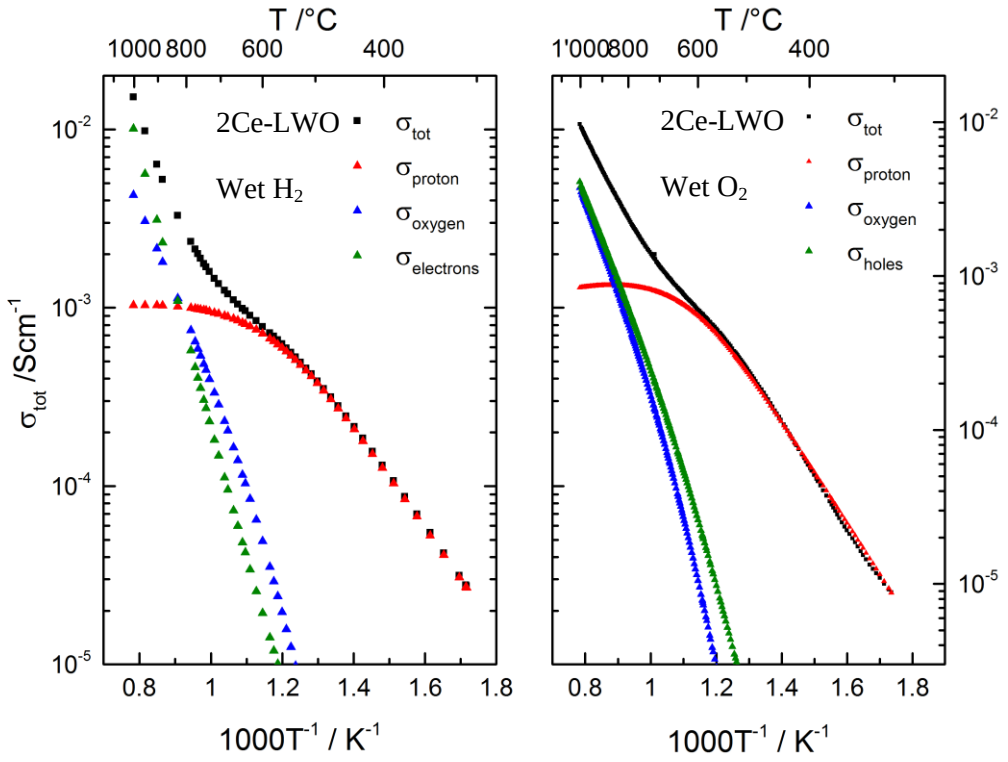

Figure 6.5. Measured total conductivity and customized partial conductivities as a function of inverse absolute temperature for 2Ce-LWO with the temperature interval 1000-300 °C at reducing (to the left) and oxidizing (to the right) conditions.

Table 6.2. Extracted transport parameters from curve fitting of the total measured conductivity as a function of inverse temperature for 2Ce-LWO with the temperature interval 1000-300 °C at reducing and oxidizing conditions.

Charge Carrier	Custom parameter	Value	Unit
$OH_O^{\bullet}$	ΔS^0_{hydr}	-122±2	J/molK
	ΔH^0_{hydr}	-105	kJ/mol
	$u^0_{OH_O^{\bullet}}$	22±7	cm^2K/Vs
	$\Delta H_{OH_O^{\bullet}}$	61±3	kJ/mol
$v_O^{\bullet\bullet}$	$u^0_{v_O^{\bullet\bullet}}$	380±250	cm^2K/Vs
	$\Delta H_{v_O^{\bullet\bullet}}$	90±10	kJ/mol
e′	$K^{1/2}_{red}u^0_{e/}$	3100±20	
	$E_{a,e'}$	163	kJ/mol
h•	$K^{1/2}_{ox}u^0_{h^{\bullet}}$	873	
	$E_{a,h^{\bullet}}$	94	kJ/mol

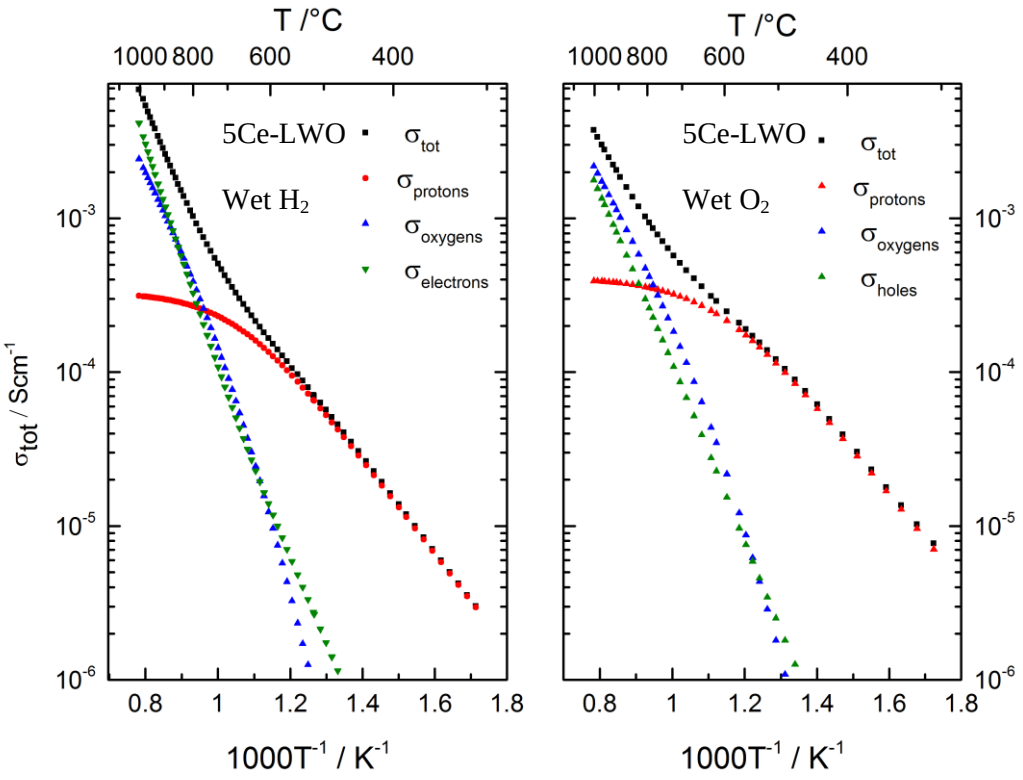

Figure 6.6. Measured total conductivity and customized partial conductivities as a function of inverse absolute temperature for 5Ce-LWO with the temperature interval 1000-300 °C at reducing (a) and oxidizing (b) conditions.

Table 6.3. Extracted transport parameters from curve fitting of the total measured conductivity as a function of inverse temperature for 5Ce-LWO with the temperature interval 1000-300 °C at reducing and oxidizing conditions.

Charge Carrier	Custom parameter	Value	Unit
$OH_O^{\bullet}$	ΔS^0_{hydr}	-118	J/molK
	ΔH^0_{hydr}	-106±3	kJ/mol
	$u^0_{OH_O^{\bullet}}$	60±3	cm^2K/Vs
	$\Delta H_{OH_O^{\bullet}}$	62±2	kJ/mol
$v_O^{\bullet\bullet}$	$u^0_{v_O^{\bullet\bullet}}$	1200±300	cm^2K/Vs
	$\Delta H_{v_O^{\bullet\bullet}}$	90±3	kJ/mol
e′	$K_{red}^{1/2}u^0_{e/}$	87000	
	$E_{a,e'}$	160	kJ/mol
h$^{\bullet}$	$K_{ox}^{1/2}u^0_{h^{\bullet}}$	1600	
	$E_{a,h^{\bullet}}$	111	kJ/mol

From the previous studies and reviews [43, 45], the standard hydration entropy, which corresponds to a loss of one gas molecule for chemical reaction is typically reported in the range -120±40 J/molK for rare earth oxides. The standard enthalpy change ΔH^0_{hydr} for the hydration reaction associates with dissolution of protons and consumption of oxygen vacancies at low temperature. The enthalpy of hydration is also associated with the stability of oxide. The studies in hydration of rare-earth oxides reported that ΔH^0_{hydr} becomes increasingly negative with increasing stability of the oxides [45].

The standard entropy of hydration, $\Delta S^0_{hydr,}$ of both 2Ce-LaWO and 5Ce-LaWO was in a range of -120 J/molK. This was in agreement with both the thermogravimetric results presented before (Table 6.1), previously published results in data modeling for LWO53/LWO57 (-125 J/molK [15]) and previous studies in hydration of LWO53/LWO56 (-115 J/molK [27]). The standard enthalpy of hydration, $\Delta H^0_{hydr,}$ was estimated to be -106 kJ/mol. This was more negative than that estimated for undoped LWO53/LWO57 (-83 kJ/mol [15]) and undoped LWO53/LWO56 (-90 kJ/mol [27]). From the previous statement about enthalpy of hydration, it can be speculated that donor doped LWO is more stable than undoped LWO. This can be also supported by the cubic lattice parameter, which is lower than that of undoped LWO54 (see subsection 5.1.1). Lower lattice parameter corresponds to a lower distortion from the cubic cell and hence higher stability, which may be ascribed to a lower concentration of oxygen vacancies [20].

The enthalpy of mobility of protons and oxide ions for both samples are estimated to be ~ 60 kJ/mol and ~ 90 ± 10 kJ/mol respectively, which is in agreement with reported results by Erdal et al [15] ($\Delta H_{OH_O^\bullet}$ ~ 60 kJ/mol, $\Delta H_{v_O^{\bullet\bullet}}$ ~ 85 kJ/mol) for undoped LWO53/LWO57. These results are also in agreement with the rule of thumb that the enthalpy of protonic mobility is 2/3 of the enthalpy of oxygen ions [46]. The activation energy of n-type electronic conductivity which contains both the enthalpy of formation and mobility of the charge carrier was estimated to be ~ 160 kJ/mol. This value is considerably lower than that was obtained for undoped LWO53/LWO57 (~275 kJ/mol [15]). The reason for this difference may be different modeling approaches of the transport parameters of electronic charge carries and/or different reduction processes compared to undoped LWO.

6.4 Phase composition

When choosing a dopant to study high temperature proton and mixed proton-electron conductors, as well as to study the material, the dopant should have similar ionic radii and chemical properties as those of the parent ion it substitutes. For La substitution in LWO cerium was shoosen as an appropriate donor dopant since its ionic radii is close to lanthanum for the same coordination number. When choosing this element, only La1 with a coordination number 8 was considered to be substituted, so the ionic radii of Ce^{4+} is close to $La1^{3+}$ ($r_{Ce^{4+}}$ = 0.97 Å, $r_{La1^{3+}}$ = 1.16 Å). However, LWO has also the La2 ions in the structure with coordination number 6.6 [17] and serium ion can be both Ce^{4+} and Ce^{3+} and have coordination numbers 6 (Ce^{4+}/ Ce^{3+}) and 7 (Ce^{3+}). The ionic radii of Ce^{4+} ion with the coordination number ~ 6 is also close to $La2^{3+}$ ions ($r_{Ce^{4+}} \sim$ 1.046 Å, $r_{Ce^{4+}} \sim$ 0.87 Å, $r_{La2^{3+}} \sim$ 1.073 Å [14]) and will be considered hereafter.

Upon donor substitution of LWO54 with Ce on La site, it was expected that Ce^{4+} substitutes La^{3+} ions without changing ratio between La and W sites, and the positive defect, created by donor doping, will be compensated by consumption of the positive oxygen vacancies and/or protons depending on conditions (Equation 1.1).

According to these expectations, 2% Ce-doping of $La_{27}W_5O_{55.5}v_{0.5}$ would decrease content of lanthanum to 26.46, changing the formula unit to $La_{26.46}Ce_{0.54}W_5O_{55.77}v_{0.23.}$ Refutation of these expectations was obtained by the calculation of unit cell of 5% Ce-doped LWO54. Calculated formula unit $La_{25.65}Ce_{1.35}W_5O_{56.175}$ contained more oxygen ions than the amount of oxygen sites in the structure, which contradicts the model of doped LWO. This reveals the failed assumptions about nature of donor substitution with Ce on La site.

Assuming that 2Ce-LWO fully hydrates in the presence of water vapor, it was concluded that there are 0.26 oxygen vacancies in the structure of 2% Ce – doped LWO54 on the basis of the thermogravimetric measurements (Figure 5.18-5.20).

The data from EPMA spot analysis was used to calculate the formula units of 2Ce-LWO and 5Ce-LWO. The measured composition of the main phase of both samples contained slightly more La and less W than expected nominally, while the composition of Ce of both samples was in agreement to expected values. The

(La+Ce)/W nominal ratio was estimated to be ~ 5.7 for 2%-doped LWO54 (Table 5.5) and ~ 6 for 5%-doped LWO54 (Table 5.6).

The obtained formula unit of 2Ce-LWO after the spot analysis was not unambitious. In order to calculate the formula unit, two approaches were used. The approach 1 was based on heavy elements and did not account oxygen content. The approach 2 accounted oxygen content. The calculations of the formula unit based on the approach 1 contained Ce^{4+} ions, and the amount of the oxygen vacancies in this unit cell was in agreement with the estimation from the thermogravimetric results: $La_{26.8}Ce_{0.54}W_{4.82}O_{55.74}v_{0.26}$.

The approach 2 contained $Ce^{3.15+}$: $La_{26.8}Ce_{0.54}W_{4.82}O_{55.51}v_{0.49}$. This formula unit did not fit the earlier results made after thermogravimetric analysis and therefore it was chosen not to trust the oxygen content from the EPMA spot analysis and hence approach 2 hereafter.

Calculating the unit cell of 5Ce-LWO was quite challenging, since no thermogravimetric data of this compound was presented. The approach of calculating the unit cell based on heavy elements and Ce^{4+} ions gave higher oxygen content than possible in $LWO/La_{28-x}W_{4+x}O_{54+1,5x}v_{2-1,5x}$ (see subsection 2.2): $La_{26.2}Ce_{1.55}W_{4.57}O_{56.11.}$ This may be explained by some uncertainties in the EPMA spot analysis or different charge of cerium ions than that was expected. With this purpose, the curve fitting approach was applied. In this approach the thermodynamic parameters estimated for 2Ce-LWO were used as constraint parameters during fitting of the conductivity for 5Ce-LWO. By adjusting the enthalpy and entropy of hydration this way, the level of oxygen vacancies could be estimated. Similar thermodynamic parameters and the enthalpy of mobility of 2%-and 5%-Ce doped LWO, provided the basis to rely on the estimated level of oxygen vacancies of *0.15* for 5Ce-LWO from the curve fitting. The calculated formula unit for 5Ce-LWO using this approach contained cerium ions with slightly lower charge ($Ce^{\cdot 3.8+}$) than was expected and estimated for 2Ce-LWO: $La_{26.2}Ce_{1.49}W_{4.57}O_{55.85v0.15.}$

The results of the EPMA spot analysis were not statistically proved and those may have uncertainties. The reason for this was discussed above in this section, which may be due to different volumes of the phase and x-ray collection. This may bring some uncertainties in the element content, and thus the calculations of the unit cell. There is

no reason to believe that cerium ion could appear with different charge than Ce^{4+}, since it was already proved for 2Ce-LWO.

EPMA spot analysis of 2Ce-LWO before the electrical measurements detected a formation of $La_6W_2O_{15}$ as a secondary phase (Table 5.4). This phase was clearly seen on the element mapping as a W rich phase (Figure 5.6). EPMA elemental mapping analysis of both samples after the electrical measurements also observed W rich areas (Figures 5.7(b) and 5.8(b)), the amount of which increased with increasing level of donor dopant. These phases appeared as bright spots on the BSE images of both samples, while the spot analysis of them detected quite similar amount of elements to the main phase. The reason for this mismatch may be a larger volume of x-ray collection than the size of the secondary phase.

The data from EPMA analysis together with the possibility of substitution both La1 and La2 sites in the LWO composition discussed above (subsection 6.1), made it believe that Ce substitutes W_{La2} sites, thus forming W rich phase $La_6W_2O_{15}$. Even so $La_6W_2O_{15}$ compound was not confirmed by XRD analysis (subsection 5.1), appearance of the secondary phase peaks were similar to that reported by Magrasó et al. [17].

6.5 Future work

It would be interesting to investigate a donor doped LWO with lower than 2 mol% Ce and higher than 5 mol% Ce in order to confirm the trends of formation of $La_6W_2O_{15}$ phase upon donor substitution and the influence of it to the electrical measurements. Furthermore, in order to study the transport properties, the EMF transport number measurements could be maintained. The thermogravimetric measurements should be performed both before and after the electrical measurements to study the influence of the measurements on the stoichiometry.

From the impedance measurements performed in these studies, it seems interesting to investigate the dependency of grain boundary on water vapor pressure to study the hydration process in the grain boundaries of Ce-dopes LWO. For the thoroughly grain boundary studies is would interesting to do TEM to verify space charge layer theory and study how positive defects upon donor doping influence the grain boundary.

In order to study phase composition of doped LWO, EPMA analysis should be performed even more thoroughly. This means statistical collection of the data from spot analysis and longer time for the elemental mapping.

In case of the gas separation membranes it would be interesting to investigate a Ce-doped $NdW_{1/6}O_2$ and/or $GdW_{1/6}O_2$. These materials were reported as interesting for membrane application since protons charge compensate electrons under partial reduction at low temperature [9]. In respect to gas separation membranes, the ambipolar proton-electron conductivity may be estimated and compared with that of strontium cerate ceramics, which has been recently tested for hydrogen permeability [47].

7 Conclusion

2Ce-LWO and 5Ce-LWO were synthesized by a wet-chemical gelation method and characterized by X-Ray diffraction (XRD), scanning electron microscopy (SEM) and electron probe micro-analysis (EPMA). Formation of a secondary phase was revealed, which is possibly related to $La_6W_2O_{15}$.

Based on the total conductivity measurements in the temperature range from 1000 °C to 300 °C, it was concluded that Ce-doped LWO54 exhibits mixed ionic - electronic conduction where the ionic contribution is predominated by protons below ~ 800 °C. The total ionic conductivity of Ce-doped LWO54 is lower than that of undoped LWO54, and it decreases with increasing Ce content, indicating thus the decrease of the oxygen vacancies concentration due to an effect of Ce acting as a donor dopant. N – and p – type electronic conductivities predominate at high temperatures under reducing and oxidizing conditions, respectively. N-type electronic conductivity increases significantly with Ce content as expected from the higher donor doping concentration for 5% Ce-doped LWO54 compared to 2%Ce-doped LWO54.

Impedance spectroscopy analysis revealed that the grain boundaries are more resistive under oxidizing conditions, and increasingly resistive with higher Ce content. The total conductivity under reducing conditions was presented only by grain interior. It was suggested that this difference arose due to an inherent space charge layer effect.

By modeling the thermogravimetric measurements and the temperature dependencies of the total conductivity, the thermodynamic and transport parameters were estimated. Modeling of the data set resulted in an estimation the standard enthalpy and entropy of hydration for both compounds of -105 ± 5 kJ/mol and -123 ± 5 J/molK respectively. The slightly more negative hydration enthalpy than that of undoped LWO ($\sim -85\pm5$ kJ/mol) could be explained by a higher stability of Ce-doped LWO, which was supported by a smaller lattice parameter (a = 11.165 Å). The enthalpy of mobility of protons and oxide ions were estimated to be 60 ± 5 kJ/mol and 90 ± 10 kJ/mol, respectively, which is in agreement with literature [15].

Phase composition of donor doped LWO was obtained mainly by EPMA measurements. This analysis revealed that Ce substitutes both La and W cations with a precipitation of $La_6W_2O_{15}$ secondary phase. This secondary phase appeared in a

higher concentration with increasing donor content.

The protonic conductivity of 2Ce-LWO reached the maximum of 0.00102 S/cm at 900 °C, while it is one order of magnitude lower for 5Ce-LWO at the same temperature. The material conducts electrons (and oxide ions) at high temperatures so it can be used as a membrane for gas separation by ambipolar transport of H^+ and $e/$.

8 References

1. Giacomelli, G., *The energy problem.* Radiation Measurements, 2009. **44**(9–10): p. 707-716.

2. EIA. *International Energy Outlook 2013*. United States Department of Energy; Availabe from www.eia.gov.

3. *Our Finite World*. [cited 2013 May]; Available at www.ourfiniteworld.com.

4. Hansen, J., M. Sato, R. Ruedy, *Dangerous human-made interference with climate: a GISS modelE study.* Atmospheric Chemistry and Physics, 2007. **7**: p. 2287–2312.

5. Mekhilef, S., R. Saidur, and A. Safari, *Comparative study of different fuel cell technologies.* Renewable and Sustainable Energy Reviews, 2012. **16**(1): p. 981-989.

6. Magraso, A., et al., *Development of Proton Conducting SOFCs Based on LaNbO(4) Electrolyte - Status in Norway.* Fuel Cells, 2011. **11**(1): p. 17-25.

7. Patcharavorachot, Y., et al., *Analysis of planar solid oxide fuel cells based on proton-conducting electrolyte.* Solid State Ionics, 2010. **181**(35–36): p. 1568-1576.

8. Gallucci, F., et al., *Recent advances on membranes and membrane reactors for hydrogen production.* Chemical Engineering Science, 2013. **92**(0): p. 40-66.

9. Haugsrud, R., *Defects and transport properties in Ln_6WO_{12} (Ln=La, Nd, Gd, Er).* Solid State Ionics, 2007. **178**(7–10): p. 555-560.

10. Norby, T. and Y. Larring, *Mixed hydrogen ion–electronic conductors for hydrogen permeable membranes.* Solid State Ionics, 2000. **136–137**(0): p. 139-148.

11. Haugsrud, R. and C. Kjolseth, *Effects of protons and acceptor substitution on the electrical conductivity of La_6WO_{12}.* Journal of Physics and Chemistry of Solids, 2008. **69**(7): p. 1758-1765.

12. Shimura, T., S. Fujimoto, and H. Iwahara, *Proton conduction in non-perovskite-type oxides at elevated temperatures.* Solid State Ionics, 2001. **143**(1): p. 117-123.

13. Cecilia Solís, S.E., Reidar Haugsrud, José M. Serra, *$La_{5.5}WO_{12-\delta}$ Characterization of Transport Properties under Oxidizing Conditions: A Conductivity Relaxation Study.* The journal of physical chemistry, 2011. **115**(22).

14. *Database of Ionic Radii*. [cited 2013 May]; Available at http://abulafia.mt.ic.ac.uk/shannon/ptable.php.

15. Erdal, S., et al., *Defect structure and its nomenclature for mixed conducting lanthanum tungstates $La_{28-x}W_{4+x}O_{54+3x/2}$*. International Journal of Hydrogen Energy, (0).

16. Norby, P.K.a.T., *Defects and transport in crystalline solids. Compendium for the advanced level course Defect Chemistry and Reactions in Solids KJM5120.* September 2007.

17. Magraso, A., et al., *New crystal structure and characterization of lanthanum tungstate "La_6WO_{12}" prepared by freeze-drying synthesis.* Dalton Transactions, 2009(46).

18. Yoshimura, M. and J.F. Baumard, *Electrical conductivity of solid solutions in the system CeO_2-La_6WO_{12}*. Materials Research Bulletin, 1975. **10**(9): p. 983-988.

19. Norby, T., *A Kroger-Vink compatible notation for defects in inherently defective sublattices.* J. Korean Ceram. Soc., 2010. **47**(1): p. 19-25.

20. Magraso, A., et al., *Complete structural model for lanthanum tungstate: a chemically stable high temperature proton conductor by means of intrinsic defects.* Journal of Materials Chemistry, 2012. **22**(5): p. 1762-1764.

21. Haile, S.M., G. Staneff, and K.H. Ryu, *Non-stoichiometry, grain boundary transport and chemical stability of proton conducting perovskites.* Journal of Materials Science, 2001. **36**(5): p. 1149-1160.

22. Haile, S.M., D.L. West, and J. Campbell, *The role of microstructure and processing on the proton conducting properties of gadolinium-doped barium cerate.* Journal of materials research, 1998. **13**(06): p. 1576-1595.

23. Ehrenberg, H., et al., *Yttrium rhenium oxide, $Y_7ReO_{14-\delta}$: a cubic fluorite superstructure.* Solid State Sciences, 2004. **6**(3): p. 247-250.

24. M.E. Ivanova, J.S., J.M. Serra, *Influence of the La6W2O15 Phase on the Properties and Integrity of $La_{6-x}WO_{12-\delta}$ Based Membranes.* Chemistry and Materials research, 2012. **2**(1).

25. Chambrier, M.H., et al., *Ab-initio structure determination of β-La_2WO_6.* Journal of Solid State Chemistry, 2009. **182**(2): p. 209-214.

26. Chambrier, M.H., R.M. Ibberson, and F. Goutenoire, *Structure determination of α-$La_6W_2O_{15}$*. Journal of Solid State Chemistry, 2010. **183**(6): p. 1297-1302.

27. Hancke, R., et al., *Hydration of lanthanum tungstate (La/W=5.6 and 5.3) studied by TG and simultaneous TG–DSC.* Solid State Ionics, 2013. **231**(0): p. 25-29.

28. Kjølseth, C., et al., *Space–charge theory applied to the grain boundary impedance of proton conducting $BaZr_{0.9}Y_{0.1}O_{3-\delta}$.* Solid State Ionics, 2010. **181**(5–7): p. 268-275.

29. Göbel, M.C., G. Gregori, and J. Maier, *Electronically blocking grain boundaries in donor doped cerium dioxide.* Solid State Ionics, 2012. **215**(0): p. 45-51.

30. Park, H.J., et al., *Interfacial protonic conduction in ceramics.* Journal of the European Ceramic Society, 2009. **29**(12): p. 2429-2437.

31. NorECsAS., *Probostat.* [sited 2013 April]. Available from http://www.norecs.com.

32. Truls Norby, P.K., *Electrical Conductivity and Defect Structure of Y203 as a Function of Water Vapor Pressure.* **67**(12): p. 786-792.

33. T. Norby, *Gasmix: Software for calculating partial pressures of mixed gases, University of Oslo.*

34. *Microsoft Visio Professional.* Version 14.0, 2010.

35. AMATEK. *Advanced measurement technologies.* [cited 2013 March]; Availabe from http://www.solartronanalytical.com/.

36. Boukamp, B.A., *Equivalent Circuit for Windows version 1.2,*. Twente University of Technology: Netherlands.

37. Norby, T., *Electrical Measurements - Compedium for the advanced level course Experimental methods KJM-MENA4010.* . 2011, University of Oslo.

38. Furøy, K.A., et al., *Role of protons in the electrical conductivity of acceptor-doped $BaPrO_3$, $BaTbO_3$, and $BaThO_3$.* Solid State Ionics, 2007. **178**(7–10): p. 461-467.

39. BrukerAXR, *D8 Advanced.* [cited 2013 March]; Available from www.bruker.com.

40. Kofstad, P., *Nonstoichiometry, Diffusion, and Electrical Conductivity in Binary Metal Oxides.* Wiley-Interscience, 1972.

41. Avila-Paredes, H.J., et al., *Dopant-concentration dependence of grain-boundary conductivity in ceria: A space-charge analysis.* Journal of Materials Chemistry, 2009. **19**(27): p. 4837-4842.

42. Brown, R., *TableCurve 2D for Windows version 5.01.* Systat Software Inc.: USA.

43. Magrasó, A., et al., *Defects and transport in Gd-doped BaPrO3.* Journal of Electroceramics, 2009. **23**(1): p. 80-88.

44. *Origin 8.6.0, Data Analysis and Graphing Software.* OriginLab Corporation, USA.

45. Larring, Y. and T. Norby, *The equilibrium between water vapour, protons, and oxygen vacancies in rare earth oxides.* Solid State Ionics, 1997. **97**(1–4): p. 523-528.

46. T. Norby, R.H., *Dense Ceramic Membranes for Hydrogen Separation, in Nonporous Inorganic Membranes.* Wiley-VCH Verlag GmbH & Co. KGaA, 2006: p. 1-48.

47. Dahl, P.I., et al., *Synthesis, densification and electrical properties of strontium cerate ceramics.* Journal of the European Ceramic Society, 2007. **27**(16): p. 4461-4471.

9 Appendix

This appendix includes the derivation of the defect chemistry equations used in the curve fittings of the TG measurements and the temperature ramps. For both samples, the simplified electroneutrality condition is assumed:

$$\frac{108}{56}\left[V_{\frac{54}{56}O}^{\frac{108}{56}\bullet}\right]+\frac{52}{56}\left[OH_{\frac{54}{56}O}^{\frac{52}{56}\bullet}\right]=\left[Acc^{/}\right] \tag{A1}$$

The equilibrium coefficient of hydration expresses as a combination of Equation 2.38 and Equation 2.21:

$$K_{hydr}=\exp\left(\frac{\Delta S_{hyrd}^{O}}{R}\right)\exp\left(-\frac{\Delta H_{hyrd}^{O}}{RT}\right)=\frac{\left[OH_{\frac{54}{56}O}^{\frac{52}{56}\bullet}\right]^{2}}{\left[V_{\frac{54}{56}O}^{\frac{108}{56}\bullet}\right]\left[O_{\frac{54}{56}O}^{\frac{4}{56}/}\right]p_{H_2O}} \tag{A2}$$

Using A1 and A2, the proton concentration can be evaluated to give the following expression:

$$\left[OH_{\frac{54}{56}O}^{\frac{52}{56}\bullet}\right]=\frac{13}{54}K_{hydr}\left[O_{\frac{54}{56}O}^{\frac{4}{56}/}\right]p_{H_2O}\left(-1+\sqrt{\frac{1512}{169}\frac{[Acc^{/}]}{K_{hydr}\left[O_{\frac{54}{56}O}^{\frac{4}{56}/}\right]p_{H_2O}}}\right) \tag{A3}$$

The concentration of oxygen vacancies can be expressed with a combination of Equation A1 and Equation A3:

$$\left[V_{\frac{54}{56}O}^{\frac{108}{56}\bullet}\right]=\frac{56\left[Acc^{/}\right]-52\left[OH_{\frac{54}{56}O}^{\frac{52}{56}\bullet}\right]}{108} \tag{A4}$$

The concentration of electrons expressed from Equation 2.13.

$$n = K_{red}^{1/2} \left[V_{\frac{54}{56}O}^{\frac{108}{56}\bullet} \right]^{-1/2} p_{O_2}^{-1/4} \tag{A5}$$

The concentration of electron holes expressed from Equation 2.15

$$p = K_{ox}^{1/2} \left[V_{\frac{54}{56}O}^{\frac{108}{56}\bullet} \right]^{1/2} p_{O_2}^{1/4} \tag{A6}$$

The partial conductivity of a charge carrier i was expressed by Equation 2.49. However, the concentration of charge carrier is often given in molar fraction, and the specific conductivity is then given:

$$\sigma_i = z_i F p_m c_i \mu_i \tag{A7}$$

where F is the Faradays constant and p_m is the molar density of the sample. The partial conductivity of a charge carrier i can be extended from Equation 2.51:

$$\sigma = \frac{\sigma_0}{T} \exp\left(-\frac{E_a}{RT}\right) = z_i F p_m c_i \mu_{0,i} \frac{1}{T} \exp\left(-\frac{\Delta H_{mob,i}}{RT}\right) \tag{A8}$$

where σ_0 is the pre-exponential constant, R is the gas constant, $\mu_{0,i}$ is the mobility and $\Delta H_{mob,i}$ is the enthalpy of migration of the charge carrier i.